

**A Tribological Study of the Interaction between
Surface Micro Texturing and Viscoelastic Lubricants**

by

Sara J. Hupp

B.S., Mechanical Engineering
Virginia Polytechnic Institute and State University, 2002

Submitted to the Department of Mechanical Engineering
In Partial Fulfillment of the Requirements for the Degree of

Master of Science in Mechanical Engineering

at the
Massachusetts Institute of Technology
September 2004

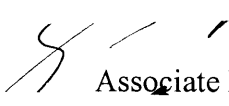
© 2004 Massachusetts Institute of Technology
All rights reserved

Signature of Author



.....
Department of Mechanical Engineering
August 8, 2004

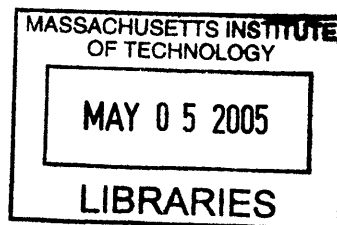
Certified by.....



.....
Professor Douglas P. Hart
Associate Professor of Mechanical Engineering
Thesis Supervisor

Accepted by.....

.....
Professor Lallit Anand
Chairman, Department Committee on Graduate Students
Department of Mechanical Engineering



BARKER

A Tribological Study of the Interaction between Surface Micro Texturing and Viscoelastic Lubricants

by

SARA JEAN HUPP

Submitted to the Department of Mechanical Engineering
on August 8, 2004, in partial fulfillment of the
requirements for the degree of
Master of Science in Mechanical Engineering

ABSTRACT

An experimental study is performed on micro textured surfaces using both elastic and Newtonian fluids in order to understand the effect of surface texturing and fluid rheology on sliding friction under lubricated conditions. Nickel micro textured surfaces containing 50 to 125 micron diameter pores and 1 to 20 percent area densities of pores are fabricated using novel techniques inspired by MEMS fabrication methods in order to obtain a metal surface that is corrosion and wear resistant. These surfaces are then friction tested using a torsional rheometer with a parallel plate configuration, and the resulting data is normalized to obtain a Stribeck diagram that spans the lubrication regimes from boundary lubrication to hydrodynamic lubrication. Each lubricant/surface pair results in a unique curve that is subsequently compared to other lubricant/surface pairs in order to study the effect of different surface texturing parameters as well as the effect of the particular lubricant rheology.

Experimental results from studying the effect of different surface texturing parameters indicate that particular micro textured patterns can reduce friction by as much as seventy-five percent after a controlled break-in period. Data from the tribo-rheometer also indicates that along with a reduction in friction, micro texturing can result in shifting the entire Stribeck curve so that the transition points between lubrication regimes are delayed or induced by as much as an order of magnitude of the Gumbel number, depending on the lubricant and running conditions. Focusing next on the effect of lubricant rheology on sliding friction over micro textured surfaces, this research reveals that the Stribeck curve will experience a shift according to the lubricant elasticity. A new dimensionless number formed by dividing the Gumbel number by the elasticity factor of the fluid can accurately account for the Stribeck curve shift as a result of fluid elasticity.

Acknowledgements

I would first like to thank Professor Douglas Hart, “Doug”, for providing the impetus for this project and allowing me the freedom to shape it in a way that was exciting and meaningful. Somehow I never thought that I would learn to love friction, but your constant excitement and vision for my work helped me realize a great project and carry my momentum through to the next step.

I would like to thank Kurt Broderick for his endless patience in the microfab and Bruce Wu for trying so hard to help me with my fruitless attempts at electroplating. I would also like to thank the Jack Kent Cooke Foundation for their amazing financial support of my graduate education.

I would like to thank my colleagues at HML for putting up with my constant badgering on the details of rheology and the beloved rheometer. Specifically, Ryan, Karen, Freddy, Sean, Sarah, and Lily, thanks for making our little section of the lab a happy place and at least pretending that you liked my pottery! To all of my wonderful friends – I can’t believe that I found such an amazing home at MIT! I would especially like to thank my roomies, Sanaz, Janine, and Tiffany, for being behind me and cheering me on every step of the way. Each one of you was truly inspirational in your own special way... yes, Tiffany, you had an apartment job, too. Furthermore, to the person who probably taught me the most about the big city, thank you Lucas for always knowing what to say. At the end of my master’s experience, there were two people left to push me past the finish line. Ryan and Jean, I would not have made it through the very final steps without your friendship and encouragement, thank you!

To my mom, thanks for being so strong and reminding me that my strength lies within myself, and thank you for letting me know that no matter where I go, I always have a warm, loving place back home. Of course, I can’t forget to say thanks to my wonderful siblings who keep me on my toes and make sure that I don’t get out of line, and above all, I thank God, whose light has always guided me when no one else could.

Finally, I would like to dedicate this thesis to my father. He was the one who taught me how to fix my car and make my ideas come to life in our wood shop. Somehow I was instilled with the concepts of mechanical advantage and material compatibility before I even knew how to ride a bike. More than that, though, he never let me settle for anything less than my best. He inspired me to always challenge myself and to persevere to the end, and so I dedicate this thesis to my dad.

Table of Contents

1	INTRODUCTION.....	10
1.1	Importance of Tribology Research	10
1.2	Physical Insights into Lubrication Theory	12
1.2.1	Basic lubrication regimes.....	12
1.2.2	The Stribeck diagram.....	16
1.3	Previous Experimental Investigation	19
1.4	Previous Theories on Micro-Texturing.....	21
1.5	Research Presented for this Master’s Thesis	23
2	EXPERIMENTAL SETUP	25
2.1	Tribometer.....	25
2.2	Rheometer Setup.....	27
2.3	Textured Nickel Surfaces.....	29
2.4	Lubricant.....	32
3	MANUFACTURE OF TEXTURED SURFACES.....	34
3.1	Vapor Deposition	37
3.2	Photolithography.....	38
3.2.1	OmniCoat™ Release Layer Application	39
3.2.2	SU-8 Photoresist Application	40
3.2.3	OmniCoat™ Develop	42
3.3	Electroless Nickel Plating.....	43
3.3.1	Electroless Nickel Plating Chemistry	44
3.3.2	Bath Preparation.....	46
3.3.3	Nickel Plating.....	46
3.4	OmniCoat™ Removal	48
4	LUBRICANT RHEOLOGY	50
4.1	STP Oil Additive Rheology	51
4.2	PDMS Rheology	58
5	EXPERIMENTAL PROCEDURES	60
5.1	Flow Parameters.....	60

5.2	Run-In Procedure	61
5.3	Testing Procedure	62
5.3.1	Configuration for STP Oil Additive	63
5.3.2	Configuration for PDMS Lubricant.....	64
5.4	Data Processing.....	64
6	RESULTS	65
6.1	Procedure Verification	65
6.1.1	Stribeck Diagram	65
6.1.2	Run-In Procedure	69
6.1.3	Increasing/Decreasing Velocity Curve Shifts	70
6.2	Results of Surface Texturing Effects	71
6.2.1	Surface Data.....	72
6.2.2	Summary of STP Oil Testing.....	90
6.3	Results of Lubrication Elasticity.....	91
6.4	Summary of Major Results	95
7	DISCUSSION.....	98
7.1	Analysis of Experimental Error and Limitations	98
7.2	Run-In Procedure	101
7.3	Interpreting Stribeck Curve Shifts due to Direction of Velocity Gradient .	102
7.4	Effect of Texture Pattern on Friction Coefficient	104
7.5	Effect of Viscoelastic Lubricant Properties on Surface Friction	106
8	CONCLUSIONS AND RECOMMENDATIONS.....	111
8.1	Conclusions.....	111
8.1.1	Testing Surfaces Using the Tribo-Rheometer.....	111
8.1.2	Friction Reduction using Surface Texturing Techniques	112
8.1.3	Impact of Lubricant Elasticity on the Stribeck Diagram	114
8.2	Recommendations for Future Work.....	115
	References.....	116
	Appendix A: Derivation of the Reynolds Equation	118
	Appendix B: Micro Textured Surface Photographs.....	122
	Appendix C: Second Order Fluid Solution for Weakly Elastic Fluids.....	131

List of Figures

Figure 1.1. Sliding friction lubrication regimes.....	15
Figure 1.2. Stribeck diagram.....	16
Figure 1.3. Illustration of surface contact in lubrication regimes	23
Figure 2.1. Tribo-rheometer schematic.....	26
Figure 2.2. Control components of the AR2000.....	28
Figure 3.1. Nickel micro textured surfaces.....	36
Figure 3.2. Failed electroplating	44
Figure 3.3. 100 μ m10% surface showing a non-uniform pattern	47
Figure 3.4. B100 μ m10% surface showing a uniform pattern	47
Figure 3.5. Photograph of a surface before the nickel plating process.....	49
Figure 3.6. Photograph of 50 μ m 2.5% micro textured surface.....	49
Figure 4.1. STP fluid viscosity	52
Figure 4.2. CABER test on STP fluid.....	53
Figure 4.3. Second order fluid model of STP fluid.....	55
Figure 4.4. STP oscillation test.....	56
Figure 4.5. STP relaxation time	57
Figure 4.6. PDMS viscosity	58
Figure 4.7. PDMS oscillation test.....	59
Figure 6.1. Raw data from friction testing at 15N.....	66
Figure 6.2. Raw data from friction testing at 10N.....	67
Figure 6.3. Normalized surface data.....	67
Figure 6.4. Consistency test.....	68
Figure 6.5. Effect of run in period.	70
Figure 6.6. Hysteresis effet	71
Figure 6.7 Bcontrol under 40X magnification.....	73
Figure 6.8. Control surface Stribeck diagram with STP fluid	74
Figure 6.9. 50um 1% surface photograph.....	75

Figure 6.10. B50um 1% surface photograph	75
Figure 6.11. 50 μ m 1% Stribeck diagram with STP oil.....	76
Figure 6.12. 50 μ m 2.5% surface photograph.....	77
Figure 6.13. B50 μ m 2.5% surface photograph	77
Figure 6.14. 50 μ m 2.5% Stribeck diagram with STP oil.....	78
Figure 6.15. 50 μ m 5% surface photograph.....	79
Figure 6.16. B50 μ m 5% surface photograph.....	79
Figure 6.17. 50 μ m 5% Stribeck diagram with STP oil.....	80
Figure 6.18. 74 μ m 5% surface photograph.....	81
Figure 6.19. 74 μ m 5% Stribeck diagram with STP oil.....	82
Figure 6.20. 100 μ m5% surface photograph.....	83
Figure 6.21. B100 μ m5% surface photograph.....	83
Figure 6.22. 100 μ m 5% Stribeck diagram with STP oil.....	84
Figure 6.23. 100um10% surface photograph.....	85
Figure 6.24. B100 μ m10% surface photograph	85
Figure 6.25. 100 μ m 10% Stribeck diagram with STP oil.....	86
Figure 6.26. 100 μ m15% surface photograph.....	87
Figure 6.27. B100um15% surface photograph.....	87
Figure 6.28. 125 μ m 15% Stribeck diagram with STP oil.....	88
Figure 6.29. 125 μ m 20% Stribeck diagram with STP oil.....	89
Figure 6.30. Summary of micro patterns with STP oil.....	90
Figure 6.31. Comparison of STP and PDMS30k on the control surface.....	92
Figure 6.32. Comparison of STP and PDMS on 50 μ m1% surface.	92
Figure 6.33. Stribeck diagram of STP and PDMS on 50 μ m2.5% surface.....	93
Figure 6.34. Stribeck diagram of STP and PDMS on 50 μ m5% surface.....	93
Figure 6.35. Stribeck diagram of STP and PDMS on 100 μ m5% surface.....	94
Figure 6.36. Stribeck diagram of STP and PDMS on 100 μ m10% surfaces.....	94
Figure 6.37. Summary of textured surfaces using STP oil	96
Figure 6.38. Summary of textured surfaces using PDMS (30Pa.s)	97

Figure 7.1. Wear study.....	100
Figure 7.2. Run-in study	103
Figure 7.3. Summary of the Stribeck curves for patterned surfaces.	104
Figure 7.4. Gumbel number shift as a result of the STP fluid elasticity.	107
Figure 7.5. Comparison of G_u and $G_{u,el}$	110
Figure 8.1. Apparent shift [Wakuda 2003]	113

List of Tables

Table 2.1. Typical deposit properties of CR-MRN electroless nickel.....	31
Table 3.1. Details for applying the OmniCoat™ release layer.....	39
Table 3.2. Photolithography process for SU-8 100 on borosilicate glass substrate.....	42
Table 4.1. Selected lubricant properties.....	50

CHAPTER 1

1 INTRODUCTION

1.1 Importance of Tribology Research

Tribology is the study of the interaction between surfaces in relative motion. When two surfaces slide past one another, the resulting sliding can create severe conditions that result in strong opposing forces and heavy surface wear. Frictional forces pose a significant barrier to many engineering, biological, and geological systems; earthquakes and arthritis pain are two familiar examples of natural phenomena that are a direct result of friction. In engineering systems, friction can not only cause systems to wear and require routine maintenance, but it can also lead to system failure. More importantly, though, large amounts of energy are wasted overcoming the frictional forces in systems involving rotating or moving components. An outstanding example of wasted energy occurs in an automobile, where 40% of the total engine energy is consumed by engine friction [1]. It is imperative that sliding friction is understood and methods for minimizing it are studied so that both lives and energy conservation can be improved.

Despite the apparent need for tribology research, engineers have been aware of frictional forces since the times of Leonardo daVinci and Newton. Using only simple experiments, daVinci was able to demonstrate Amonton's law, which states that dry,

sliding friction is proportional to and depends only on normal force. In his work, he also successfully noted that there were different mechanisms controlling rolling friction and sliding friction. Friction was identified by Isaac Newton as a force resisting motion, but he could not explain the basic physics behind friction to determine why it occurred. Since daVinci and Newton, many scientists have devoted their careers to understanding friction, but it is still “a force for which there is no general explanation” [2]. Current knowledge of lubricant and surface chemistry allows scientists to estimate interactions between surfaces under ideal situations with well-known materials, but most conditions require extensive experimental testing. Even advanced computational simulations have been limited to estimating friction coefficients or idealizing surfaces in order to predict an outcome which is still requires experimental testing for verification. As a result, engineers have been unable to optimize surface/lubricant interactions and are forced to design systems that require extensive preventative maintenance where parts must be replaced and lubricant must be changed.

The goal of the research presented in this thesis, is to use experimentally produced Stribeck diagrams to gain a better understanding of the surface/lubricant interaction between surfaces so that more accurate predictions and models can be designed for sliding friction. More specifically, micro patterned surfaces will be friction tested with viscous and viscoelastic lubricants under sliding conditions to determine which surface parameters can minimize friction when combined with a particular lubricant rheology. Previous research has focused on testing micro patterned surfaces in particular lubrication regimes rather than looking at texturing effects over the entire lubrication spectrum. They also concentrated on surface parameters while neglecting to exploit the elastic properties

of viscoelastic lubricants. This thesis explores the effects of surface micro texturing and lubricant rheology on the entire lubrication spectrum and introduces a new non-dimensional parameter that allows a lubricant to be “tuned” for specific sliding conditions in order to minimize friction.

1.2 Physical Insights into Lubrication Theory

1.2.1 Basic lubrication regimes

Before exploring the new concepts introduced in this paper, it is important to first understand the terminology and basic underlying principals. For this research, the lubrication and frictional properties between lubricated, sliding surfaces were studied. Under these conditions, there are three basic lubrication regimes: hydrodynamic lubrication, elastohydrodynamic lubrication, and boundary lubrication. These regimes are defined based on the surface/lubricant interaction and the resulting friction coefficient. Many tribologists refer to another regime called the mixed lubrication regime. Mixed lubrication is a state that has characteristics of both boundary and hydrodynamic lubrication.

Hydrodynamic lubrication is the term given to the regime where the sliding surface experiences hydrodynamic lift and is fully supported by a continuous, load-bearing film of lubricant. There is no interaction between the two surfaces, and therefore very little wear occurs. Under elastohydrodynamic lubrication conditions, there is also a continuous film of lubricant between the two surfaces, but the surfaces are loaded such

that a force is transmitted through the fluid and the surfaces deform elastically under the load. Elastohydrodynamic lubrication typically occurs at either slower speeds or at higher loads than the conditions for hydrodynamic lubrication.

To describe full-film lubrication, the equations of motion and the continuity equation are combined to form the Reynolds equation, which governs the pressure distribution in a lubricant film [3]. Assumptions of incompressibility and constant viscosity as well as the thin film lubrication approximation are made in order to simplify the equations. The complete derivation of the Reynolds equation is given in Appendix A, and the result is given by the equation:

$$\frac{\partial}{\partial x} \left(\frac{h^3}{\mu} \frac{\partial p}{\partial x} \right) + \frac{\partial}{\partial z} \left(\frac{h^3}{\mu} \frac{\partial p}{\partial z} \right) = 6(U_1 - U_2) \frac{\partial h}{\partial x} + 6h \frac{\partial(U_1 + U_2)}{\partial x} + 12(V_2 - V_1).$$

Unfortunately, the Reynolds equation is incomplete since it only considers the fluid parameters and ignores the surface characteristics. When the surfaces are deformable, the equations of surface material elasticity and the pressure dependence of lubricant viscosity must also be considered in the analysis. In the mixed and boundary lubrication regimes, surface roughness and surface chemistry may also play a significant role in the development of friction. Patir and Cheng showed that the effect of excessive surface roughness on friction can be taken into account by numerically solving the Reynolds equation for micro bearings to obtain the Patir-Cheng flow factors [4].

Boundary lubrication results when the full film of lubricant between the two sliding surfaces breaks down and the surfaces come into contact. The load on the sliding surface is no longer supported by fluid and is transferred to the surface contact area,

which is only a fraction of the apparent area because at the microscopic level, surfaces are composed of asperities that create hundreds of micro-scale peaks and valleys. Boundary lubrication is often characterized by very high friction and wear due to the intimate contact between the two surfaces. Surface asperities break and reform constantly while releasing bursts of energy that often result in flash temperatures [5] along with local changes in surface contact. The exact interaction between the surfaces is not yet fully understood. Since lubricant bulk properties are assumed to be inconsequential in this regime, much research has been performed to understand and develop boundary lubricants. These specialized lubricants interact with the chemistry of the surface to create a protective barrier layer of lubricant molecules between the two surfaces. Currently, most boundary lubricants simply act as a sacrificial layer and only delay the onset of friction and wear.

Finally, mixed lubrication is a combination of both boundary and full film lubrication. Since surfaces are not perfectly smooth and are often characterized by mountains and valleys of micro asperities, lubricant becomes trapped in some of the lower regions on the surface and is capable of helping to sustain some of the load between the two surfaces. Since all surfaces are unique, it is difficult to determine what percent of the load between surfaces is carried by the lubricant and what percent is sustained by the surfaces. Mixed lubrication is not well understood, and it is unclear what role the lubricant plays in decreasing the friction to a value below that of boundary lubrication.

The three main lubrication regimes, boundary, hydrodynamic, and elastohydrodynamic lubrications are illustrated in Figure 1.1.

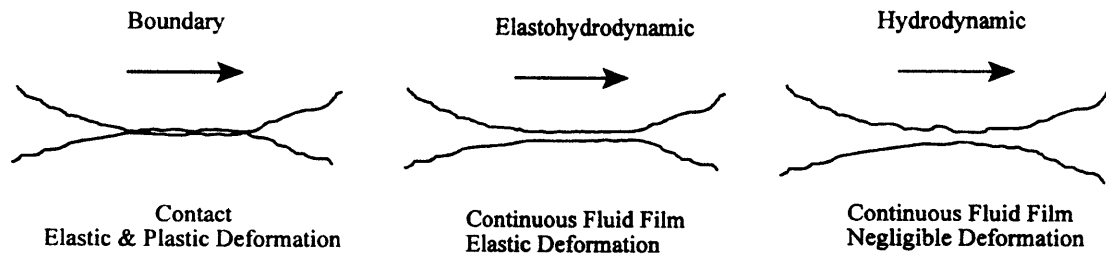


Figure 1.1. Illustration of the 3 main lubrication regimes in sliding friction [3]. Under both hydrodynamic and elastohydrodynamic lubrication, the sliding surface experiences hydrodynamic lift and is fully supported by a continuous, load-bearing film of lubricant. Hydrodynamic lubrication involves no interaction between the two surfaces, while elastohydrodynamic lubrication allows a force to be transmitted through the fluid and elastically deform the surfaces. Boundary lubrication results when the full film of lubricant between the two sliding surfaces breaks down and the surfaces come into contact. Tribologists also often refer to a mixed lubrication regime, which is a state that combines the properties of full-film and boundary lubrication. The fluid supports a fraction of the load, while the contacting surfaces support the remainder of the load.

1.2.2 The Stribeck diagram

The Stribeck diagram, or Reynolds-Sommerfeld curve as it is otherwise known [6], is often used to characterize sliding surface friction [7]. The lubrication regimes for sliding friction can visually be characterized by their location on a Stribeck diagram, as shown in Figure 1.1.

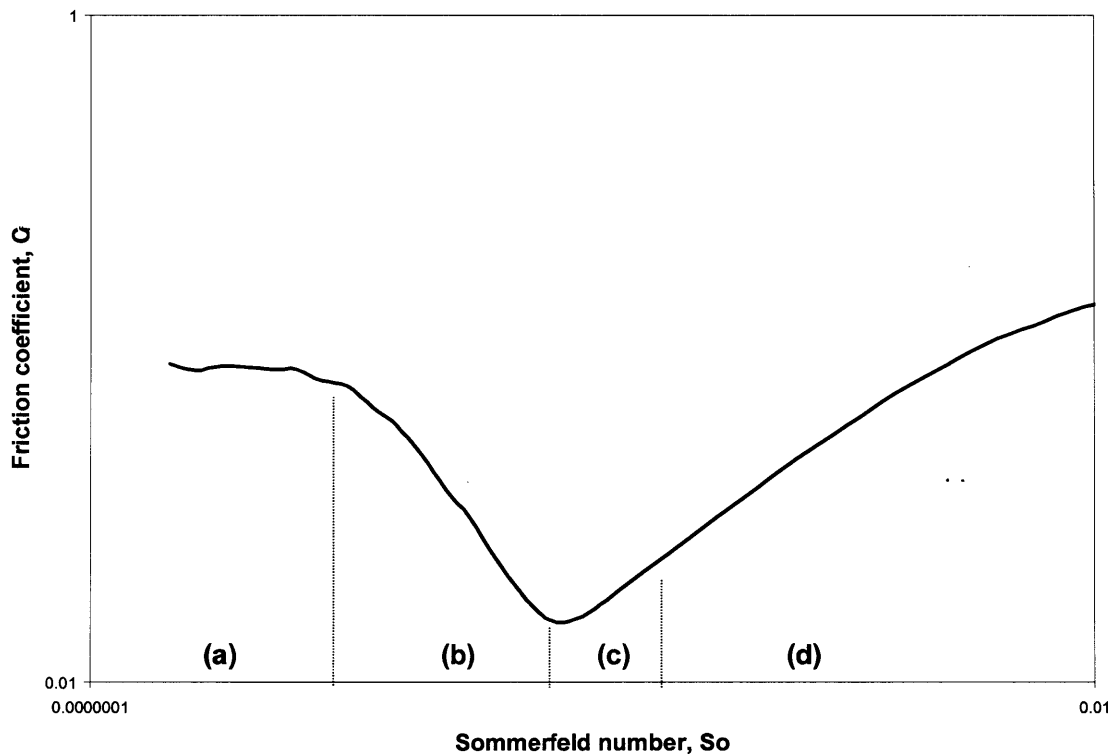


Figure 1.2. A typical Stribeck diagram illustrating the 4 main regimes of sliding lubrication. These regimes are (a) boundary lubrication, (b) mixed lubrication, (c) elastohydrodynamic lubrication, and (d) hydrodynamic lubrication. Boundary lubrication (a) is found at lower Sommerfeld numbers where either the normal load is very high or the sliding velocity is very slow. Mixed lubrication (b) is found at moderate Sommerfeld numbers, and the characteristic dip in the Stribeck curve, is indicative of the transition from mixed to elastohydrodynamic lubrication (c). High Sommerfeld numbers indicate either very light normal loads or high sliding velocities, which lead to hydrodynamic lubrication (d).

Although the Stribeck diagram is an essential tool for design and studies in tribology, it can only be created experimentally and is unique for a particular surface/lubricant pair. Experimentally, a Stribeck curve can be obtained by performing an angular velocity sweep on a triborheometer with a constant normal load and variable gap height. The shearing stress (Pa), τ , required to rotate one surface across the other stationary surface is measured and normalized with the normal stress (Pa), σ , or load, to get a friction coefficient, C_f .

$$C_f = \frac{\tau}{\sigma}$$

The resulting friction coefficient is plotted as a function of the Sommerfeld number, So , which is the viscosity (Pa.s), μ , times the speed (m/s), U , divided by the normal stress per unit length (Pa/m), P , assuming a constant bulk viscosity.

$$So = \frac{\mu U}{P}$$

When looking at a Stribeck diagram, boundary lubrication is found at lower Sommerfeld numbers where either the normal load is very high or the sliding velocity is very slow. Mixed lubrication is found at moderate Sommerfeld numbers, and the characteristic dip in the Stribeck curve, such as the one shown in Figure 1, is indicative of the transition from mixed to either elastohydrodynamic lubrication or hydrodynamic lubrication depending on the surface material properties. High Sommerfeld numbers indicate either very light normal loads or high sliding velocities, which lead to hydrodynamic lubrication and the establishment of a full film of lubricant between the sliding surfaces.

In rotational systems, often the Gumbel number, Gu , replaces the Sommerfeld number. The Gumbel number uses angular velocity (rad/s), ω , instead of the sliding velocity and normal stress (Pa), σ , instead of the normal stress per unit length.

$$Gu = \frac{\mu\omega}{\sigma}$$

One advantage of the Stribeck curve in tribology research is that the non-dimensional Gumbel or Sommerfeld numbers allow a single curve to represent the same lubricant-surface pair under varying sliding speeds and normal forces. To fully characterize the sliding frictional properties between two surfaces in lubricated contact, a complete Stribeck curve spanning all three lubrication regimes, such as that in Figure 1.2, is needed. Unfortunately, until now the Stribeck diagram has typically been a composite of several tests performed under separate lubrication conditions. For example, a full film test will be performed using a particular lubricant/surface pair, and then that same pair will be used in a minimally lubricated test. Although the separate tests may use the same materials and lubricants, the testing conditions can change dramatically, thus the two ends of the lubrication spectrum will not necessarily combine to create a reliable Stribeck curve. Section 1.3 describes some of the previous theories and methods of friction testing sliding surfaces.

1.3 Previous Experimental Investigation

Although we still do not know exactly what causes friction or how to predict a friction coefficient, many tribological parameters have been investigated in an attempt to reduce sliding friction. In particular, one of the dominant variables in sliding friction for both engineering and natural surfaces is surface roughness. In 1959, Lewis and McCutchen published an article in *Nature* about the role that surface structure of cartilage played in lubricating animal joints [8]. This article highlighted the fact that cartilage is a sponge-like material with a micro-scale texture that can capture fluid in tiny pores. When cartilage is compressed, the fluid is squeezed from the pores and can form a layer of fluid between the cartilage and contacting surface. When the load is released, the fluid is re-absorbed into the cartilage matrix. In 1965, industrial studies showed that small pores on metallic surfaces were also useful as lubricant reservoirs to reduce friction [9]. By glass bead peening a steel surface, Bossler showed that it is possible to significantly reduce sliding friction in the boundary lubrication regime. The exact amount of reduced friction depends strongly on the final RMS surface roughness attained with the glass beads. From this initial research, others began experimentally exploring the effects of micro texturing.

When researchers began to design controlled surface textures, most research was focused toward the hydrodynamic lubrication regime. Specifically, research was performed on rotary-shaft face seals, which ideally only run under full-film lubrication conditions with the exception of experiencing boundary lubrication conditions during the

startup period. Initially, testing was limited to detecting the point of full-film lubrication break down, and the surfaces were etched in copper, a very soft metal [10, 11]. Extensive testing confirmed the fact that micro texturing reduced the friction of sliding surfaces in the hydrodynamic regime and sparked more interest in future studies. Hypotheses were presented that suggested this reduction in friction was either a result of a pressure imbalance due to cavitation around the surface features [11] or possibly the leading edge of each asperity became slightly worn so that it acted as an inclined surface that promoted lift [10]. The leading edge hypothesis was supported by experimental data that indicated the initial friction at start up was much higher than the average values. If a seal was permitted to run at a high load for a specified period of time, called a run-in period, then the seal would experience much less friction when it was installed later under standard running conditions. Given the experimental evidence, it was assumed that this “run-in” period would be required to wear the leading edge of each asperity.

Later, the experimentally observed “run-in” effect was tested by Cogdell using a ball-on-flat device that measured the resulting torque when three steel balls were slid against a steel textured surface [12]. The surface texturing was created simply by scuffing a surface using abrasive paper with different grit sizes. Collected contact resistance measurements indicated that there was an intense initial period of contact resistance, which implied the existence of a run-in period. Instead of measuring friction, the wear rate was determined for the different textures by visually inspecting the steel balls at 1-hour intervals. After the initial wear period, wear measurements indicated that surface wear could be successfully decreased by applying a surface texture.

Eventually, different types of surface texturing were explored. Experiments performed for the sheet metal forming industry indicated that a combination of both surface dimples and channels created a desirable surface that could contain liquid to allow for hydrostatic liquid pockets as well as transport lubricant to areas on the surface that were facing starved lubrication conditions [13]. Suh concluded that undulations in machined titanium surfaces reduced friction by collecting the wear particles created during boundary lubricated contact [14]. Recently, laser ablation techniques have been used to pattern ceramic and sapphire surfaces as well as carbon face seals [15-19]. Each paper presents research showing that surface micro texturing improves the tribological conditions between sliding surfaces, but they are unable to give evidence of the effects of micro texturing in multiple lubrication regimes.

1.4 Previous Theories on Micro Texturing

Although micro texturing can be experimentally shown to improve surface lubrication, the theoretical evidence is sparse. In the hydrodynamic regime, classical lubrication theory does not predict the existence of a stable hydrodynamic film for steady-state, isothermal, incompressible flow between smooth, parallel surfaces [10]. There must be an inclined surface to attain the appropriate pressure gradient to allow the fluid to sustain a load. Anno et al. hypothesize that the lift is possible with micro textured surfaces because the leading edge of each hole becomes worn down to create a slightly inclined surface. Using a rotary shaft face seal against a glass panel, Hamilton

observed cavitation bubbles on the surface, which indicated that the pressure within a cavity can reach the vapor pressure of the lubricant [11]. Once the vapor pressure is reached, cavitation occurs and the cavity pressure remains constant while the surrounding surface experiences a much higher pressure. The pressure difference results in the ability of the textured surface to maintain a load, while a smooth surface cannot maintain a load because it does not experience any pressure gradients.

In the boundary lubrication regime, only hypotheses are available to explain the phenomena that adding a surface texture will reduce the friction between sliding, lubricated surfaces. While it seems reasonable that applied texture acts as a micro-reservoir to hold the lubricant, Yu postulates that hydrodynamic pressure over the pore and surrounding areas can lift the contacting surfaces and reduce the contact force between a face seal on a silicon carbide ring [19]. When the two surfaces are not both planar, Wakuda shows that for a cylinder-on-flat geometry, the area of contact can actually straddle the applied texture. This condition would allow a flow of lubricant underneath a section of the contacting surface, which could create a lifting force to reduce the normal force on the surface [18]. Figure 1.3 illustrates this condition by showing the area of pin contact compared to different diameter holes for a cylinder-on-flat geometry.

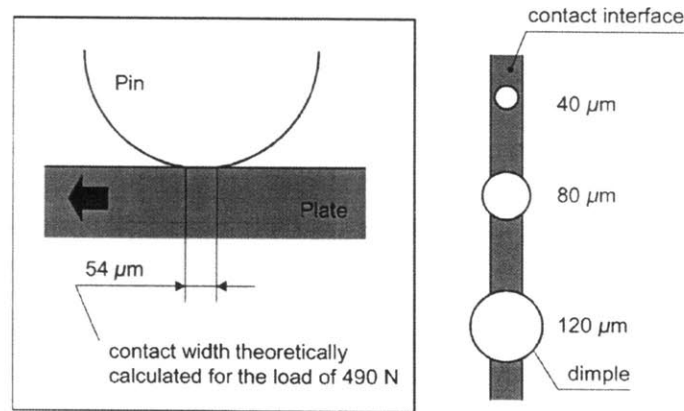


Figure 1.3. Illustration showing the relationship between the contact width of the mating surfaces and dimple size [18]. Wakuda shows that for a cylinder-on-flat geometry, the area of contact can actually straddle the applied texture. This condition would allow a flow of lubricant underneath a section of the contacting surface, which could create a lifting force to reduce the normal force on the surface

1.5 Research Presented for this Master's Thesis

The research presented for this thesis explores the effect of surface micro texturing and lubricant rheology on the friction coefficient between sliding surfaces in order to understand the fundamental mechanisms that control friction and to determine how micro texturing can be used to reduce it. In contrast to previous research, the experimental data presented in this paper can be used to produce the entire Stribeck diagram, which allows the effect of micro texturing and lubricant rheology to be determined for all lubrication regimes rather than just focusing on a specific region of the lubrication spectrum.

In order to perform this research, an array of micro-scale holes is created on a nickel surface using a novel procedure that involves vapor deposition, photo lithography, and finally electroless nickel plating. Nine different texture patterns are created that have different hole shapes, sizes, and density of holes. These patterns are then tested using a

unique method that allows tight control over testing parameters and is capable of a large operating range. Using this testing method, a single test can characterize the textured surface in all lubrication regimes. Along with testing different texture parameters, four different lubricating fluids are tested on different surfaces to determine the effect of lubricant viscosity and elasticity on the resulting Stribeck curves.

After friction testing each surface with different lubricants, the results are normalized using the coefficient of friction and the Gumbel number, which are the two parameters that make up a Stribeck diagram for rotating systems. The results are further analyzed using dimensional analyses, surface mechanics, and fluid mechanics, and lead to a new scaling parameter that characterizes the effect of lubricant elasticity on the Stribeck diagram. Using this new scaling parameter, surfaces under particular running conditions can be tuned by choosing a desirable lubricant rheology in order to minimize the sliding friction.

CHAPTER 2

2 EXPERIMENTAL SETUP

2.1 Tribometer

Traditionally, tribometers such as pin-on-disk or cylinder-on-flat devices have been used to test the friction coefficient of a lubricant/surface pair for tribology research. Unfortunately, the setup and geometry of these devices create limiting conditions that allow testing only in a single lubrication regime instead of covering the entire spectrum from hydrodynamic to boundary lubrication. Real systems typically operate in more than one lubrication regime. For example, pistons in engines are designed to operate in the hydrodynamic lubrication regime. Each cycle, however, requires the piston to change directions twice, which forces it to come to a complete stop and thus operate in the boundary lubrication regime for a very short period of time [1]. Likewise, any reciprocating system will experience the same conditions. For this reason, characterizing friction in all regions of lubrication is essential for adequate design of sliding contacts.

To this end, a tribo-rheometer has been suggested that allows friction measurements to be attained using a parallel plate rheometer and any desired flat surface sample [20]. This tribo-rheometer can set either a constant gap or normal force and increase the rotational speed of the top plate while simultaneously measuring the required torque; thus, the shearing stress can be calculated for a range of Gumbel numbers.

Unlike previous tests where a single lubrication condition is studied, a dimensionless friction coefficient can be calculated from the tribo-rheometer data and can be plotted against the Gumbel number to attain a complete Stribeck diagram. This complete diagram exposes the frictional characteristics of the tested surface in the boundary, mixed, and hydrodynamic lubrication regimes. Figure 2.1 shows a schematic of the tribo-rheometer as it was used for the current study

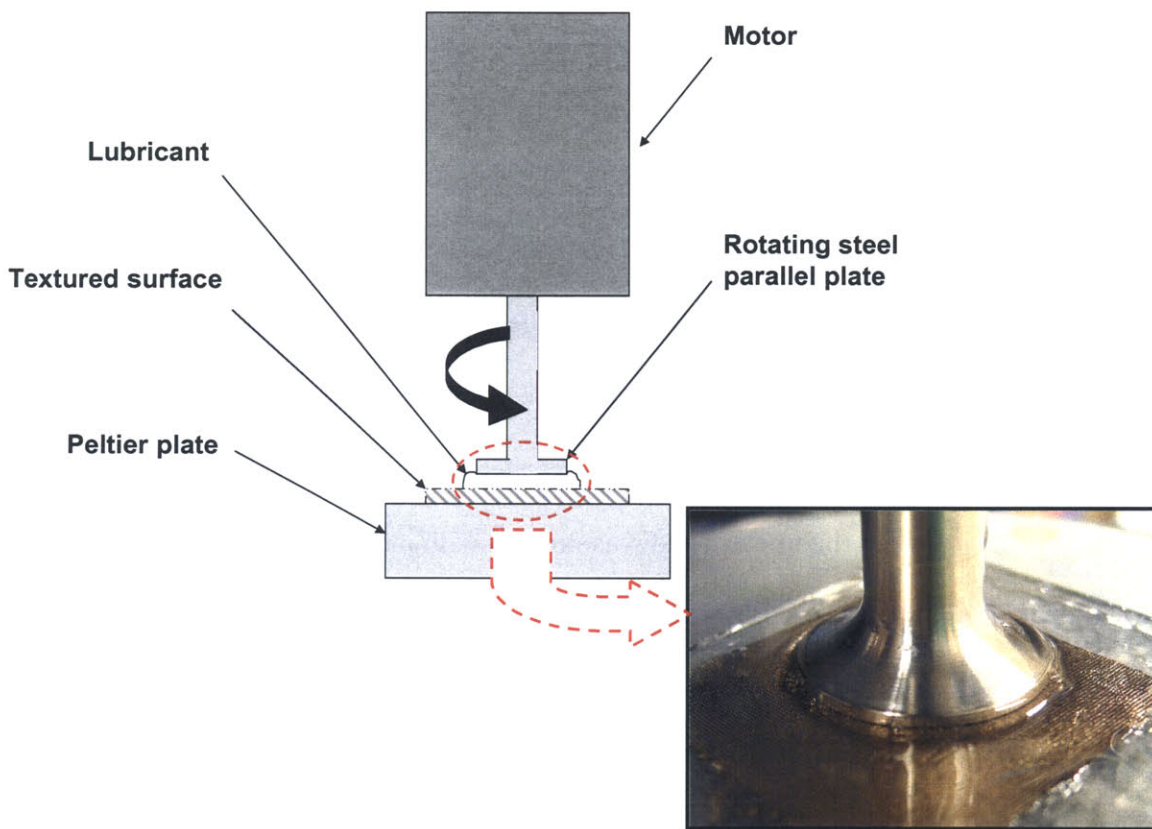


Figure 2.1. Schematic of the tribo-rheometer setup used for friction testing the textured nickel surfaces. The rheometer can set either a constant gap or normal force and ramp up the rotational speed of the top plate while simultaneously measuring the required torque; thus, the shearing stress can be calculated for a range of Gumbel numbers. Along with rheometer functions, this setup is also ideal because textured surfaces can easily be attached to the Peltier plate by melting a very thin layer of wax between the surfaces.

A detailed description of the theoretical considerations that went into the design of the tribo-rheometer can be found in Kavehpour and McKinley's paper [20]. For this study, a rheometer with a parallel plate geometry configuration was used for testing micro textured nickel surfaces. These surfaces were affixed to the rheometer, adjusted so that they were parallel to the rheometer head, and tested with a 20mm diameter steel parallel plate using different elastic and Newtonian lubricants.

2.2 Rheometer Setup

The AR2000 advanced parallel plate rheometer by TA Instruments is ideal for friction testing surfaces because of the wide range of testing parameters that can be controlled. For this study, the temperature of the surface and the normal force of the parallel plate rheometer head on the test surface were held constant while the angular velocity of the rotating rheometer head was ramped with increasing speed or decreasing speed depending on the desired outcome. The gap between the plates was allowed to change as necessary to maintain the constant normal force

Rheology Advantage Instrument Control AR© software by TA Instruments Ltd. is used as the user interface for controlling the instrument. From the computer interface, the information goes to a central controller and from the controller to the rheometer. To drive the rheometer shaft at a desired shear rate, velocity, or torque, the input to the rheometer motor is a torque. From the resulting motor response, an optical encoder on the drive shaft of the rheometer head relays the angular velocity or shear rate of the head

to the controller. A feedback loop adjusts the speed by sending a new torque requirement. The normal force is measured by force transducers in the Peltier plate, and the vertical position of the head is detected using an air bearing system in the rheometer.

Temperature is controlled by the Peltier plate and an external cooling system. Although the Peltier plate can easily raise the temperature using internal resistance heaters, trying to cool the plate via natural convection would require long cool-down periods. Instead, a cooling system is implemented where water is pumped through channels near the surface of the plate. The water is maintained at a constant, user-controlled temperature with a separate cooling system. An illustration of the rheometer control system is shown in Figure 2.2.

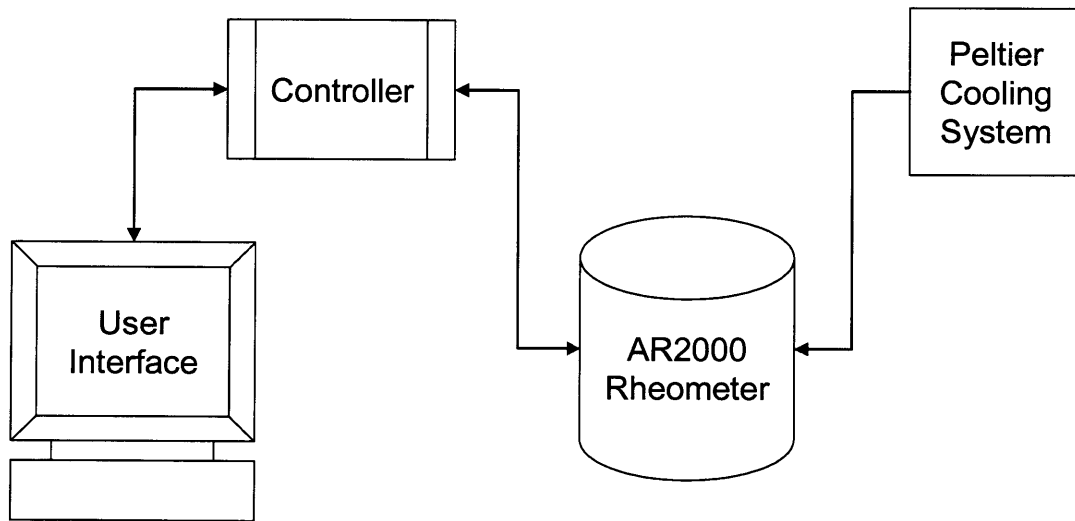


Figure 2.2. Illustration showing the components used to control the AR2000 torsional rheometer. The controller interprets the user inputs for velocity, torque, shear stress, or shear rate into torque requirements for the rheometer motor and uses a feedback control loop on an optical encoder to control the desired input and interpret the output. The Peltier cooling system cools the Peltier plate to the desired temperature, and the Peltier sends normal force and temperature information back to the computer interface through the controller.

In order to set up the rheometer for testing, the rheometer must first be configured and calibrated. The system inertia is initially calibrated without the parallel plate rheometer attached, and then the geometry must be mapped and the inertia calibrated with the parallel plate affixed to the system. These are internal functions that the system will perform on demand. After mapping the geometry, the system must be configured to recognize the zero-gap setting as the position where the rheometer head meets the surface of the Peltier plate. After these simple steps have been performed, the rheometer is calibrated and ready for the next step, which is to affix the textured nickel test specimen.

2.3 Textured Nickel Surfaces

Previous research has focused on the effect that surface texturing has on sliding friction under lubricated contact. Typically, carbon seals or ceramics were used as the textured surface due to the ease of fabrication using laser ablation techniques. For this study, the focus is to create a textured surface on a material commonly used in engineering applications and then test the sliding friction properties using an elastic fluid.

The desired material needed to have a high elastic modulus and hardness in order to be wear resistant and practical under heavily-loaded situations. It also needed to be corrosion resistant so that layers of oxidation did not build up on the surface during testing periods. Oxidation brings surface chemistry and the interaction between the surface and lubricant into question and adds more variables to an already complex question. Metals such as chrome, platinum, and nickel seemed to best satisfy the given

criteria. Once cost and ease of fabrication were considered, nickel was chosen as the best material for this study.

Although nickel was selected as the desired surface material, it did not necessarily need to be the only material used. Fabrication options included vapor depositing over a photoresist pattern to coat the photoresist or etching a pattern into a glass surface and then coating the glass with nickel. Although these options would ultimately lead to the outer surface being nickel, the collective modulus of the multi-layered structure would not be indicative of a true nickel modulus. The entire pattern was therefore required to be solid nickel. To meet this requirement, borosilicate glass was used only as a substrate, and the nickel pattern was applied onto the glass.

The resulting surface required a process of adding and removing layers on top of the glass. First, nickel is vapor deposited onto 2-inch square borosilicate glass plates using chromium as an adhesion layer between the nickel and the glass. On top of the vapor deposited nickel, photolithography techniques are used to apply a photoresin pattern for the desired texture. Once the pattern is applied, the surface is submerged in an electroless nickel plating solution so that only the vapor-deposited nickel that is not covered by the photoresist is plated. The plating builds up around the photoresist pattern, and at the desired thickness, the resin is removed to leave only the nickel pattern.

The texture patterns were selected based on conclusions from previous researchers [15-17, 19, 21]. Limitations were placed on the size of the pattern due to printing techniques. The photolithography masks were printed as transparencies, and the available printers were limited to a maximum resolution of 5080 dots per inch. The pattern is therefore comprised of tiny dots that are approximately $5\mu\text{m}$ in diameter.

Square patterns thus had a minimum corner radius of $5\mu\text{m}$, but the dot pattern led to discontinuous lines for features smaller than approximately $50\mu\text{m}$ in diameter. Due to control limitations with electroless plating methods, the feature depth was kept constant at $15\mu\text{m}$ with a tolerance of $\pm 5\mu\text{m}$.

Since electroless nickel plating is an autocatalytic process, the chemistry involved requires that the resulting surface actually be a nickel-phosphorus alloy. This alloy is advantageous in friction testing because electroless nickel-phosphorous coatings are considerably harder and more wear resistant than conventional electroplated nickel [22]. Our particular process resulted in a surface that was approximately 89% nickel and 11% phosphorus. The material properties of the surface are given in Table 2.1.

Table 2.1. Typical deposit properties of CR-MRN electroless nickel plating as reported by Plating Process Systems, Inc.

Phosphorous	10.5 – 12%
Hardness (VHN ₁₀₀) as plated	450 – 550
Density	8.2 g/cc
Internal Stress	0 to -15 kpsi
Tensile Strength	>100 kpsi

In order to attach the textured plate to the surface of the rheometer's Peltier plate as shown in Figure 2.1, the rheometer must first be calibrated and the zero-gap must be set. Once the system is configured, the next step is to affix the glass plate. With the rheometer head lifted off of the surface, place approximately 1 cm^3 of wax in the center of the Peltier plate. Lay the glass plate on top of the wax and lower the rheometer head until it makes contact with the plate. Using the rheometer control interface, set the normal

force to apply a constant 15N force on the surface. After the normal force had been set, raise the temperature of the Peltier to the melting point of the wax. The normal force on the surface of the plate will push the surface into a nearly perfect parallel configuration with the rheometer head while securely affixing it to the surface of the Peltier plate. Before the wax melts completely and while the glass plate and Peltier are still approximately 1mm apart, slowly cool the Peltier back down to 25°C while maintaining the 15N normal force.

Once the Peltier reaches 25°C, lift the rheometer head off of the surface. The glass plate with the nickel surface should now be securely affixed to the Peltier and configured to be parallel with the parallel-plate rheometer head.

2.4 Lubricant

For this study, a key hypothesis was that the elasticity of a lubricant could be tuned to interact with the surface texture in order to minimize sliding friction. For this reason, STP Oil Additive by First Brands Corporation was chosen as a lubricant due to its weakly viscoelastic properties. As a comparison, polydimethylsiloxane (PDMS) with approximately the same viscosity was chosen as the appropriate Newtonian fluid. One major advantage to PDMS is that it is available in a wide range of viscosities. Two different viscosity solutions of PDMS were compared to STP fluid. The particular fluid properties and rheology are discussed in Chapter 4.

Because the viscosity of a fluid is very sensitive to temperature, each test was run with the Peltier plate set at a constant 25 °C. Another consideration was that due to the

surface micro pores, it was impossible to clean the surfaces without chemical processes. Therefore, unless it was cleaned between uses, a particular surface could not be tested twice in the same area with different lubricants. This prevented lubricant mixing or the case where one lubricant might be filling the pores while the other is sitting on top. Lubricants were carefully stored and used so as to prevent deterioration and contamination during the length of this study.

CHAPTER 3

3 MANUFACTURE OF TEXTURED SURFACES

Surface micro texturing techniques largely depend on the material that is to be used as the contacting surface. Patterns made out of silicon or photoresin are among the easiest to fabricate due to the developments of photolithography techniques. Patterns cut into materials such as sapphire or ceramic, on the other hand, require a much different fabrication process that usually involves laser ablation of the surface material. For this study, a common engineering material was desired as the textured surface in order to allow more direct correlation to engineering applications. The desired material should have a high elastic modulus and hardness in order to be wear resistant, and it should be corrosion resistant so that layers of oxidation did not build up on the surface during the testing periods. Metals such as chromium, platinum, or nickel seemed to best satisfy the given criteria.

The next consideration was to determine which metal would allow the easiest fabrication methods. A literature review revealed that chemical etching, laser ablation, surface implantation, and machining techniques have been used for micro texturing in previous studies [14, 16, 18, 23, 24]. Chemical etching is a process where a pattern is placed on the surface of the piece and an etching chemical is allowed to dissolve the exposed surface. When the etchant creates a hole, both the bottom of the hole and the sides of the hole are exposed, so the sides begin to dissolve along with the layer of material on the bottom. As the hole reaches the required depth, the diameter has

increased and the sides of the hole are no longer vertical. Laser ablation is another common micro texturing technique, but depending on the material used, the laser can crack the surface [17] or it can melt some of the material and re-deposit it around the hole so that polishing is necessary to eliminate burrs on the surface. Another concern with laser ablation techniques is that the laser may work-harden the material around the hole so that the surface properties are not uniform. Surface machining is very limited to simple geometries and large features. Currently, machining techniques can typically reach a minimum channel size of about $100\mu\text{m}$.

Although it had not previously been used to micro texture surfaces for friction or wear testing, Dr. Abraham Stroock suggested recent MEMS fabrication techniques that explore the use of electroplating in combination with photolithography to create metallic structures on the micro scale [25]. Song and Ajmers also describe this technique and include details on which photoresist works well for plating and how to remove the photoresist negative after the electroplating process [26]. For this fabrication technique, a photoresist pattern is first applied to a nickel surface, and then the entire surface is electroplated. Since the resist is a non-conducting surface, it does not become plated; the exposed metal substrate, however, attracts the nickel ions and a layer of nickel is plated on the surface. This technique allows the resist to act as a negative pattern for the desired metal structure. After the plating, the photoresist is lifted off of the surface, and only the metal is left behind. Using this technique, although it is possible to plate a surface with many different metals, the most desirable for this study is nickel.

This technique seemed to be the best solution for applying a texture to a nickel surface, but after carefully following the techniques laid out by previous researchers, the

electroplating process was not successful for nickel plating on a layer of vapor deposited nickel. The plating resulted in the removal of the vapor deposited nickel layer instead of depositing a thick layer of nickel. Following many failed attempts at electroplating, a new method of nickel deposition using electroless nickel deposition was successful. Therefore, the process of fabrication was finalized. The final process, which will be later described in detail, requires that a thin layer of nickel is vapor deposited onto a glass substrate. Then a photoresist pattern is applied to the nickel surface and nickel is deposited in the negative space of the photoresist pattern. After depositing the nickel, the photoresist is removed to leave only the nickel texture on the surface. Figure 3.1 illustrates the layering process.

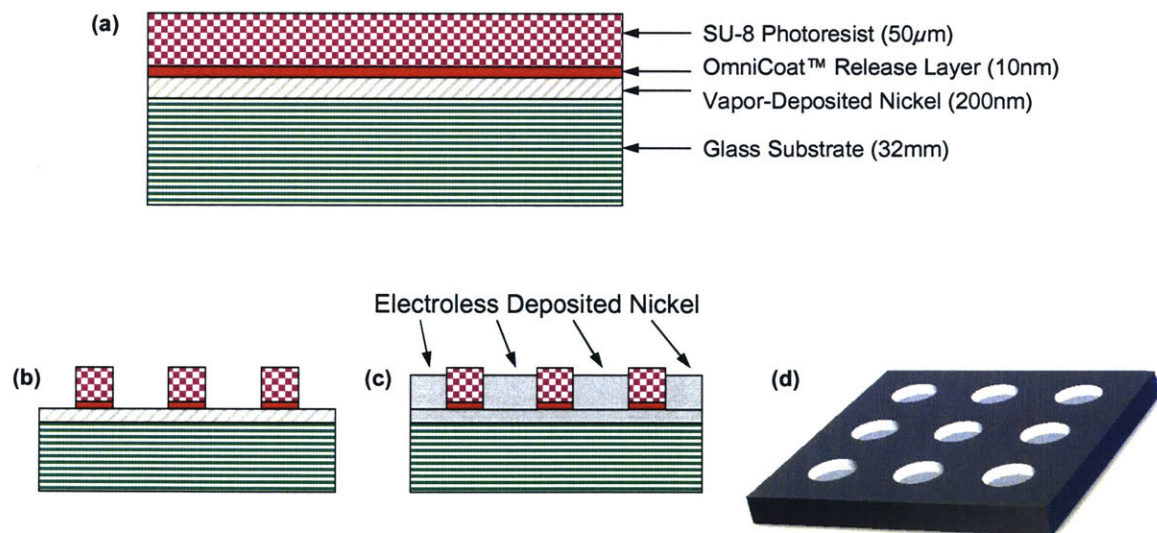


Figure 3.1. Illustration showing the layering required for the manufacture of nickel micro textured surfaces. First, a very thin layer of nickel is vapor deposited on a borosilicate glass substrate. A photoresist pattern is applied on the nickel surface and nickel is deposited in the negative space of the photoresist pattern. After depositing the nickel, the photoresist is removed to leave only the nickel texture on the surface.

3.1 Vapor Deposition

The first step in the fabrication process is to vapor deposit a layer of nickel on a 2-inch square, 3/8-inch thick flat piece of borosilicate glass. This glass was chosen as a substrate mainly because of its resistance to the chemical treatments necessary to clean the glass before the fabrication process. Glass is also a good substrate because it is rigid enough to resist bending due to internal stresses that result from the nickel plating process. In order to prepare the glass plates for the vapor deposition process, they were first cleaned in a standard piranha bath. This bath consists of soaking the surfaces in a solution of 1 part hydrogen peroxide and 4 parts sulfuric acid for at least 10 minutes. After soaking, the plates were rinsed with deionized water, dried, and dehydrated for 30 minutes at 160 degrees Celsius.

An electron beam vapor deposition system was used to vapor deposit a 2000 angstrom nickel seed layer. Because of nickel's poor adhesion properties to glass, a 500 angstrom thick layer of chromium was applied to the glass before applying the nickel. The system used allowed 3 samples to be coated at a time, and both the chromium and nickel could be deposited consecutively during the same run.

The samples were arranged in the vacuum chamber so that they would all receive the same amount of exposure to the metal vapors. Then, the chamber was pumped down to a vacuum of 3×10^{-6} Torr before the deposition was started. Once the desired vacuum was attained, first the chromium and then the nickel was deposited each by focusing an electron beam into a crucible of pure metal until the metal melted and vaporized, and

therefore depositing a uniform layer on the exposed glass surfaces. Thickness was determined according to electron beam intensity and exposure time. After deposition, the system was allowed to cool, and the metal coated surfaces were removed. Because the deposition occurred only on exposed surfaces, both the top and sides of the glass flats were coated with metal, but the back surface was not coated.

3.2 Photolithography

After depositing the nickel seed layer onto the glass substrate, the next step of the fabrication process is to create a photoresist pattern on top of the nickel seed layer. Patterns were designed to test the effect of pattern density and size and included the recommended optimum sizes and densities from previous research [15-17, 19, 21]. There is a minimum size limitation for photolithography texturing because a transparency mask of the pattern must first be available. Printing technology typically has a printing limit of 5080 dots per inch, so a surface feature is composed of tiny dots that are approximately $5\mu\text{m}$ in diameter.

Another limitation to photolithography is the aspect-ratio of the features. Applications that require the photoresist to be eventually removed from the surface typically use positive photoresists, which will easily dissolve in solvents such as acetone or methanol. Positive resists, however, can only be spun in thicknesses less than 20 microns, and the goal for this research is to attain features that are around 20 microns deep. The best option for taller features is to use SU-8, a negative photoresist. SU-8 is

not easily removed with solvents, but using OmniCoat™ from MicroChem corporation as a base/release layer, the photoresist can be lifted off using RemoverPG™, another MicroChem product. SU-8 is a very viscous photoresist and can be spun into thicknesses greater than 100 microns.

3.2.1 OmniCoat™ Release Layer Application

Before applying the photoresist and release layer to the surface of the nickel-coated glass samples, they were first dehydrated in a convection oven at 180 degrees C for 20 minutes. After dehydration, the OmniCoat™ release layer was spun onto the sample and baked for 1 min. on a 200 °C hotplate according to the instructions given by MicroChem and shown in Table 3.1.

Table 3.1. Details for applying the OmniCoat™ release layer.

Thickness	20nm
Dispense	2mL
Spin	500 rpm for 5sec with acceleration of 100 R/s 3000 rpm for 30 sec with acceleration of 300 R/s
Bake	200 °C hotplate for 1 min

After baking the OmniCoat™, the surfaces are allowed to cool before starting the SU-8 process.

3.2.2 SU-8 Photoresist Application

The SU-8 photoresist application process is summarized in Table 3.2 and described below in detail. Because the substrate is a 3/8-inch thick glass plate rather than a silicone wafer, the bake times for the SU-8 are altered from the MicroChem instructions to allow for the difference in thermal properties between the two substrates. Overall the bake times increase slightly, but the thick glass allows for very uniform heating of the photoresist layer.

Spin

The first step in processing the photoresist is to spin coat the surface. To do this, approximately 4mL of SU-8 is dynamically dispensed onto the surface, creating as few air bubbles as possible. Once on the surface, the photoresist is allowed to spread until almost reaching the sides, at which point the surface is spun at 500 rpm to allow the resist to completely cover the surface. Once covered, the surface is moved to hotplates for the pre-bake and softbake steps.

Softbake

Once the softbake is complete, the surfaces must cool to room temperature before UV exposure. Depending on the room temperature and humidity, the bake times may need slight adjustment. If the photoresist surface is still tacky after cooling from the softbake, it should be baked again at 95 °C at approximately 1 minute intervals until the surface is no longer tacky at room temperature.

Expose

While the surface is cooling after the softbake, a transparency mask is selected to create the desired texture pattern. This pattern should be the negative image of the desired texture since the photoresist will ultimately be removed to leave only a nickel pattern. The pattern should be free of dust and creases in order to get a more consistent pattern. When the surface is cool, it is placed on the aligner with the mask on top covered by a glass slide to hold the mask in place. Expose the surface to near UV light (350-400nm) at 400 mJ/cm^2 .

Post Expose Bake

Following exposure, the surface is baked at $65 \text{ }^\circ\text{C}$ for 1 minute and then moved to $95 \text{ }^\circ\text{C}$ for 6 minutes. This final bake cross-links the exposed photoresist film.

Develop and Rinse

Developing the resist is performed using a spin process. While the surface is spun at 100 rpm on a coater, it is sprayed with propylene glycol monomethylether acetate (PGMEA) in 5 second intervals for 2 minutes. After developing, the PGMEA is rinsed with isopropyl alcohol and allowed to spin dry. A visual inspection should be done under a microscope to check if the SU-8 has been fully developed. It is essential that the developing is complete and that there is no residue left in corners or at the base of the resist posts since they will act as the negative pattern for the final nickel plating.

If the resist is not completely developed, redo the spin develop step for 30 second to 1 minute intervals and repeat the rinse step.

Table 3.2. Photolithography process for SU-8 100 on borosilicate glass substrate

Thickness	50 μ m
Dispense	3mL
Spin	500 rpm for 5sec with acceleration of 100 rpm/s 1500 rpm for 30 sec with acceleration of 300 rpm/s
Pre-bake	65 °C hotplate for 7 min
Soft bake	95 °C hotplate for 24 min
Expose	350-400nm at either 400 mJ/cm ²
Post Exposure Bake 1	65 °C hotplate for 1 min
Post Exposure Bake 2	95 °C hotplate for 6 min
Develop	Spin develop using PGMEA for 2 min
Rinse	Briefly rinse with isopropyl alcohol

3.2.3 OmniCoat™ Develop

The final step in completing the photoresist mask is to develop the OmniCoat™, which is done by O₂ plasma removal. The surface is placed under a 200 mTorr vacuum while the power is maintained at 75 W for 3 minutes in order to completely remove the exposed OmniCoat™ from the surface of the vapor-deposited nickel. After removing the OmniCoat™, only the nickel surface not covered by the photoresist pattern is exposed and will be plated by the nickel electroless plating process.

3.3 Electroless Nickel Plating

Initial research into the fabrication of micro-scale nickel patterns led to the conclusion that it would be best to electroplate nickel over an applied photoresist pattern [26]. Nickel electroplating is the deposition of a nickel coating onto an object by applying a negative charge onto the surface and immersing it into a solution which contains a nickel salt. The metallic ions of the salt carry a positive charge and are attracted to the conducting surfaces. When they reach the surface, the negatively charge provides the electrons to reduce the positively charged ions to metallic form. The particular salt solution used for plating was designed specifically to deposit nickel with a very small grain size so that there could be a more precise shape to the micro-scale pattern.

Several attempts were made at electroplating vapor-deposited nickel surfaces, but each attempt resulted in the nickel being dissolved around the electrical connection, as shown in Figure 3.2. It is unclear why this result was occurring, and many attempts were made to change the type and material of connector along with trying to place the connection in the bath or keep it out of the bath. After consulting literature and experienced engineers in the field, alternative solutions were explored.

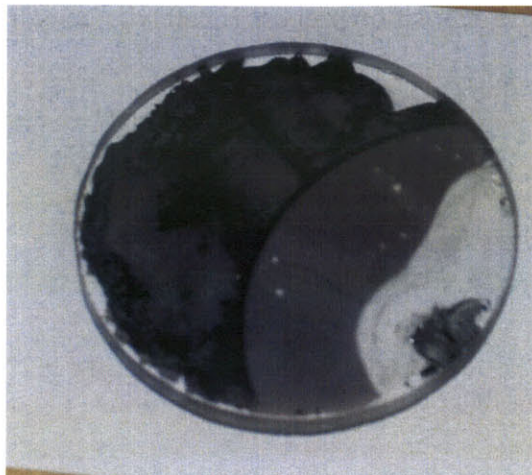
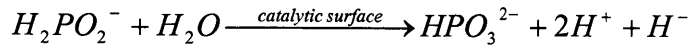


Figure 3.2. Photograph of the nickel remaining on a borosilicate glass plate after an attempt at electroplating the surface. The electroplating process etched away the layer of vapor deposited nickel and chromium rather than plating on a thick layer of nickel.

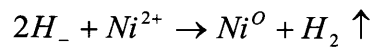
3.3.1 Electroless Nickel Plating Chemistry

The most promising alternative solution was electroless nickel plating. Electroless plating is a “controlled autocatalytic chemical reduction process for depositing metals” [22]. Once the deposition is initiated on a catalytic surface, plating continues at a rate linear with time. For nickel hypophosphate baths, such as the one used for this study, the essential chemicals for the reaction are a nickel salt, hypophosphite, and a salt which acts both as a buffer and a mild complexing agent for nickel. Other substances can be added to improve bath stability or increase plating rates. Plating can only be initiated on catalytic metals such as nickel, cobalt, steel, and other active metals. Non-catalytic metals and non-metals can also be plated, but appropriate conditioning steps must first be performed. Once the plating process is initiated on any surface, deposition continues because electroless nickel is itself catalytic.

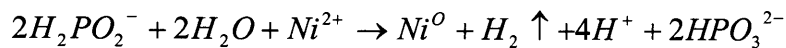
The first step in the deposition process is catalytic dehydration of hypophosphate with a hydride transfer to the catalytic surface [22]:



The hydride ions can then react with nickel ions to produce the deposit:



The total reaction can be represented by



Electroless nickel plating produces a nickel-phosphorus alloy rather than a pure nickel coating. Typical deposits contain 3 to 15% (wt) phosphorus.

After several attempts at trying to mix electroless plating baths from chemical recipes, it became more obvious that the chemical processes involved in the reduction and phosphide formation are not completely understood. A bath that is not well-balanced can quickly degrade and lead to a plate out, where the nickel rapidly precipitates out of the solution. Eventually, a commercial electroless nickel bath was able to give consistent, good results. The plating bath results in a high phosphorous, corrosion resistant surface and is developed and sold by Plating Process Incorporated as their CR bath.

3.3.2 Bath Preparation

In order to use the electroless nickel bath, two solutions, CR-M and CR-N, are carefully mixed together and heated according to the directions given by Plating Processes, Inc. The pH must be maintained around 4.8 using dilute ammonia hydroxide, and the temperature range for plating is between 88–92 °C. The bath will not plate at lower temperatures, and it could decompose at higher temperatures. Once the bath is prepared and stabilized at the desired temperature, it is ready for plating.

3.3.3 Nickel Plating

A surface that is covered with a photoresist pattern and ashed is lowered into the bath and secured so that it remains fully submerged. The bath should be stirred vigorously in order to dislodge air bubbles on the surface that result from the chemical plating process. It was determined, however, that stirring too vigorously resulted in pattern inconsistencies. In order to obtain the most uniform pattern, the orientation of the surface should be change every 15 to 30 minutes; a simple 90° rotation works well. Figure 3.3 shows a photograph of a surface that has not been rotated in the bath, and Figure 3.4 shows the result of a surface with an identical pattern, but it has been rotated every 15 minutes for the first 2 hours and every 30 minutes for the last hour. As bubbles collect around a photoresist post, they rise to the top of the post but remain there until enough gas is collected to gain the buoyant force required to dislodge it from the surface. For this reason, surfaces that are not rotated often are formed with a low region at the top of the post where less plating has built up due to air bubble accumulation.

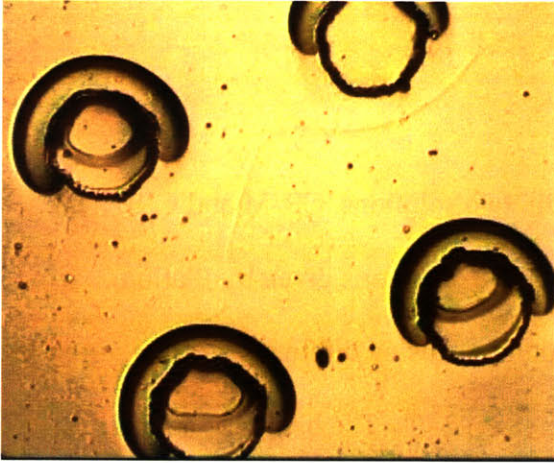


Figure 3.3. 100µm10% surface shows a non-uniform pattern due to bubble accumulation during the nickel plating.

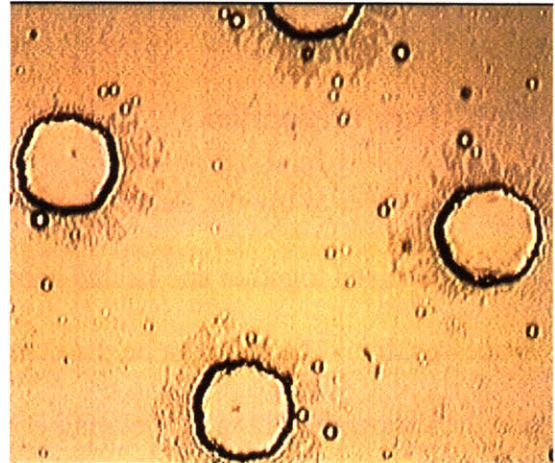


Figure 3.4. B100µm10% surface was rotated frequently during plating, so the holes are well-formed.

Plating time depends on bath pH, nickel activity, and bath temperature. If the bath remains around 90 °C, a nickel layer of approximately 15µm will be deposited after 3 hours of plating. To determine the exact layer thickness, the surface thickness should be carefully measured before plating and compared to measurements during plating. To measure the thickness of the surface during plating, it should be removed from the bath and rinsed with deionized water. After measuring, rinse the surface again with DI water before returning it to the bath in order to reduce the impurities on the surface. During the plating process, the bath should also be monitored for impurities and loose nickel pieces. If the bath becomes contaminated with visible impurities, it should be filtered through a 5-20µm membrane filter and reheated to plating temperature.

Once the desired thickness is reached, remove the surface from the plating bath and rinse it a final time with deionized water. The electroless plating bath is no longer needed, and it should be disposed of according to appropriate chemical safety procedures.

3.4 OmniCoat™ Removal

Once the nickel plating process is complete, the final step in the surface manufacturing procedure is to remove the OmniCoat™ release layer. First, heat 100mL of RemoverPG™ to 80 °C. After the solution is stabilized at the desired temperature, place the textured surface in the solution so that it is completely immersed and agitate for 30 minutes. Remove from the solution after 30 minutes, rinse with distilled or DI water and dry using forced air. If some of the photoresist posts remain on the surface, try to blow them off using the canned air. Typically, the photoresist is visible without the aid of a microscope if you look at the plate profile instead of looking directly from the top. Figure 3.5 shows a surface with the photoresist posts before it is submerged in the plating solution. The posts can be seen without the aid of magnification, although it is not necessarily possible to identify the post shape or size. A microscope may be necessary in some cases. If the posts are still in place, repeat the RemoverPG™ bath until all posts have been removed from the surface. Dry the surface completely and store it in a dry place taking care not to scratch the surface.

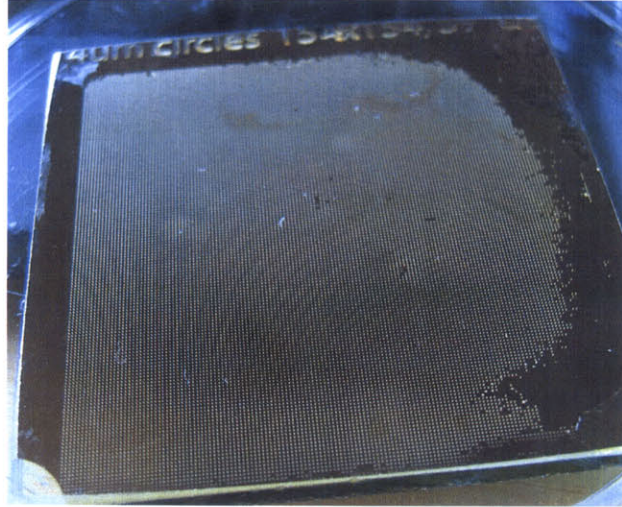


Figure 3.5. Photograph of a surface with photoresist posts before the nickel plating process. The posts can be seen without the aid of magnification, although it is not necessarily possible to identify the post shape or size.

If any part of the nickel has delaminated from the surface of the glass, there could very possibly be liquid trapped between the two layers. In cases such as this, it is best to dry the surfaces in a warm oven (90 °C) for an hour to make sure the fluid is completely evaporated so that it does not leak out of surface cracks during testing and contaminate the lubricating fluid.

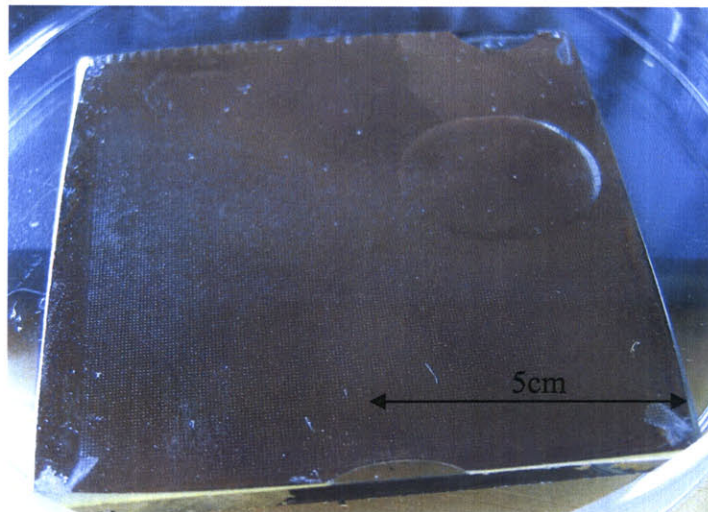


Figure 3.6. Photograph of 50 μm 2.5% micro textured surface. The micro texture is difficult to see without magnification, but the surface is visibly consistent except for the small section of delamination in the upper right corner.

CHAPTER 4

4 LUBRICANT RHEOLOGY

In order to determine the effect of lubricant elasticity on the friction coefficient of micro textured surfaces, three fluids were tested. Two fluids were weakly viscoelastic lubricants – the main test fluid was STP Oil Additive by First Brands Corporation, and the second was Valuecraft Oil Treatment. The fluid used as a comparison to the elastic lubricants was polydimethylsiloxane (PDMS), a viscous Newtonian fluid. A summary of the properties for each lubricant is given in Table 4.1.

Table 4.1. Selected lubricant properties. Three lubricants were tested to determine the effect of lubricant elasticity on the friction coefficient of micro textured surfaces. STP and Valuecraft were weakly elastic fluids, and they were compared to PDMS, a viscous Newtonian fluid.

Fluid	Viscosity (Pa·s)	Density (kg/m³)	Relaxation time (s)
PDMS (30k)	30.0	(unknown)	(Newtonian)
STP	16.1	879	0.076
Valuecraft	5.1	899	0.029

4.1 STP Oil Additive Rheology

STP Oil Additive is a complex viscoelastic fluid. Because of proprietary restrictions, First Brands Corporation would not release a full fluid characterization, nor would they share the chemical composition of the fluid. Therefore, extensive testing was required to fully characterize the fluid and understand the elastic properties.

The first test performed measured the fluid viscosity using a cone and plate geometry on a torsional rheometer. While maintaining a constant plate temperature, a 6mm, 1° cone was used for a flow test where the shear rate was ramped from 0.05 s⁻¹ to 5000 s⁻¹. Due to the rod climbing properties of viscoelastic fluids, only the data below a shear rate of 220 s⁻¹ was used to model the fluid. Above that value, the fluid began to climb up the sides of the cone and there was not a continuous layer of fluid beneath the cone for testing. Using data between the values of 0.1 and 220 s⁻¹, the test results showed that STP was a shear-thinning fluid with a zero shear rate viscosity of 16.02 Pa·s (Figure 4.1).

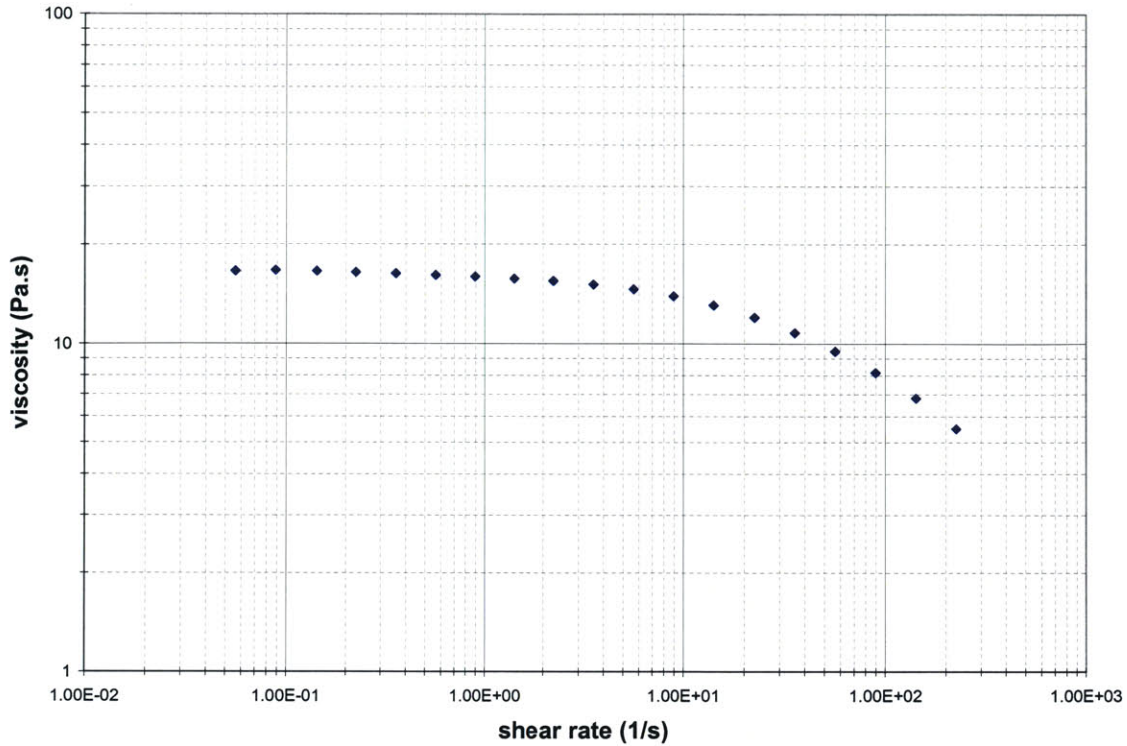


Figure 4.1. Viscosity plot of a flow test with STP Oil Additive on a torsional rheometer using a cone and plate geometry. The downward trend at high shear rates is characteristic of a shear-thinning, non-Newtonian fluid.

Using commercial Rheology Advantage software, the rheometer shear data was fit to a Carreau model in order to characterize the shear-thinning nature of the fluid.

While the Carreau model typically allows for an infinite-rate viscosity parameter, the viscosity of STP became insignificant at high shear rates, so that term was neglected.

The equation to model viscosity is given below [27]:

$$\frac{\text{viscosity}}{a} = \frac{1}{((1 + c * \text{rate})^2)^{d/2}}$$

where a is the zero rate viscosity

c is the consistency

d is the rate index

and rate is the applied shear rate.

In order to take a more careful look at the elastic properties of STP, an extensional flow test was performed using a capillary break up extensional rheometer (CABER). For our particular setup, the aspect ratio was 1.75, the starting diameter was 6mm, and the Hencky Strain was 1.52. The results are shown in Figure 4.2. When compared to a straight line, it is evident that the tail end of the data curves upward, which is characteristic of a second-order viscoelastic fluid [28].

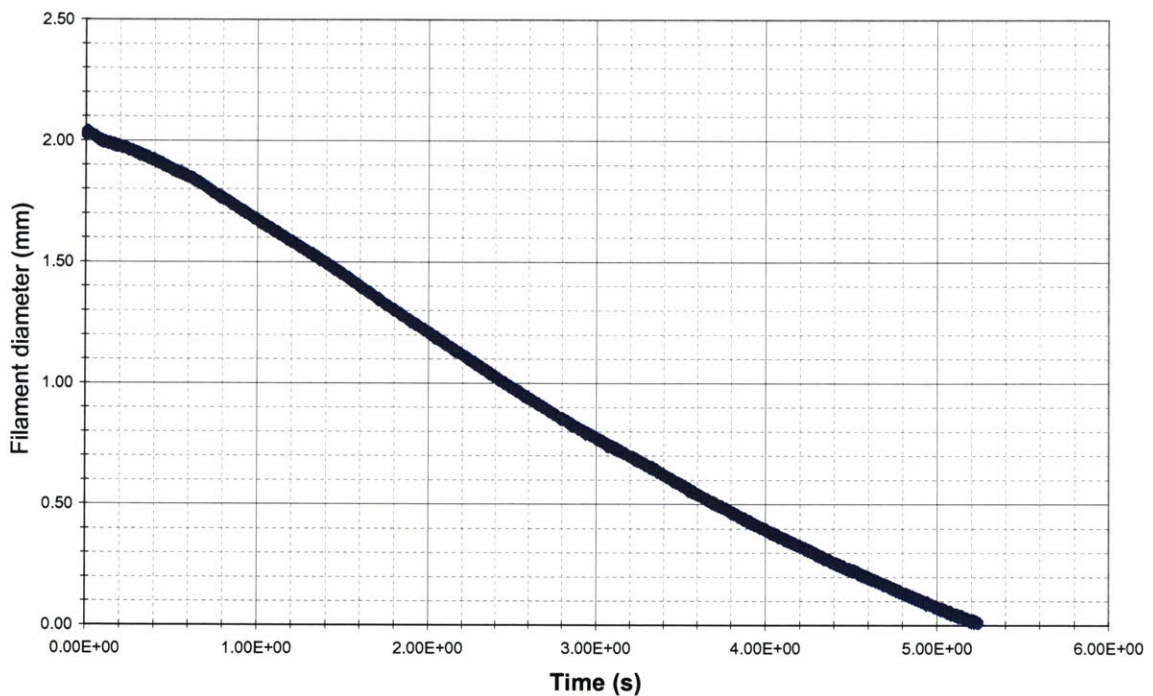


Figure 4.2. CABER test on STP to determine fluid elasticity. When compared to a straight line, it is evident that the tail end of the data curves upward, which is characteristic of a second-order viscoelastic fluid.

This CABER data can be modeled as a second order fluid to attain a measurement for the relaxation time [29]. The data is fitted to the equations below:

$$y = \sinh^{-1} \left\{ \left(\frac{h}{4B(2x-1)} \right) \right\}$$

$$\frac{1}{2} (e^{2y} - 1) + y = \frac{1}{2B} (t_c - t)$$

where $B = \frac{\lambda\sigma}{3\eta_0 R_0}$

t_c = critical time

h = stretching distance

t = time from start

x = constant

λ = relaxation time

σ = surface tension

η_0 = zero shear rate viscosity'

R_0 = initial filament radius

Figure 4.3 shows a plot of the collected data with the fitted second order fluid (SOF) model compared to the Newtonian model. There is good agreement between the two curves, which indicates a good fit. From this model, the relaxation time for STP can be calculated as 0.09 s. The second order fluid model is explained in more detail in Appendix C.

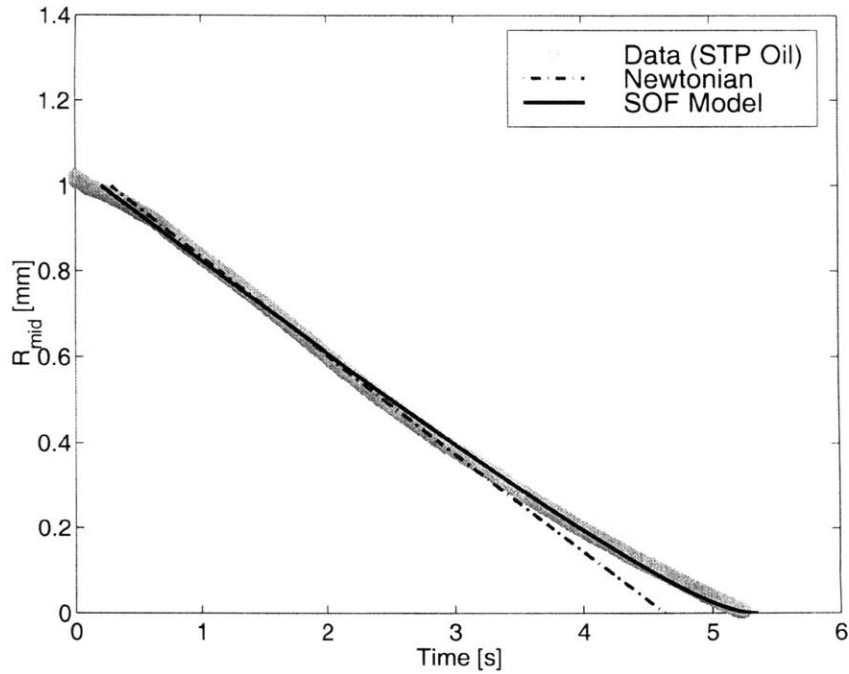


Figure 4.3. Plot of the collected CABER data for STP oil additive with the fitted second order fluid (SOF) model compared to the Newtonian model. There is good agreement between the SOF and data curve, which indicates that the model can accurately characterize the fluid.

As a second look at the fluid elasticity, an oscillation test was performed on a torsional rheometer using the same cone and plate geometry as that for the viscosity testing. For the oscillation test, oscillation stress was held constant at 3 Pa while the angular frequency was swept from 0.1 to 100 rad/s. The resulting data shown in Figure 4.4 once again confirms that the fluid is mildly elastic because the curves for G' and G'' curve and will eventually cross at a particular angular frequency that indicates the fluid relaxation time.

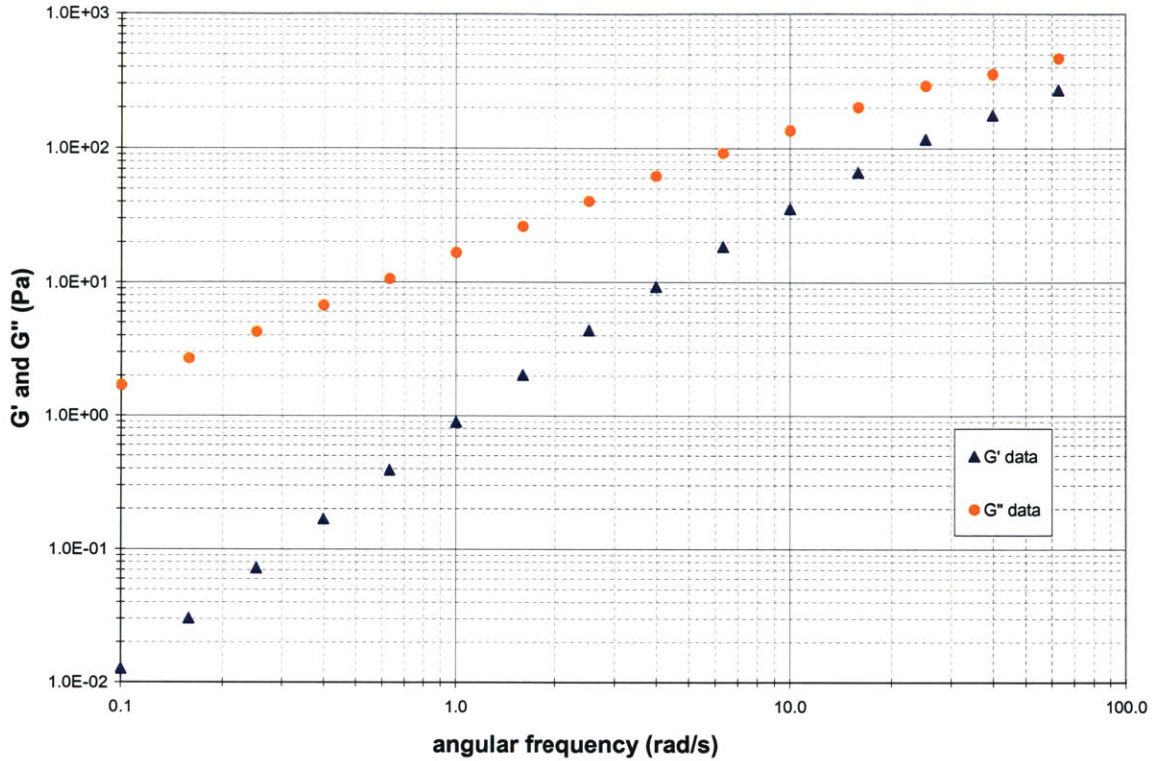


Figure 4.4. An oscillation test with STP fluid. This test performed using a cone and plate geometry on a torsional rheometer shows a non-Newtonian trend for the G' and G'' data.

Another method for finding the fluid relaxation, λ , time at particular angular frequencies, ω , is to use the G' and G'' data in the equation

$$\lambda(\omega) = \frac{G' / \omega^2}{G'' / \omega}$$

The relaxation time is plotted versus angular frequency in Figure 4.5. From this graph, a characteristic relaxation time, λ , is determined to be the value that the curve asymptotically approaches as it goes to very low angular frequencies. The value for λ is determined to be approximately 0.076 s for STP fluid.

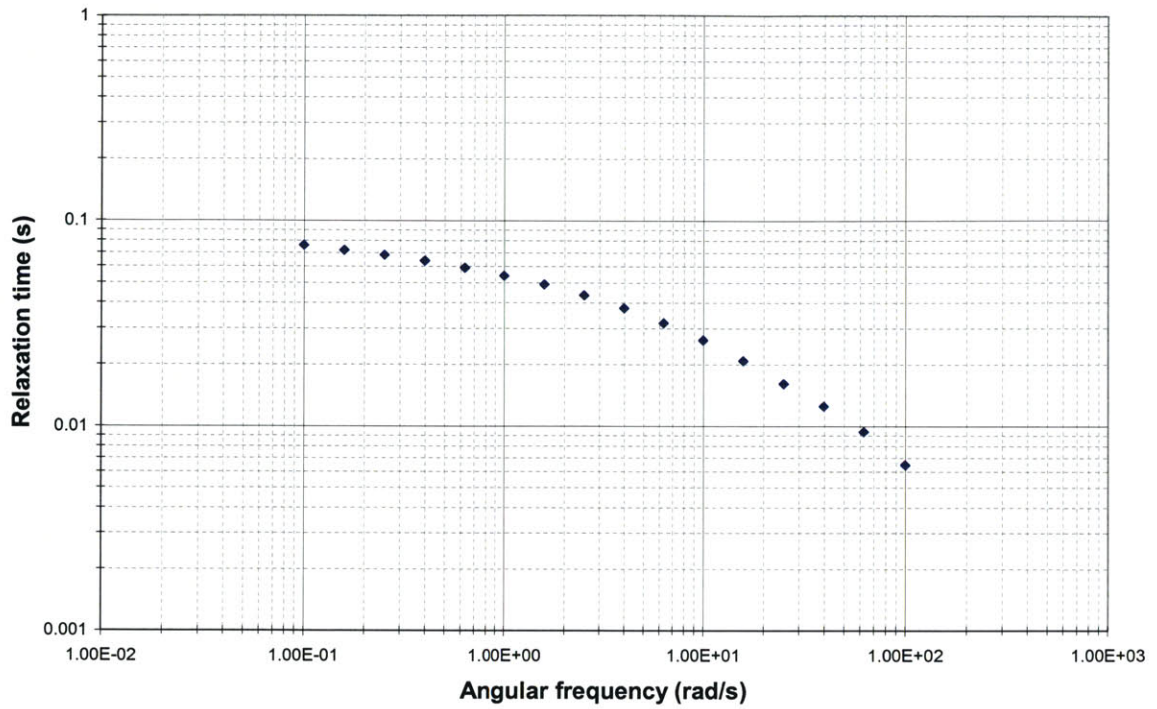


Figure 4.5. Relaxation time for STP fluid calculated using G' and G'' from oscillation tests on a torsional rheometer. From this graph, a characteristic relaxation time, λ , is determined to be the value that the curve asymptotically approaches as it goes to very low angular frequencies.

Finally, the fluid elasticity can be summarized using the Maxwell equations:

$$G' = \frac{G(\lambda \omega)^2}{1 + (\lambda \omega)^2}$$

$$G'' = \frac{G(\lambda \omega)}{1 + (\lambda \omega)^2}$$

4.2 PDMS Rheology

In contrast to STP fluid, PDMS is a Newtonian fluid, so it does not have any elastic properties. Although it is specified for the particular fluid, the viscosity can be tested using the same torsional rheometer setup with the 6mm 1° cone and plate geometry. Figure 4.6 shows that the fluid is not shear thinning, but instead the viscosity remains constant across the entire range of shear rates.

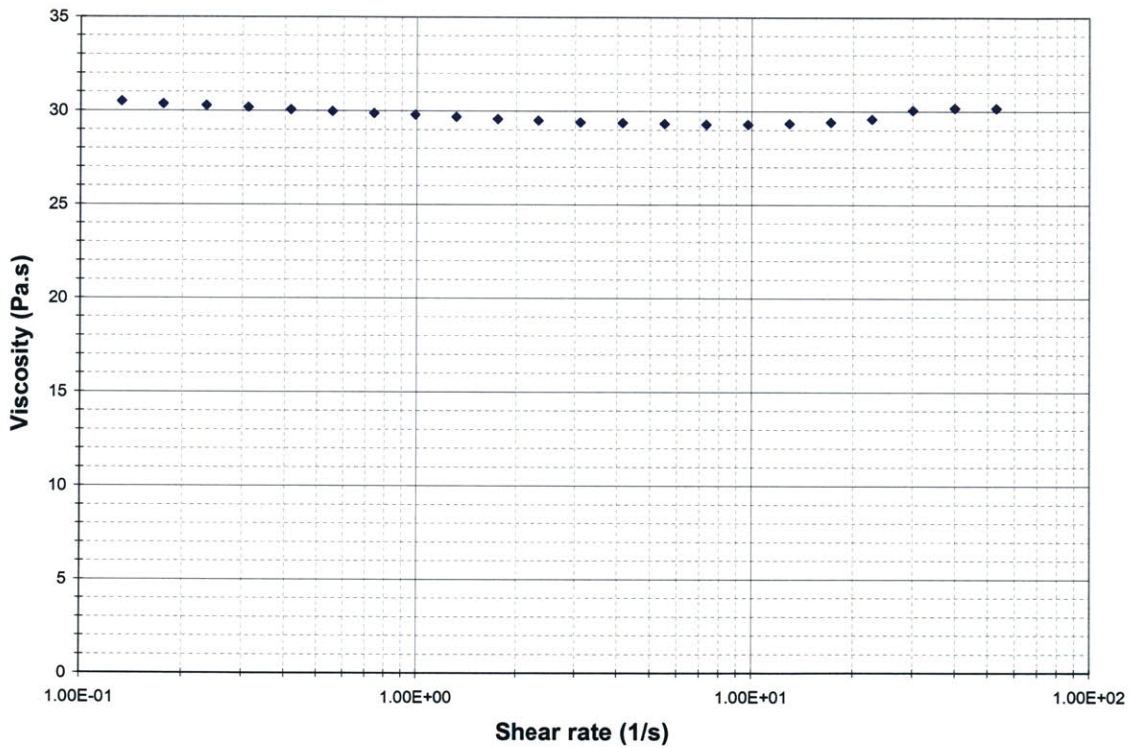


Figure 4.6. Torsional rheometer data showing the Newtonian viscosity behavior of polydimethylsiloxane (PDMS). Because the viscosity remains constant and does not decrease at high shear rates, it is not a shear-thinning fluid like STP.

Again, although the PDMS fluid is not specified as having any elasticity, an oscillation procedure is performed on the rheometer to verify the fluid assumptions and to act as a comparison for the STP fluid. Figure 4.7 shows that the curves for G' and G'' do not cross at an angular frequency near conditions at which it is used for friction testing, and they vary linearly with angular frequency. These conditions indicate that PDMS acts as Newtonian fluid for the running conditions used in this study.

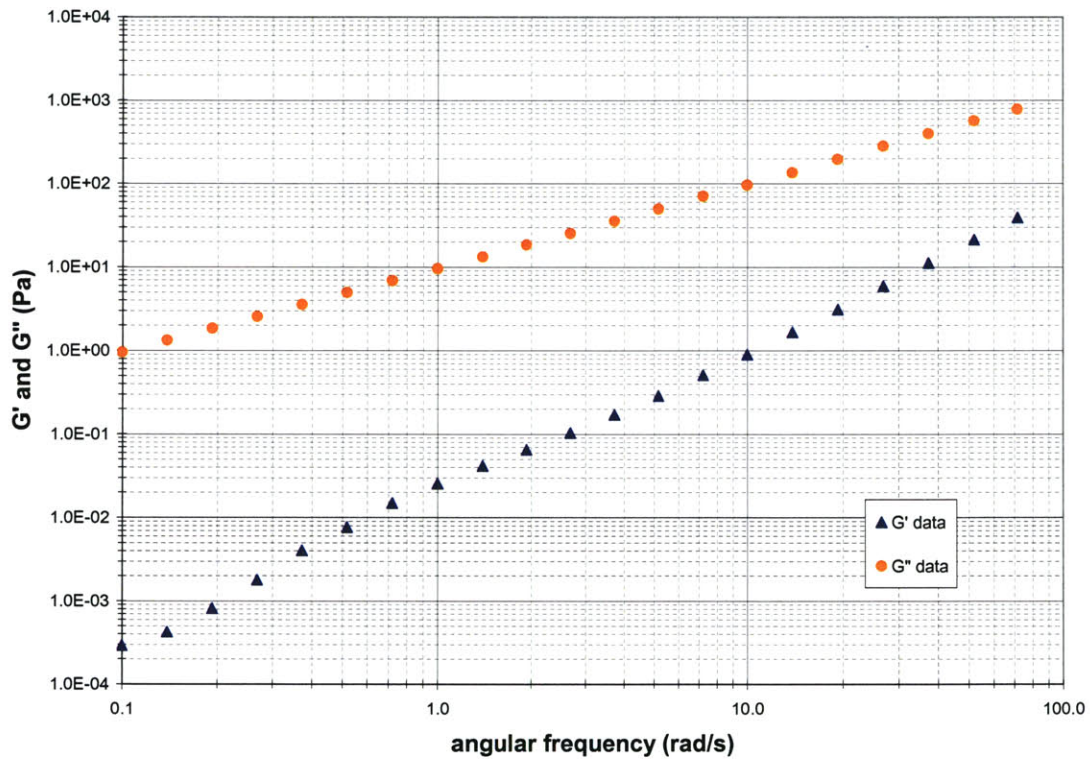


Figure 4.7. An oscillation test on PDMS fluid using a cone and plate rheometer geometry shows a Newtonian for the G' and G'' data.

A CaBER test was not performed on the PDMS fluid because the oscillation test verified that there in fact was no elasticity in the fluid.

CHAPTER 5

5 EXPERIMENTAL PROCEDURES

5.1 Flow Parameters

The only parameter that was varied during a friction test was the angular velocity, ω , of the parallel plate. The range of the angular velocity and the constant normal force for each test was determined by the type of lubricant used. The desired result of each test was a complete Stribeck curve, so if high normal forces were used, then higher velocities were needed whereas if a lower normal force was selected, then the rheometer needed to run at slower velocities to reach the boundary lubrication regime. Ideally, tests were performed at higher velocities (15N) to decrease testing time and allow the rheometer to reach steady state at each particular angular velocity. Certain testing conditions, however, resulted in high friction coefficients. In order to reduce the required shear stress, the normal force was decreased from 15N to 10N. Typically, the exact testing conditions were determined during the run-in period.

Each test consisted of affixing the selected textured plate to the Peltier plate and setting up the parallel plate geometry on the torsional rheometer, as described in Chapter 2. Once the rheometer was set up, the rheometer was configured to perform a flow test procedure at 25°C with a constant normal force. The angular velocity was either set to decrease from between 1 and 100rad/s to 0.01rad/s for run-in procedures, or it was set to increase from 0.001 rad/s to 100 rad/s for surface testing.

Often, the shear stress would exceed the acceptable value at high angular velocities, so the test would be terminated at values less than 100rad/s. If at any time the shear stress exceeded the safe operating values, the test would be terminated, the surface would be wiped clean, and a new test would be run.

5.2 Run-In Procedure

A run-in procedure is always performed before running the testing procedure. This run-in requires the same surface preparation and testing parameters, but the velocity is typically decreased from 100rad/s to 0.01rad/s at intervals of only 5 points per decade of decreasing velocity. The rheometer is allowed to make at least one complete rotation at each velocity point before accepting the average shear stress and moving on to the next data point.

After the run-in procedure is complete, the rheometer head is wiped cleaned using methanol. The nickel textured surface is simply wiped off, removing as much lubricant as possible without leaving dust or fibers from the cleaning cloth. Once the surface is cleaned, it should be visually examined from dust or unwanted particles and cleaned a second time if necessary. When it is satisfactorily clean, new lubricant is applied and the testing procedure is started.

5.3 Testing Procedure

After each surface was run-in, a second velocity sweep was performed. The data from this second run was used for surface analysis because it was generally more consistent and a better representation of the true surface friction characteristics than the data from the run-in period. As previously described, the resulting data from a velocity sweep depends on whether the surface is accelerating or decelerating, so for the second run, the velocity was always increased from 0.001rad/s.

For velocities ranging from 0.001rad/s to approximately 0.05rad/s, the rheometer was typically only allowed to make a single full rotation before accepting the average shear stress for that velocity and moving on to the next speed. It was important to accept data points only after complete rotations because the shear stress could change in value as much as 5000 Pa during a single rotation, but the variation was very periodic with a period of a full rotation. Once velocities of greater than 0.05rad/s were reached, a single rotation took less than 5 minutes to complete, so the rheometer was typically allowed several full rotations before accepting the average shear stress.

5.3.1 Configuration for STP Oil Additive

As expected, STP fluid significantly decreased the coefficient of friction for the textured surfaces, so higher normal forces and larger ranges of angular velocities were required to obtain the entire lubrication spectrum. Originally, a normal force of 10N was used to test the surface, but it was determined that a normal force of 15N would allow for faster testing velocities without destroying the nickel surface.

STP fluid was run-in at a 15N normal force with the angular velocity decreasing from 100 to 0.01rad/s. Due to the high starting velocity, a conditioning procedure was used where the rheometer was run at testing conditions and an angular velocity of 50rad/s for 5 seconds before performing the run-in procedure. This prevented the fluid from foaming due to the very rapid acceleration to 100rad/s.

For the testing procedure, the angular velocity was increased from 0.001 rad/s to 100rad/s, and the shear stress was measured at 7 points per decade of angular velocity. Because of the very slow angular velocity, the test sometime took up to 10 minutes to reach a steady state value for the shear stress. After steady state was reached, the first point was discarded since the average value would be lower than expected as a result of the ramp-up time.

5.3.2 Configuration for PDMS Lubricant

Testing for Newtonian PDMS lubricant is the same as that for STP, but the run-in period for PDMS is started at 10rad/s instead of 100rad/s because the higher viscosity typically leads to shear stresses that are damaging to the surface above 10rad/s. For the testing procedure, however, the angular velocity is allowed to increase until shear stresses of approximately 30,000 Pa are reached.

5.4 Data Processing

The recorded data was viewed using a commercial package specific to the AR2000 rheometer. With this package, the desired variables were selected for each test, and after viewing the data, it was copied and pasted into Microsoft Excel for further analyzing. Using the spreadsheet environment, Gumbel numbers and coefficients of friction were determined for the data and used to compare the different surfaces and lubricants.

CHAPTER 6

6 RESULTS

The detailed results are presented under three major headings corresponding to the experiments used to verify the testing procedure, then those used to explore the effects of surface texture and finally the experiments to determine the role of the lubricant rheology. For reference purposes, a summary of the major results can be found at the end of this chapter.

6.1 Procedure Verification

6.1.1 Stribeck Diagram

The testing procedure discussed in Chapter 5 is designed to produce a Stribeck curve that includes all major lubrication regimes by running an angular velocity sweep at a constant temperature and normal force. As a result of this test, the shear stress required for rotation is measured at particular values of angular velocity, as shown in Figure 6.1.

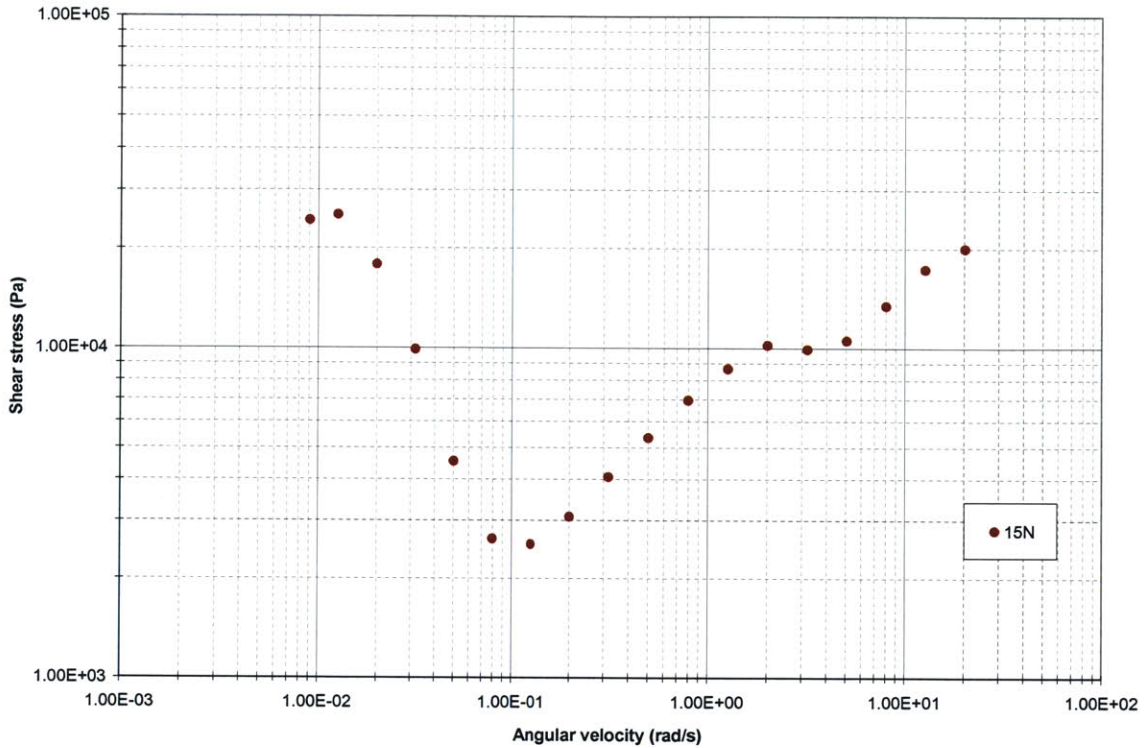


Figure 6.1. Raw data showing the variation of shear stress with angular velocity at a constant 15N normal force. Tests run with the triborheometer are set to maintain a constant normal force while sweeping the relative angular velocity of the rheometer head. The shear stress required for rotation is measured at particular values of angular velocity.

For this research, the dimensionless Gumbel number and friction coefficient are used to construct a Stribeck diagram that characterizes a particular lubricant/surface pair. Figure 6.2 shows the results from a test performed using the same lubricant/surface pair as that in Figure 6.1, but the normal force is now 10N rather than 15N. According to theory, the velocity and viscosity data should be normalized with the particular applied normal stress to form the dimensionless Gumbel number, while the resulting shear stress will also be normalized with the normal stress to obtain the coefficient of friction. The resulting Stribeck curves for tests with different loads are identical despite the change in conditions (Figure 6.3).

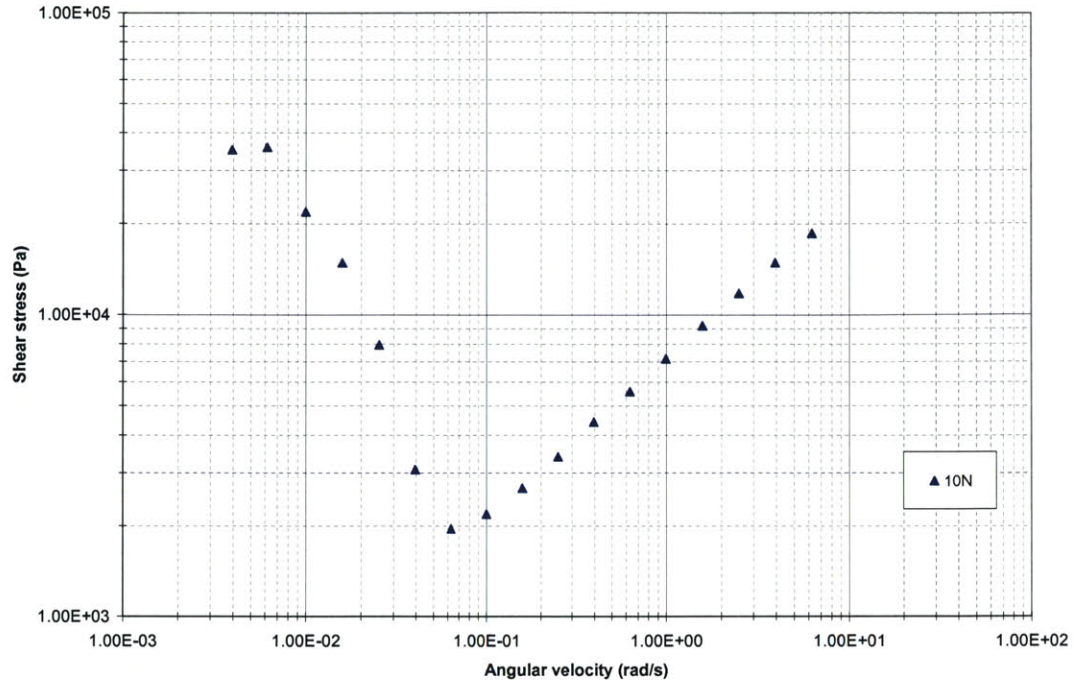


Figure 6.2. Raw data showing the variation of shear stress with angular velocity at a constant 10N normal force. This is data taken from the same surface as Figure 6.1, but the normal force is reduced to 10N.

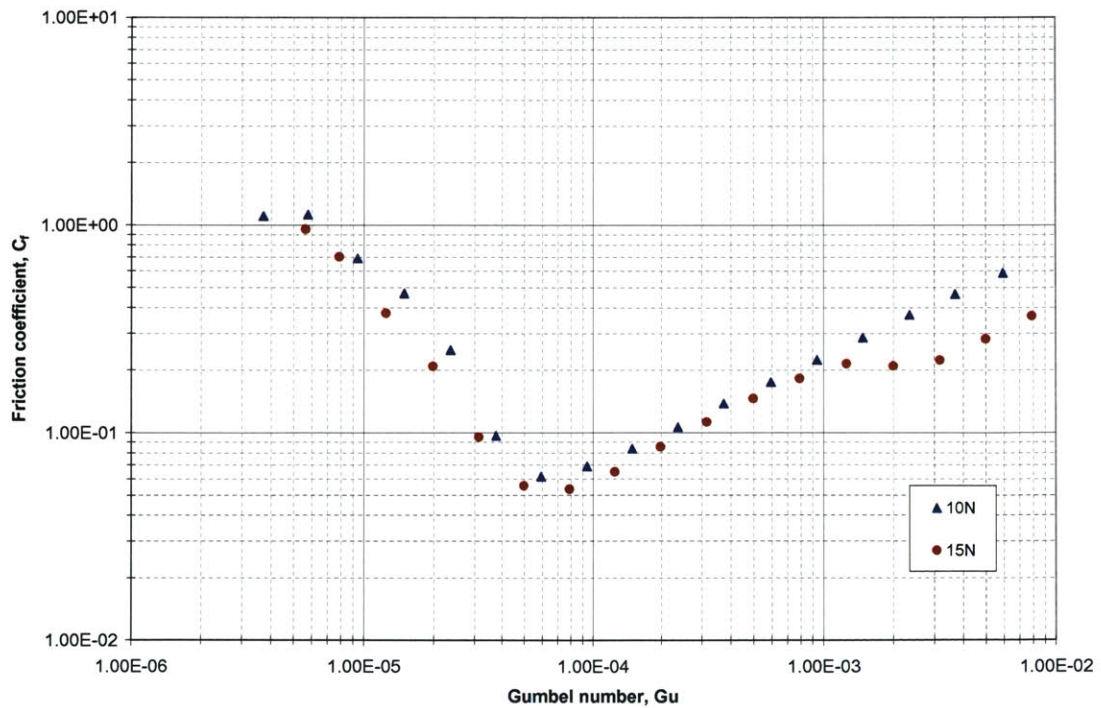


Figure 6.3. Comparison of surface data when it is normalized using the Gumbel number and friction coefficient. Using the dimensionless groups, the resulting Stribeck curves for tests on the same surface but with different loads are identical despite the change in testing conditions.

Similar to comparing the Stribeck curves of different normal forces, a fluid with two different viscosities should also result in the same Stribeck curve when the data is normalized using the Gumbel number. As an investigation, polydimethylsiloxane (PDMS) can be obtained in a very wide range of viscosities. PDMS with a viscosity of 10 Pa·s is tested and the resulting data is plotted on a Stribeck diagram along with the data from PDMS having a viscosity of 30 Pa·s. The resulting graph in Figure 6.4 shows that the change in fluid viscosity does not affect the calculated Gumbel number. The Stribeck curve for STP fluid is given on the same graph as a comparison. Although STP has a similar viscosity of 16 Pa·s, it is an elastic fluid with very different properties than PDMS. These property differences result in drastically different friction characteristics.

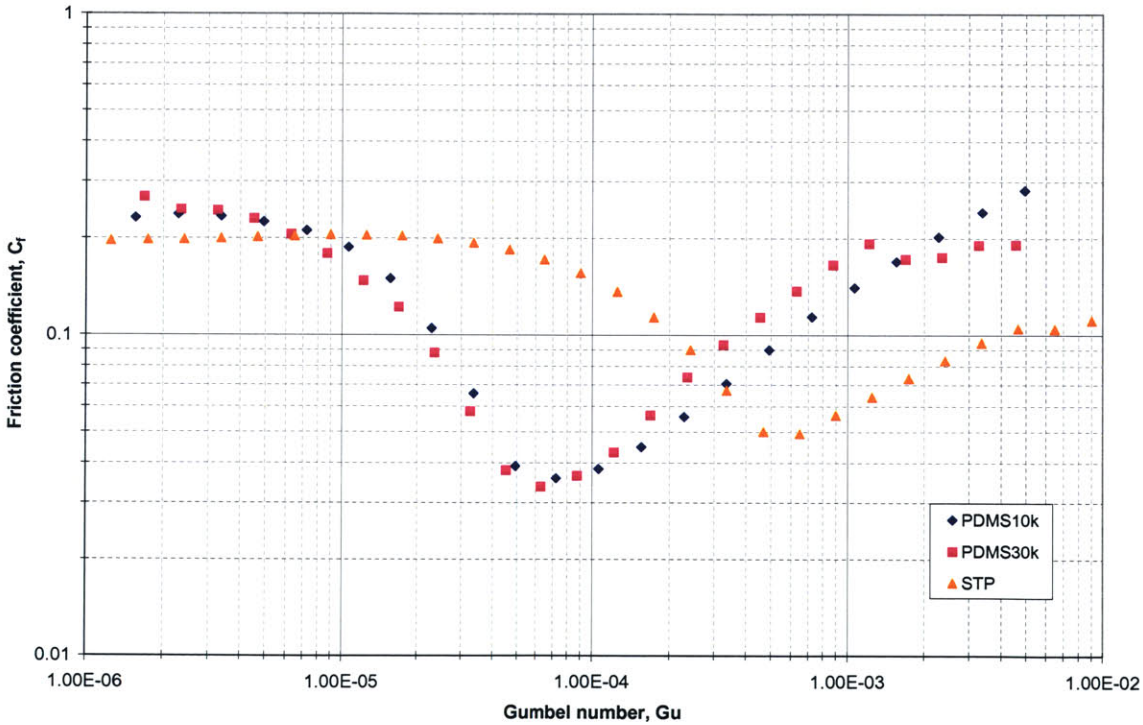


Figure 6.4. Illustration of the Stribeck curve consistency between two fluids with the same fluid properties but different viscosities compared to that of a different fluid with similar viscosity.

6.1.2 Run-In Procedure

Due to surface wear, initial surface chemistry, and other unknown interactions between the lubricant and surface, a surface will often realize different frictional properties during the initial testing period at a particular location. Surfaces are therefore required to undergo an initial procedure before collecting data for accurate friction testing. The initial procedure is typically referred to as the run-in or break-in period, and after this period has been experienced, the subsequent testing will result in consistent data unless the system undergoes heavy wear. Figure 6.5 illustrates the difference between the Stribeck curve during the run-in period and the curve obtained during the test directly following the run-in period. As outlined in section 5.2, the surface is cleaned and the lubricant is replaced between tests.

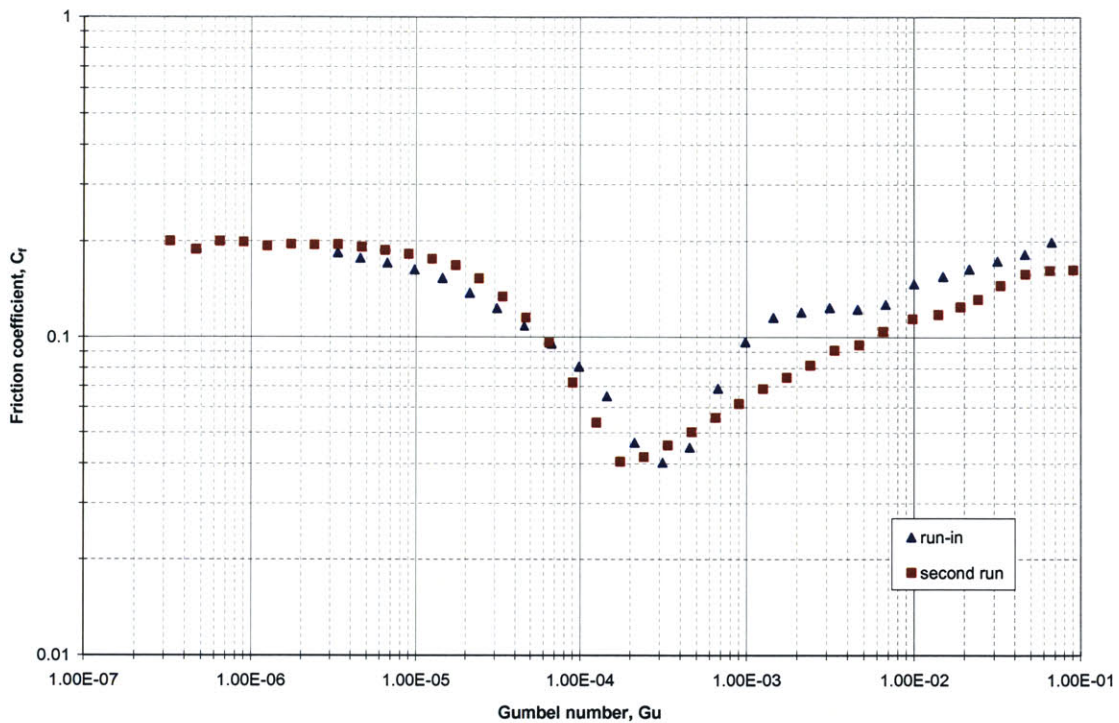


Figure 6.5. Effect of run in period. A run-in period is performed at each location before surface data is collected. As shown in the graph, the run-in period exhibits different frictional characteristics than subsequent tests.

6.1.3 Increasing/Decreasing Velocity Curve Shifts

During the duration of this study, it became evident that the Stribeck curve would shift depending on whether the relative angular velocity was tested with increasing speed or with decreasing speed. Figure 6.6 illustrates this phenomenon and shows that it is very consistent over many iterations of testing a surface at the same location and is not just a result of surface wear. Because of the curve shifts, all of the results reported for particular patterns are those taken with the angular velocity increasing in speed unless otherwise noted. This allows more accurate comparison of both Gumbel number and friction coefficient.

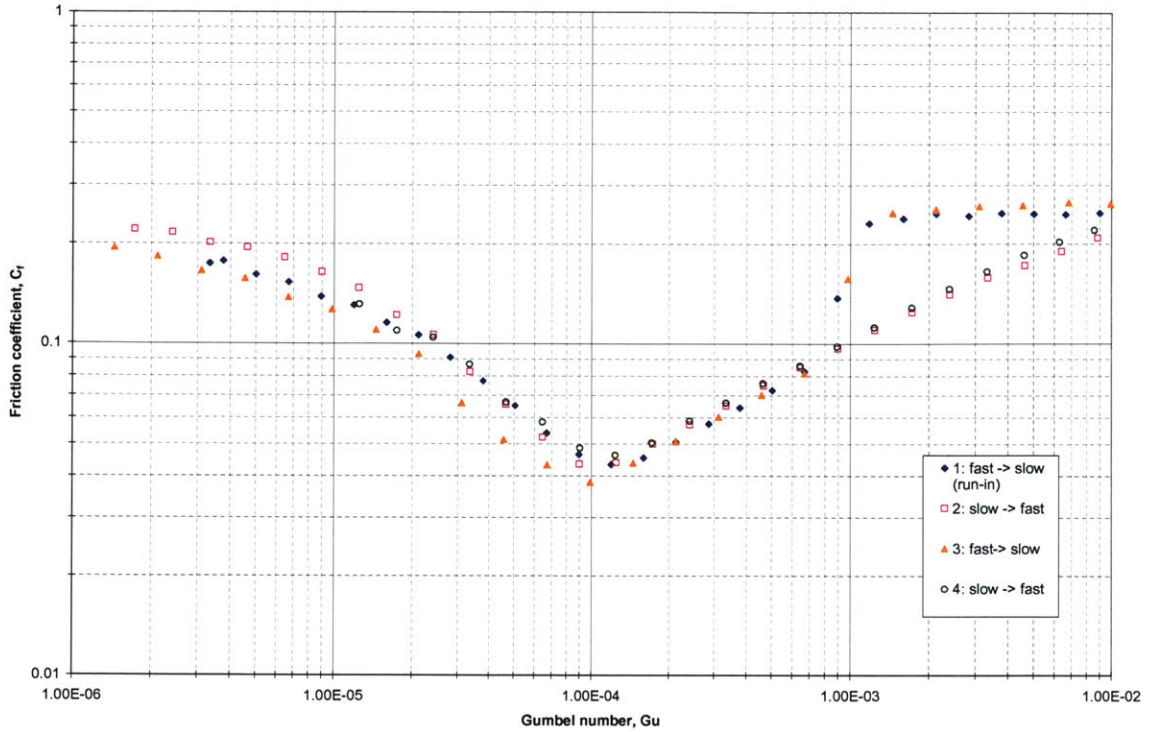


Figure 6.6. Stribeck diagram showing the data shift due to increasing or decreasing velocity. This figure illustrates the curve shift and shows that it is very consistent over many iterations of testing a surface at the same location. All of the results reported in this study are taken with the angular velocity increasing in speed to allow more accurate comparison of surfaces.

6.2 Results of Surface Texturing Effects

The results shown in this section are data collected from particular surface/lubricant pairs. Unless otherwise specified, a run-in procedure has been completed on each surface, and the data given is the Stribeck diagram of the second run, which typically starts at a velocity of 0.001rad/s and ends around 50rad/s.

Table 2 gives a summary of the surfaces fabricated and the tests performed on each surfaces. In some cases, two surfaces were fabricated with the identical pattern. For this situation, the second surface fabricated is given a “B” before the pattern name to

differentiate it from the first. Appendix B shows pictures of each pattern under magnification.

Table 2. Summary of the patterns fabricated and tested for this study.

	STP	PDMS 30Pa·s	PDMS 10Pa·s	Second Surface
Control (flat)	X	X		X
50um 1%	X	X		X
50um 2.5%	X	X		X
50um 5%	X	X	X	X
75um 5%	X			
100um 5%	X	X		X
100um 10%	X	X		X
125um 15%	X			X
125um 20%	X			

6.2.1 Surface Data

Each surface was tested multiple times using STP Oil Additive as the lubricant in order to determine consistency and to get an average Stribeck curve. For many of the patterns, a second surface was fabricated in order to determine robustness of the original surface data. The data presented in this section shows photographs and multiple tests for each pattern along with comments on particular surface or testing conditions. Each data set has been normalized to produce a Stribeck curve.

6.2.1 A) Control Surface

The control surface is a nickel plated, flat surface. The same procedure was used to fabricate this surface as that for the textured surface except no photolithography pattern was applied. There are no observable imperfections in the surface, and the surface roughness is less than $1\mu\text{m}$ when measured with a digital micrometer under 40X magnification. Figure 6.7 shows Bcontrol surface under 40X magnification.

No photographs were taken of the original control surface, but it also has a surface roughness of less than $1\mu\text{m}$.

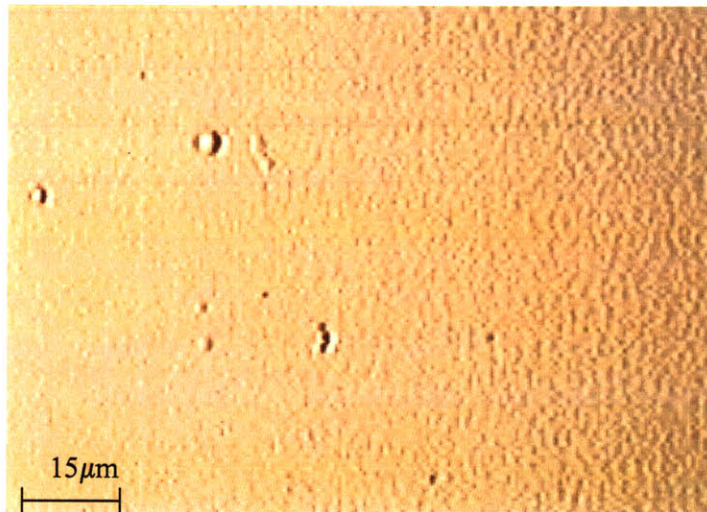


Figure 6.7 Bcontrol under 40X magnification.

Figure 6.8 gives the Stribeck diagram for the tests performed on each control surface. The curves are smooth, and both are approximately consistent with each other, which indicates good testing conditions.

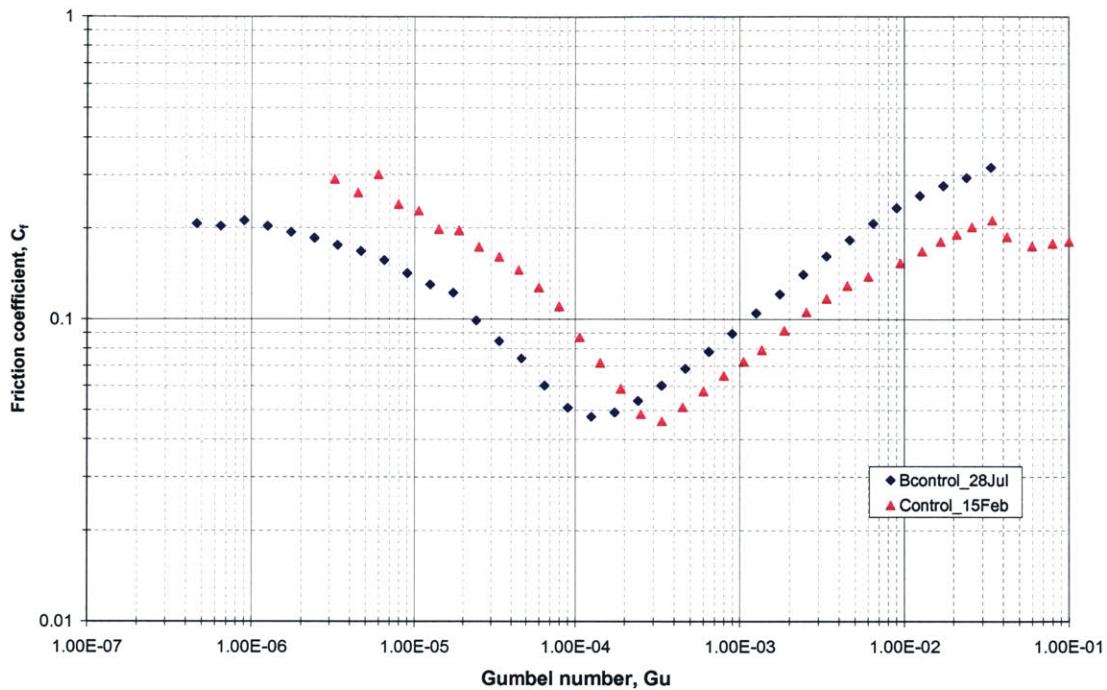


Figure 6.8. Stribeck diagram of the control surfaces with STP fluid as the lubricant.

6.2.1 B) $50\mu\text{m}$ Diameter Pores at 1% Area Density

The original $50\mu\text{m}1\%$ surface was not rotated during the nickel plating process and therefore developed air pockets above the holes. These pockets are only $5\mu\text{m}$ deep, while the central pore is $17\mu\text{m}$ deep. Surface photographs, such as the one shown in Figure 6.9, show that almost 80% of the holes have a maximum diameter of approximately $100\mu\text{m}$ rather than $50\mu\text{m}$. This is a rough approximation, but it is a better representation of the actual surface than the original surface parameters. Given the information from the photographs, the area density of the features is actually 2.2% rather than 1%. The surface pattern for the B $50\mu\text{m}1\%$ surface is fabricated as desired with minimal air pockets on the surface (Figure 6.10).

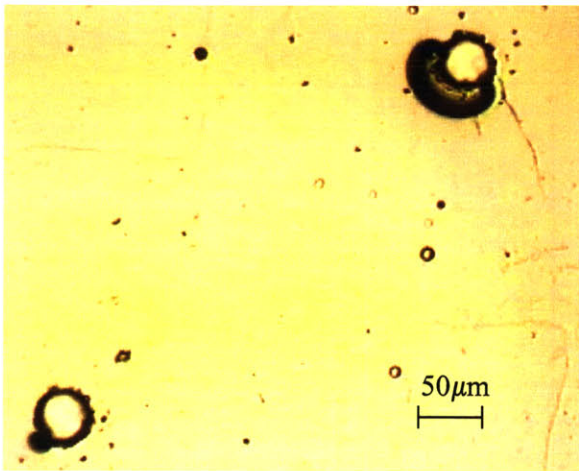


Figure 6.9. 50um 1% surface photograph.

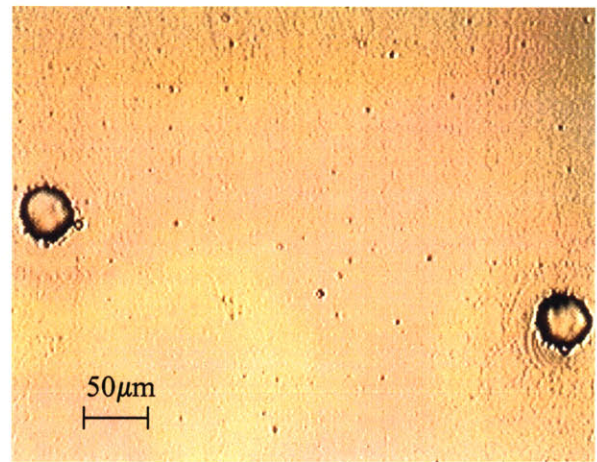


Figure 6.10. B50um 1% surface photograph

The Stribeck diagram of both the 50 μm 1% and B50 μm 1% surfaces (Figure 6.11) does not show great consistency in the surfaces. If the lower curve is neglected, however, the two remaining curves show reasonable agreement for the frictional characteristics of the surface. Data such as this indicates that the surface was either somehow contaminated during one of the testing runs, or there was a surface flaw at one particular location on the surface.

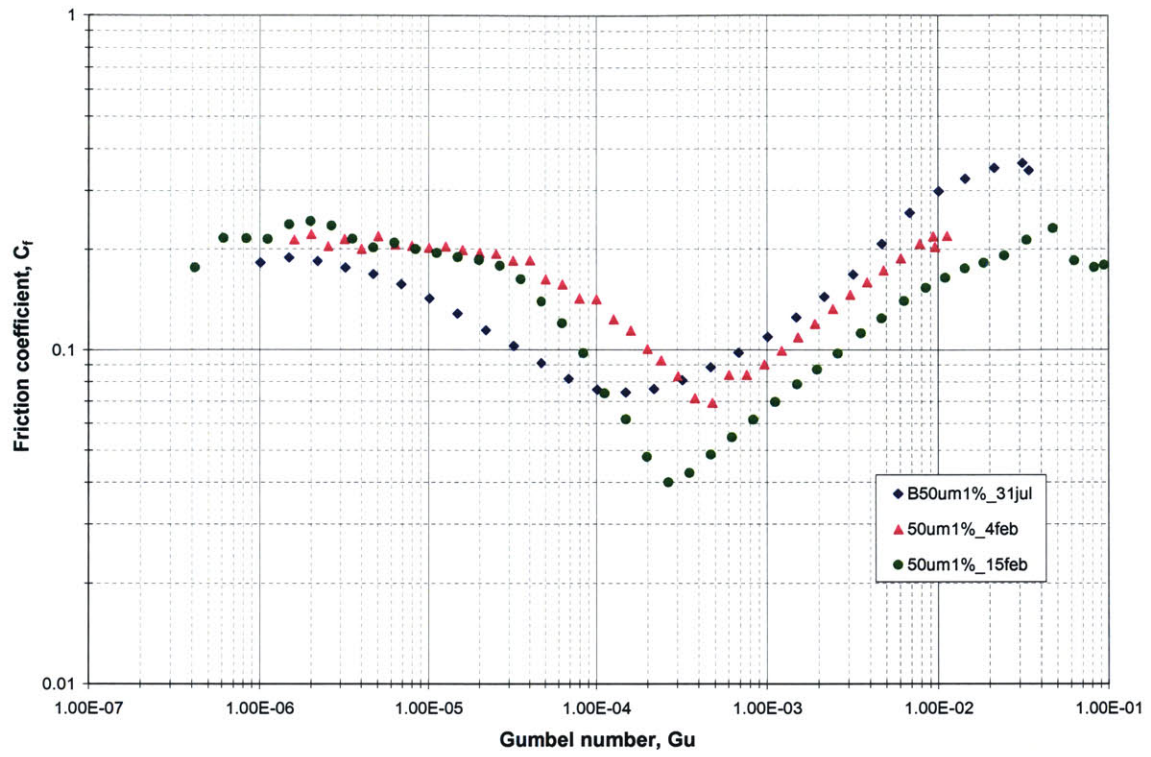


Figure 6.11. Stribeck curve for the surfaces having a pore diameter of $50\mu\text{m}$ and 1% feature density with STP oil as the lubricating fluid.

6.2.1 C) 50 μ m Diameter Pores at 2.5% Area Density

Two surfaces were fabricated to test the 50 μ m 2.5% pattern. The first surface, shown in Figure 6.12, was not rotated during the plating process, so the hole diameters are not 50 μ m as expected. When measured using a microscope and rough estimation techniques, it was found that 30% of the holes have a diameter closer to 125 μ m, while the other 70% remain at 50 μ m in diameter. The increase in hole size for part of the surface increases the area density of features from the desired 2.5% to 6.5%. The plating process was more predictable for the B50 μ m2.5% surface, so the holes are formed properly (Figure 6.13).

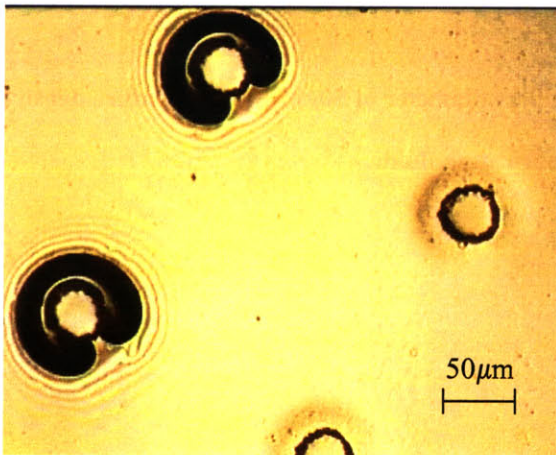


Figure 6.12. 50 μ m 2.5% surface photograph.

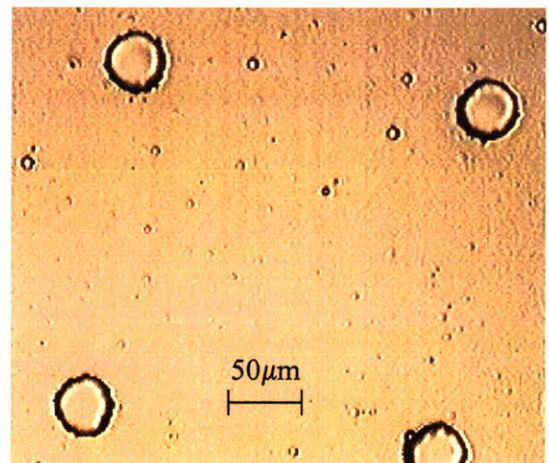


Figure 6.13. B50 μ m 2.5% surface photograph

Only one test was run on each of the surfaces, but the two resulting Stribeck curves are very similar. The B50 μ m2.5% surface shows a curve that rises steeply in the mixed lubrication regime. This sharp friction gradient is unlike data from other tests

using STP as the lubricating fluid, so there could have been an external factor affecting this curve at that particular location.

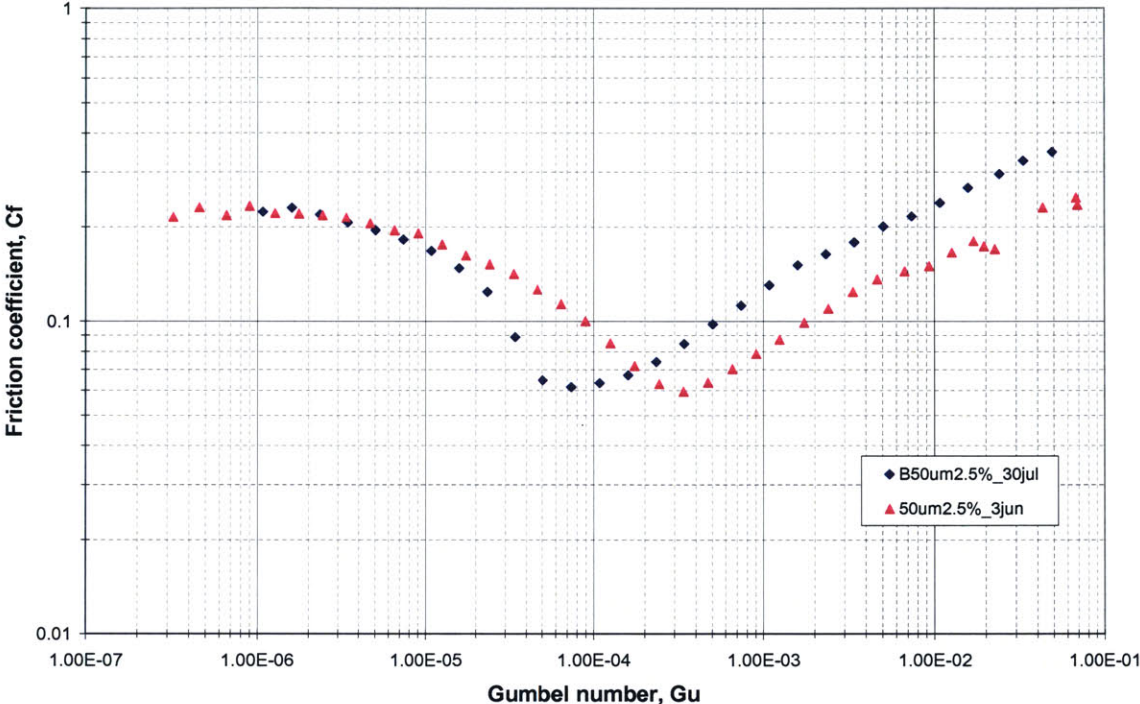


Figure 6.14. Stribeck diagram for the surfaces having a pore diameter of 50μm and 2.5% feature density using STP Oil as the lubricating fluid.

6.2.1 D) 50 μ m Diameter Pores at 5% Area Density

Photographs of the two nickel surfaces containing a pattern of 50 μ m diameter holes at 5% feature density are shown in Figure 6.15 and Figure 6.16. The first surface fabricated (50 μ m5%) was not rotated during plating, so the holes collected air bubbles and are not properly formed. Instead of having a consistent 50 μ m hole size, 25% of the holes have an average size of 108 μ m, and 75% of the holes have the appropriate 50 μ m diameter. Along with misshapen pores, there are several pockets on the surface that are a result of air bubble during the plating process. These small pockets, however, should be insignificant due to their very small size compared to the surface texture. The rough texture around the B50 μ m5% holes is probably a result of internal stresses in the nickel due to the electroless plating process. The roughness, however, is less than 0.5 μ m deep, so it is insignificant compared to the feature depth. The color around the B50 μ m5% holes is STP oil, indicating that this photograph was taken after testing the surface.

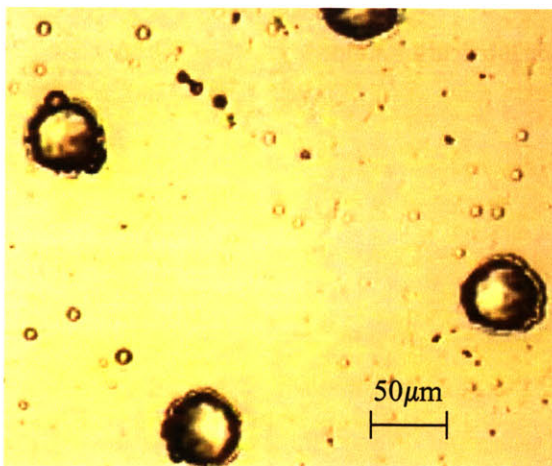


Figure 6.15. 50 μ m 5% surface photograph.

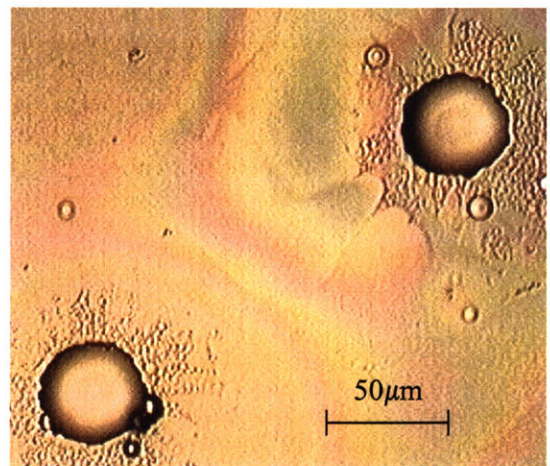


Figure 6.16. B50 μ m 5% surface photograph.

The $50\mu\text{m}5\%$ surface was tested twice, while the $B50\mu\text{m}5\%$ surface was only tested once. The resulting curves are shown in Figure 6.17. Again, there is a particular curve that is not consistent with the rest of the data. If the data from March 10th is neglected, the remaining data is consistent to within 15% of the median value.

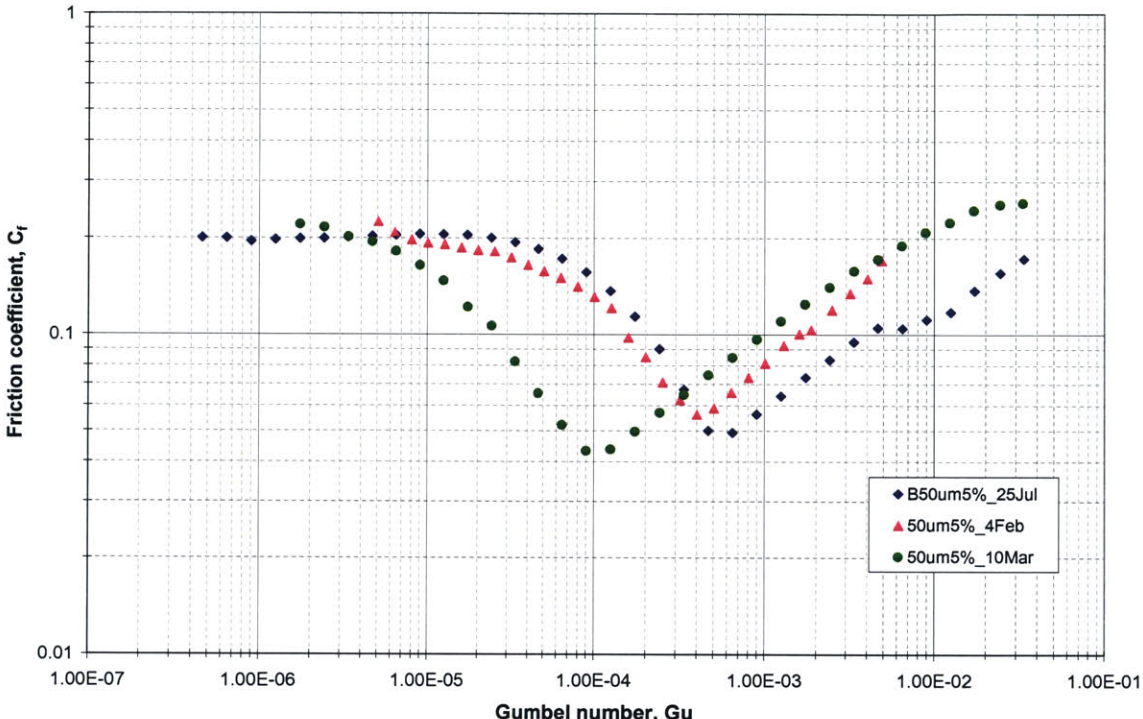


Figure 6.17. Stribeck diagram for the surfaces having a pore diameter of $50\mu\text{m}$ and 5% feature density using STP Oil as the lubricating fluid.

6.2.1 E) 74 μm Diameter Pores at 5% Area Density

Only one 74 μm 5% surface was successfully fabricated, and photograph of that surface is shown in Figure 6.18. The holes are regularly formed, and although the area around them is a little rough, the depth of the roughness is much less than 1 μm .

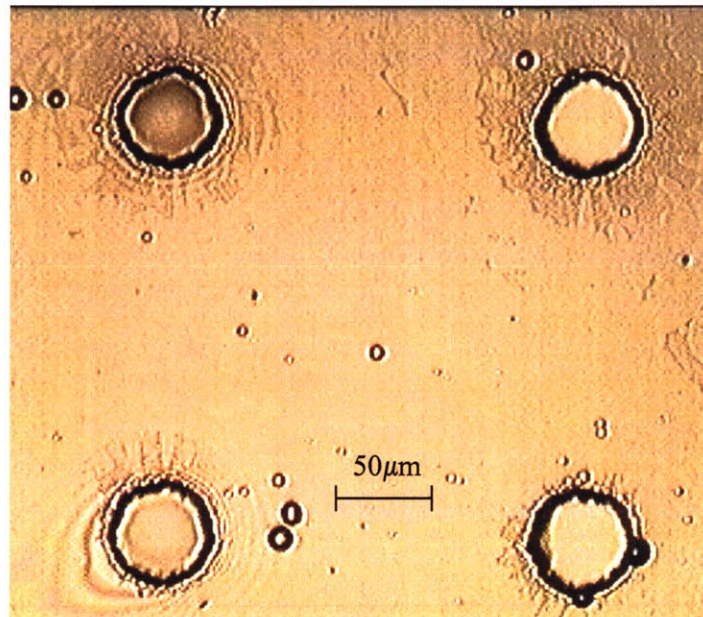


Figure 6.18. 74 μm 5% surface photograph

Figure 6.19 shows the resulting Stribeck curves for the B74 μm 5% surface, which are consistent in the hydrodynamic regime. The resulting curves in the boundary lubrication regime, however, show a very large variation depending on the location on the surface at which they were tested. The curves also indicate minimal variation in friction between the mixed and boundary lubrication regimes. These results are therefore considered unreliable and will not be used for further study in this research.

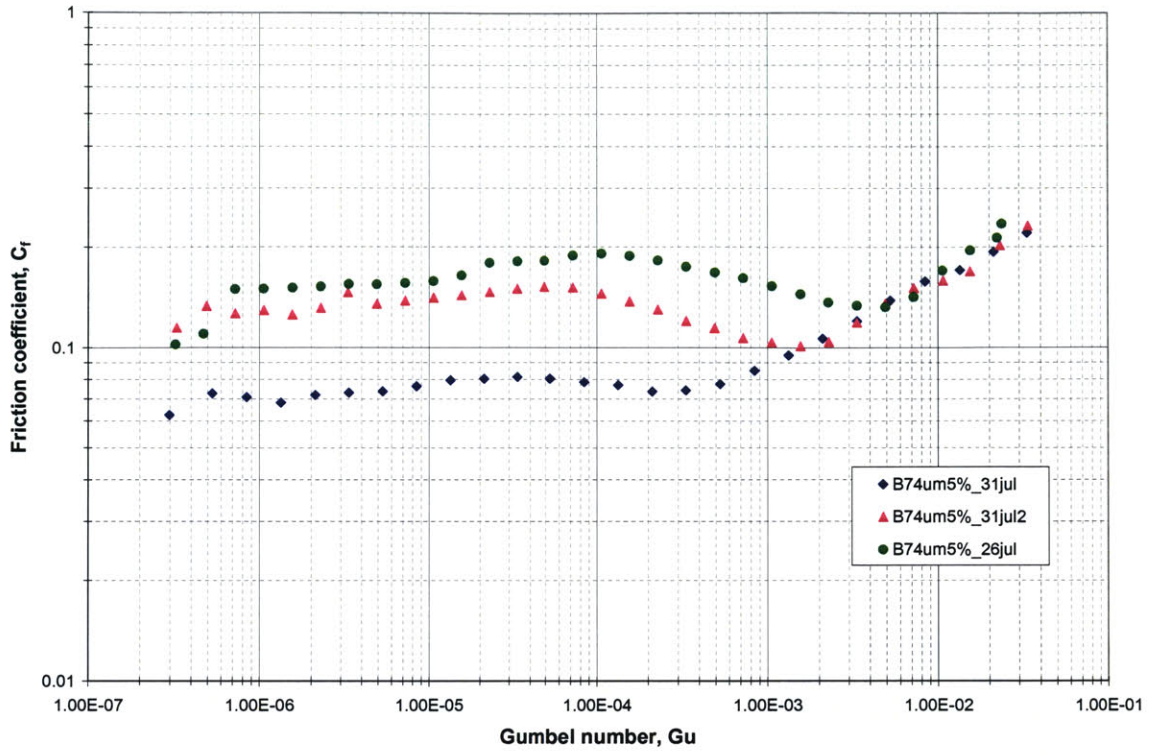


Figure 6.19. Stribeck diagram for the surfaces having a pore diameter of $74\mu\text{m}$ and 5% feature density using STP Oil as the lubricating fluid.

6.2.1 F) 100 μm Diameter Pores at 5% Area Density

Two surfaces were fabricated to test the 100 μm 5% pattern. Both surfaces have regularly shaped patterns, but there are a lot of surface air pockets on the 100 μm 5% surface. The B100 μm 5% surface shows many surface irregularities around the hole, but the surface is otherwise very smooth.

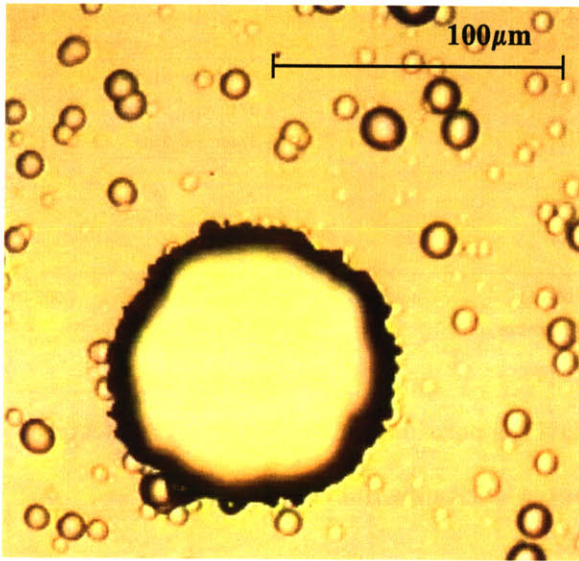


Figure 6.20. 100 μm 5% surface photograph

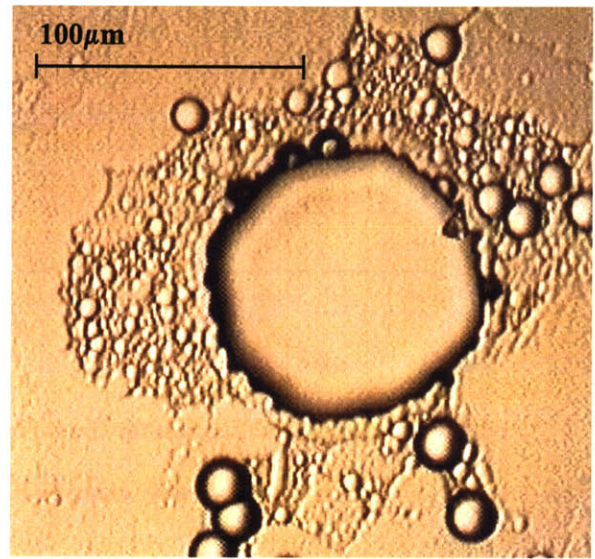


Figure 6.21. B100 μm 5% surface photograph

Only one 100 μm 5% surface was tested with STP oil, but the results in Figure 6.22 show all of the typical characteristics of a Stribeck diagram. The friction coefficient remains constant in the boundary lubrication regime and drops steeply through the mixed regime. Once full-film lubrication is attained, the curve becomes linear until it reaches high shear rates. The digression from a linear rise in the hydrodynamic regime is more than likely a result of the shear-thinning properties of the lubricant.

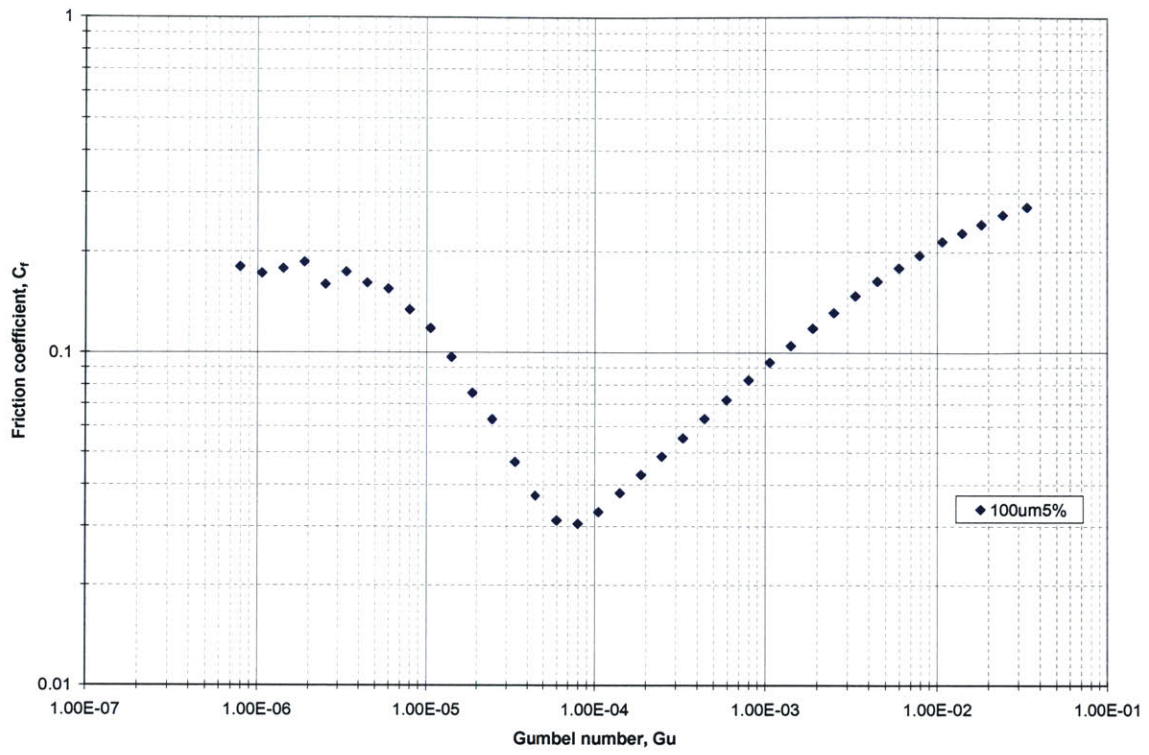


Figure 6.22. Stribeck diagram for the surface having a pore diameter of $100\mu\text{m}$ and 5% feature density using STP Oil as the lubricating fluid.

6.2.1 G) 100 μ m Diameter Pores at 10% Area Density

The original 100 μ m10% surface was not rotated during the nickel plating process and therefore developed air pockets above the holes. These pockets were not as deep as the holes, but they were at a lower level than the surface. Surface photographs, such as the one shown in Figure 6.23, show that almost 50% of the holes have a diameter of approximately 167 μ m rather than 100 μ m. This is a rough approximation, but it is a better representation of the actual surface than the original surface parameters. Given the information from the photographs, the area density of the features is actually 19% rather than 10%. The surface pattern for the B100 μ m10% surface is fabricated as desired (Figure 6.24)

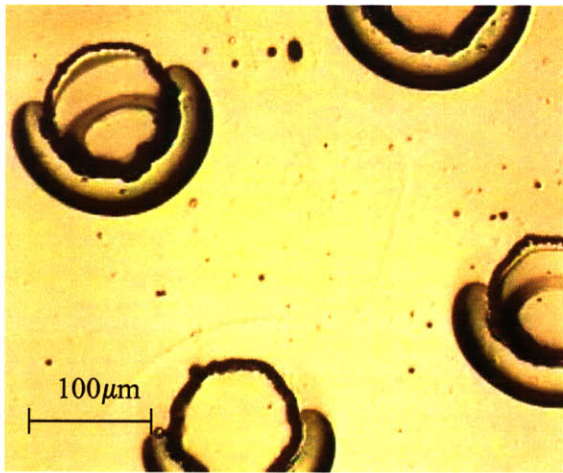


Figure 6.23. 100um10% surface photograph

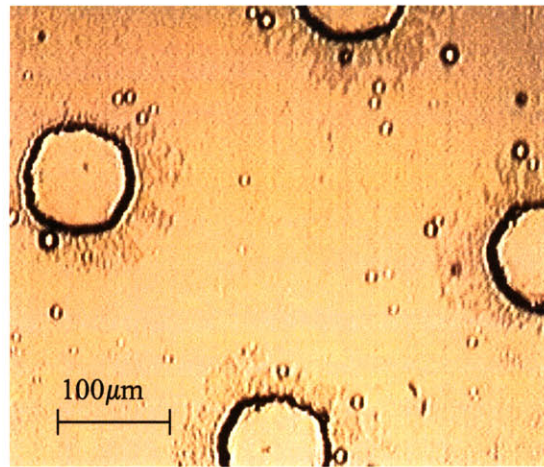


Figure 6.24. B100 μ m10% surface photograph

The Stribeck diagram in Figure 6.25 shows that the Stribeck curves for the 100um10% surface are not at all consistent for tests performed at different times and

locations on the surface. The curve from the 25th of March, however, corresponds nearly perfectly with the curve from the B100um10% surface. Given this correlation, the data from those curves will be used in subsequent analyses.

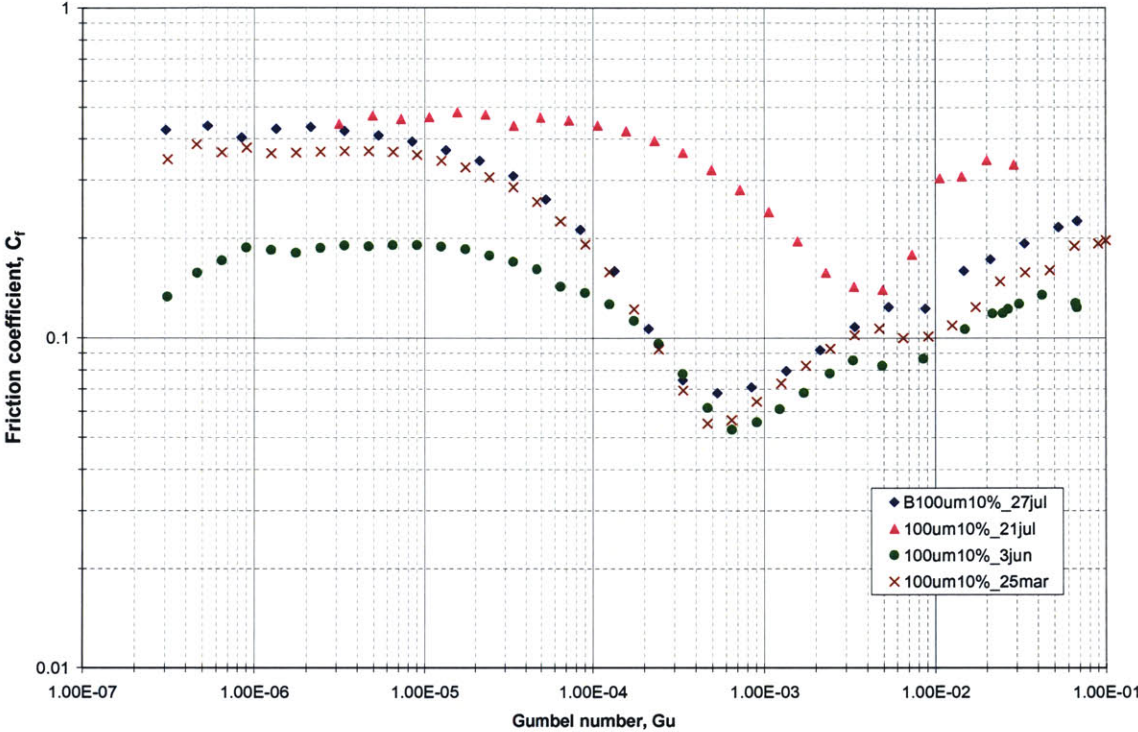


Figure 6.25. Stribeck diagram for the surfaces having a pore diameter of 100μm and 10% feature density using STP Oil as the lubricating fluid.

6.2.1 H) 125 μ m Square Pores at 15% Area Density

The original 125 μ m15% surface was plated using an experimental nickel electroless plating bath. The surface properties of this surface may, therefore, be slightly different than those of the surfaces plated using the commercial plating solution from Plating Processes, Inc. Since the bath was experimental, the exact surface properties are unknown, although it is not likely that they differ greatly from those of the commercial solution. Another difference in the 125 μ m15% surface is that the nickel was polished with 0.1 μ m polishing grit. As seen in Figure 6.26 the polishing left 0.1 μ m deep scratches on the surface that are only noticeable under magnification. The B125 μ m15% surface pores are well-formed, but the surface forms inverted peaks between the pores.

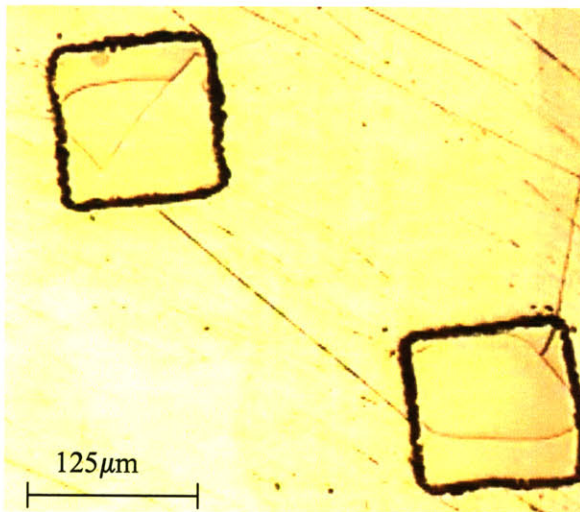


Figure 6.26. 100 μ m15% surface photograph.

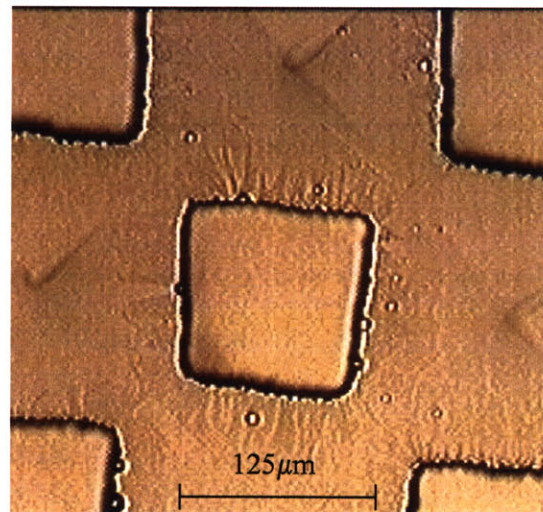


Figure 6.27. B100um15% surface photograph.

Figure 6.28 shows the resulting Stribeck curves for the 100 μm 15% and B100 μm 15% surfaces. The test run on August 1 indicates an error in the testing and should be neglected. The remaining two curves show remarkable consistency between the two different surfaces with the same surface micro texture.

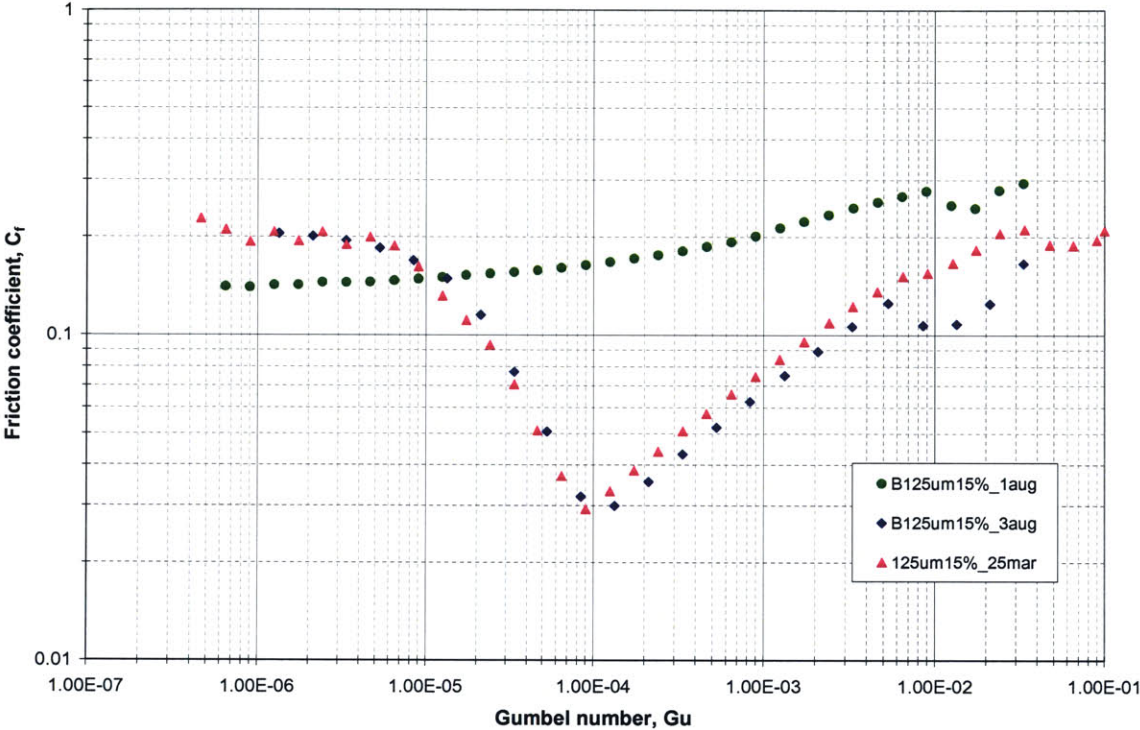


Figure 6.28. Stribeck diagram for the surfaces having squares pores with a side length of 125 μm and 15% feature density using STP Oil as the lubricating fluid.

6.2.1 I) 125 μm Diameter Pores at 20% Area Density

Only one 120 μm 20% surface was fabricated, but surface photographs were not taken. The resulting Stribeck diagram for the surface is given in Figure 6.25.

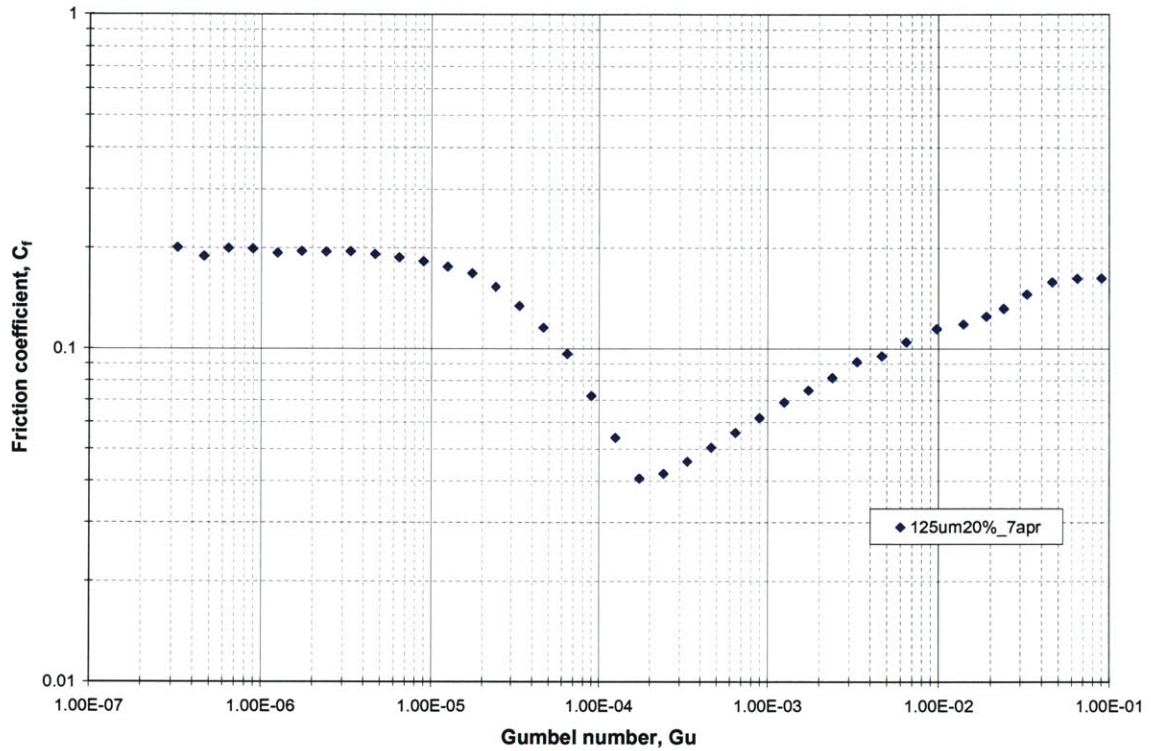


Figure 6.29. Stribeck diagram for the surfaces having a pore diameter of 125 μm and 20% feature density using STP Oil as the lubricating fluid.

6.2.2 Summary of STP Oil Testing

Figure 6.30 shows selected data from each of the surfaces tested with STP Oil. These particular data were chosen either because they were repeated for multiple tests or because they represent a median value for the collection of curves. This data will later be used to analyze the effect of surface texturing on friction testing with a viscoelastic fluid such as STP Oil.

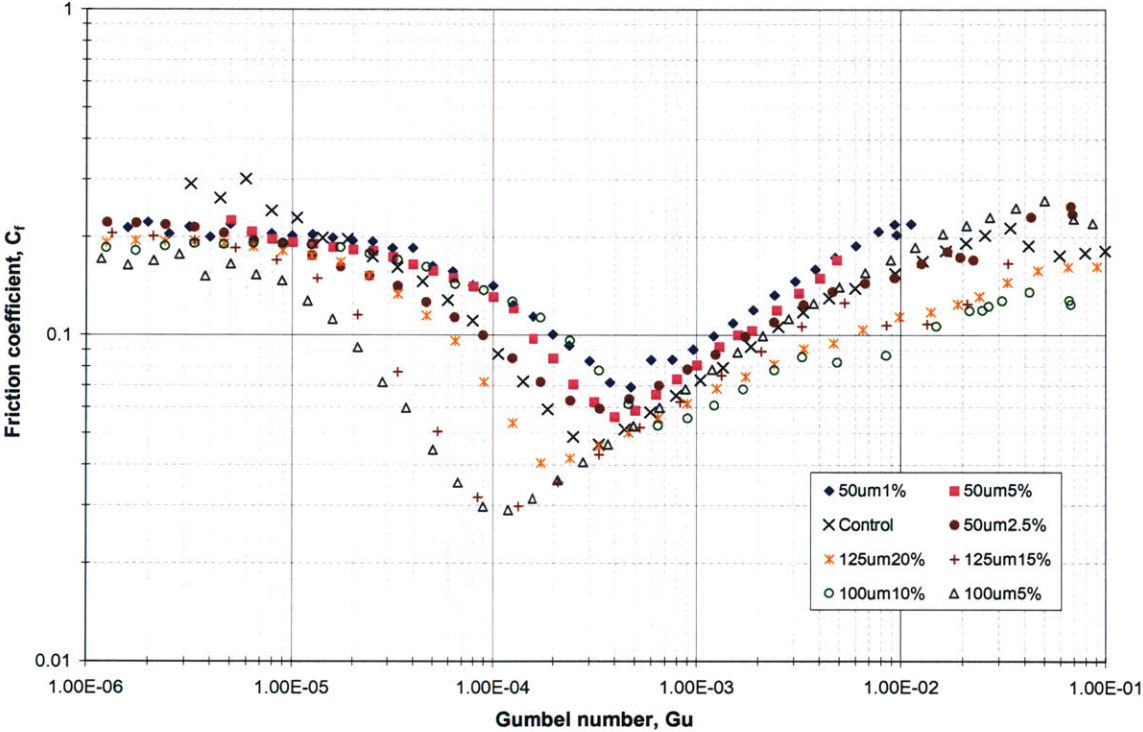


Figure 6.30. Summary of Stribeck curves obtained using STP Oil as the lubricating fluid.

6.3 Results of Lubrication Elasticity

One of the major goals of this research was to determine how the weakly elastic properties of STP Oil Additive interacted with the surface texture. As a comparative lubricant, polydimethylsiloxane (PDMS) of two different viscosities was tested on many of the textured surfaces. These tests were designed to run at the same normal forces and speeds as the tests used with the STP testing. An important consideration when testing the two different lubricants was that they could not be mixed on the surface. Undoubtedly, mixing would give erroneous results, so special care was taken to keep the two lubricants separated.

When comparing the PDMS and STP lubricants, the Gumbel number considers viscosity differences, but it does not take elastic effects into consideration. Figure 6.4 illustrates that the Stribeck diagram successfully accounts for changes in lubricant viscosity, so any difference between the PDMS and STP curve is a result of fluid properties other than viscosity.

The results of the PDMS testing on each surface are shown along with the average result from the STP testing so that the Stribeck curves for each lubricant can be easily compared.

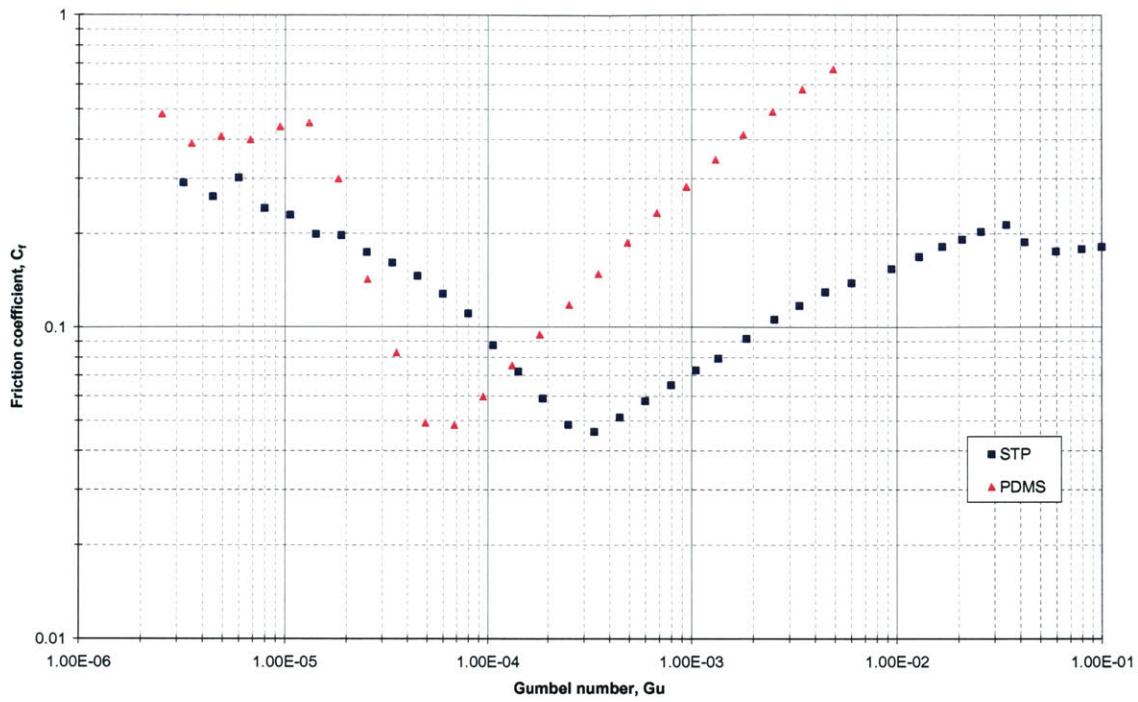


Figure 6.31. Comparison of STP and PDMS30k on the control surface

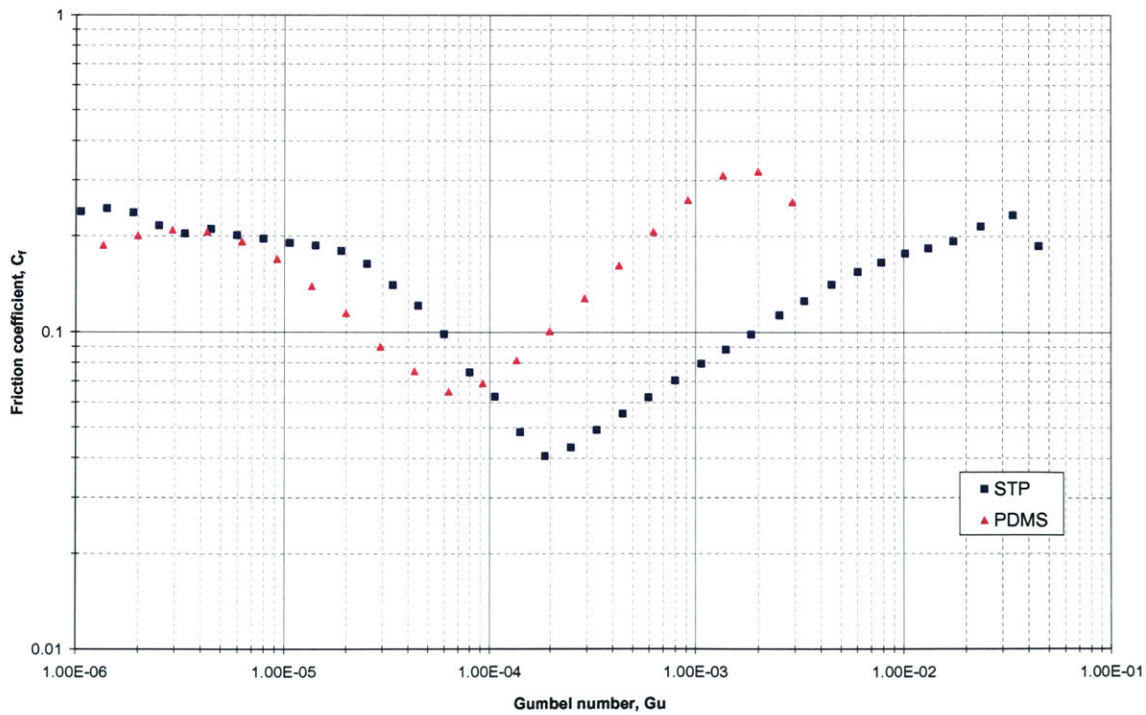


Figure 6.32. Comparison of STP and PDMS on $50\mu m 1\%$ surface.

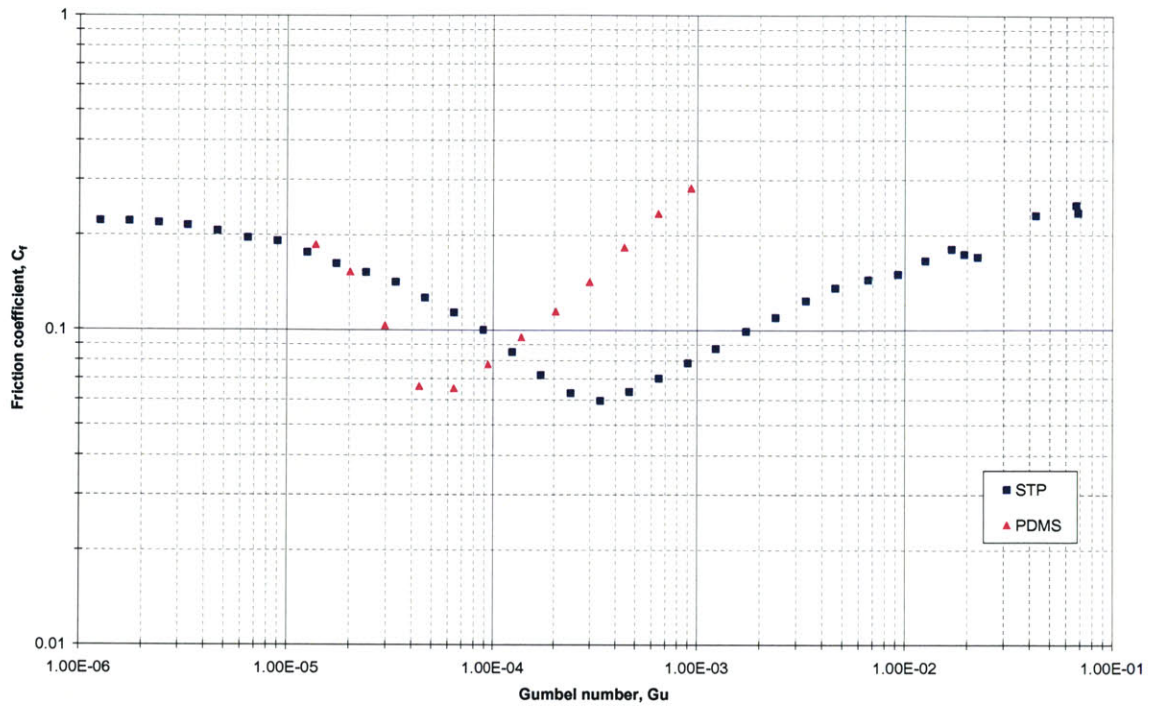


Figure 6.33. Stribeck diagram of STP and PDMS on $50\mu\text{m}2.5\%$ surface.

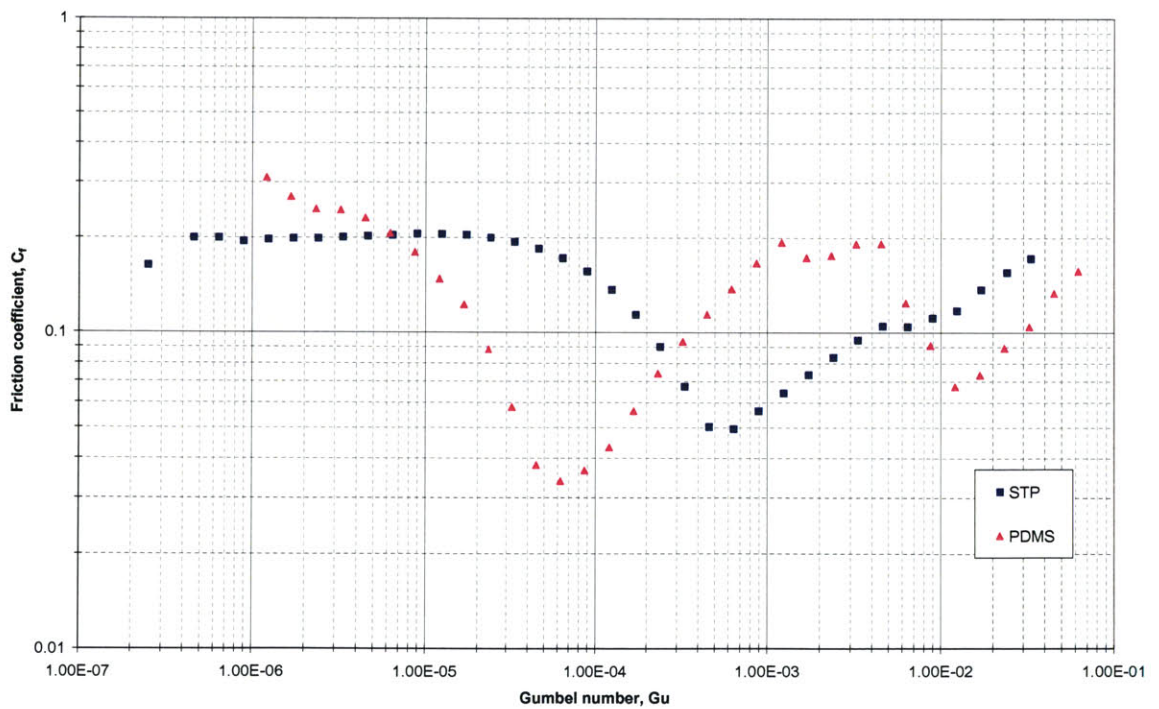


Figure 6.34. Stribeck diagram of STP and PDMS on $50\mu\text{m}5\%$ surface.

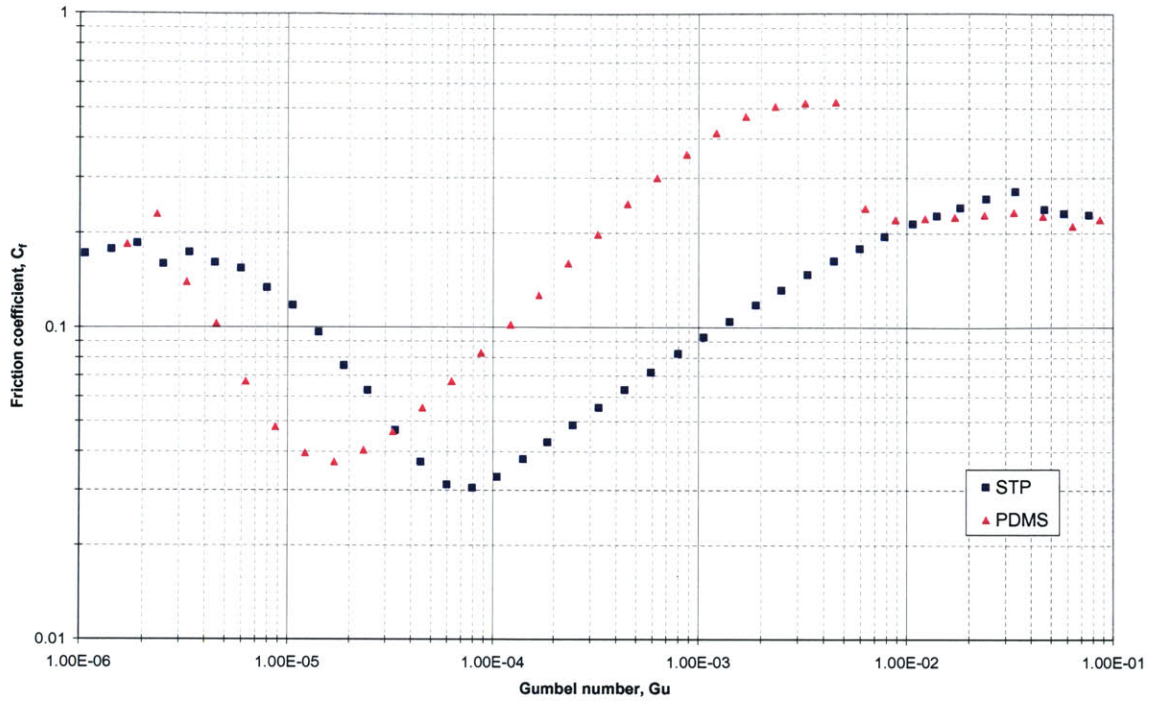


Figure 6.35. Stribeck diagram of STP and PDMS on $100\mu\text{m}5\%$ surface

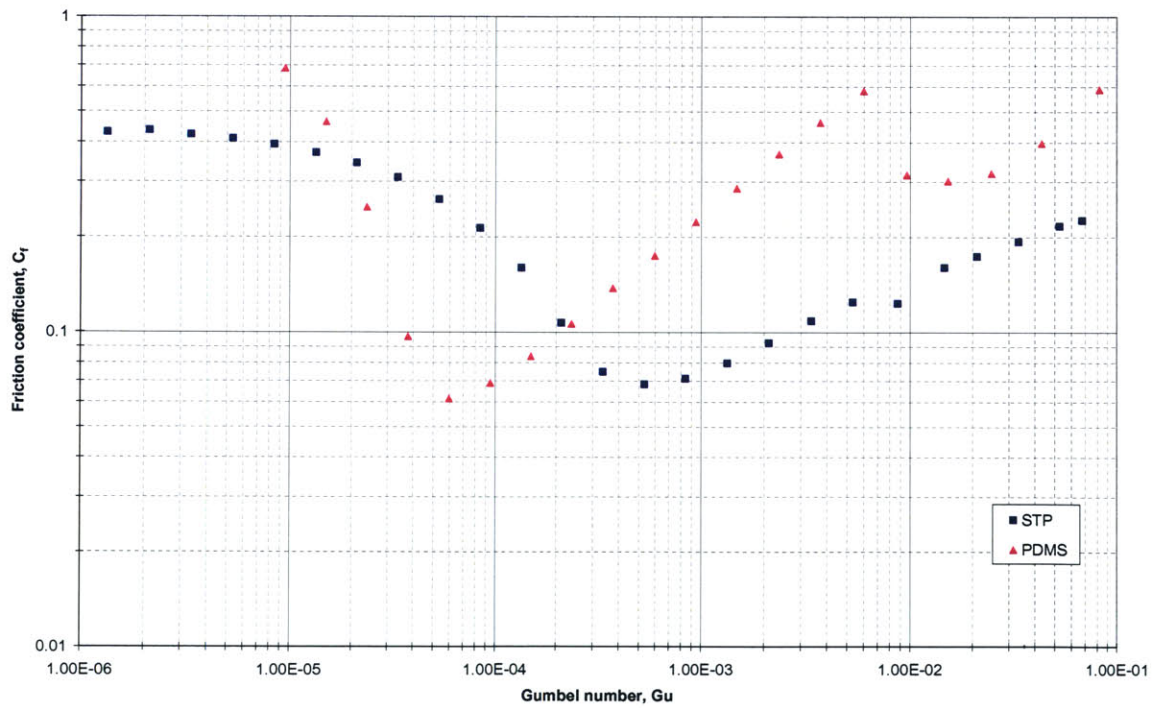


Figure 6.36. Stribeck diagram of STP and PDMS on $100\mu\text{m}10\%$ surfaces.

There is an obvious trend in the curve shifts between the STP and PDMS lubricant that will be discussed later in Chapter 7.

6.4 Summary of Major Results

The results shown in this section demonstrate that nickel micro textured surfaces were successfully fabricated and tested using a torsional rheometer to obtain a Stribeck diagram that covers the entire lubrication spectrum. From this Stribeck diagram, different surface patterns can be compared to determine which features can be used to improve lubrication conditions for particular running conditions. Figure 6.37 shows a comparison of the Stribeck curves for each of the surface patterns tested in this study using STP Oil Additive as the lubricating fluid.

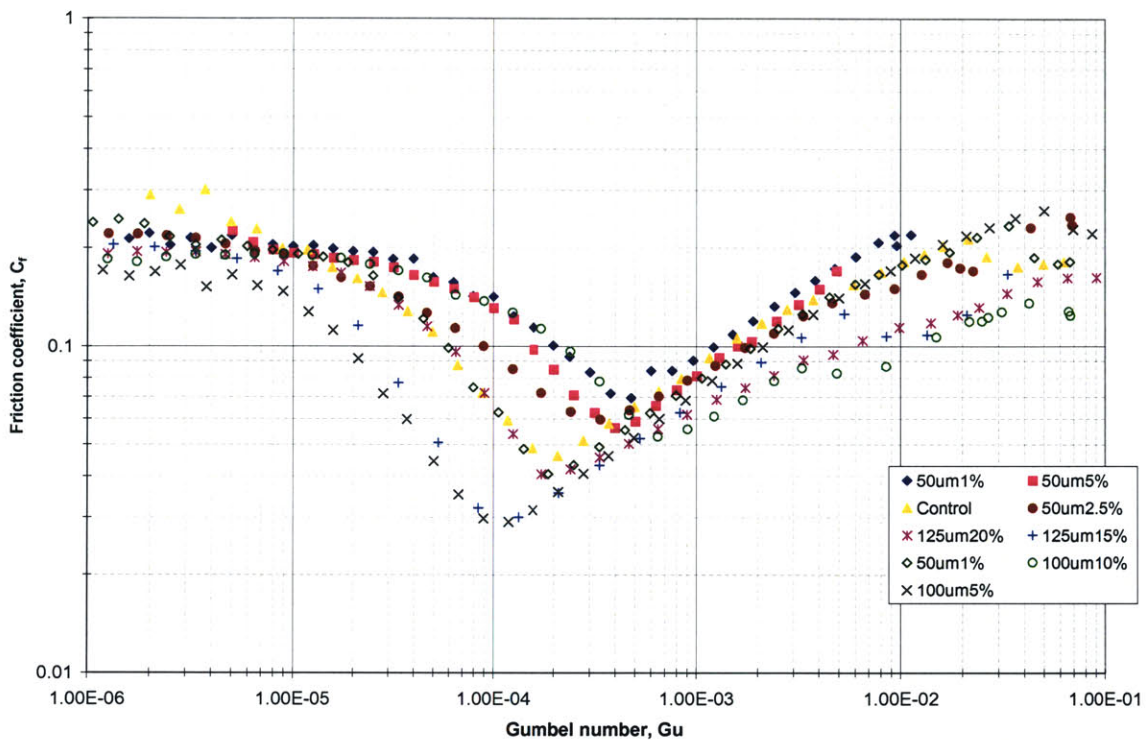


Figure 6.37. Summary of Stribeck curves from textured surfaces using STP Oil Additive as the lubricating fluid.

In addition to surface features, data presented in this research also shows that lubricant properties can greatly affect the friction conditions. Analysis in the subsequent chapter explains how the lubricant rheology might affect the lubrication properties and will predict how to “tune” the lubricant to a particular surface pattern. Figure 6.38 shows a comparison of the textured surfaces using PDMS with a viscosity of 30 Pa·s as the lubricant.

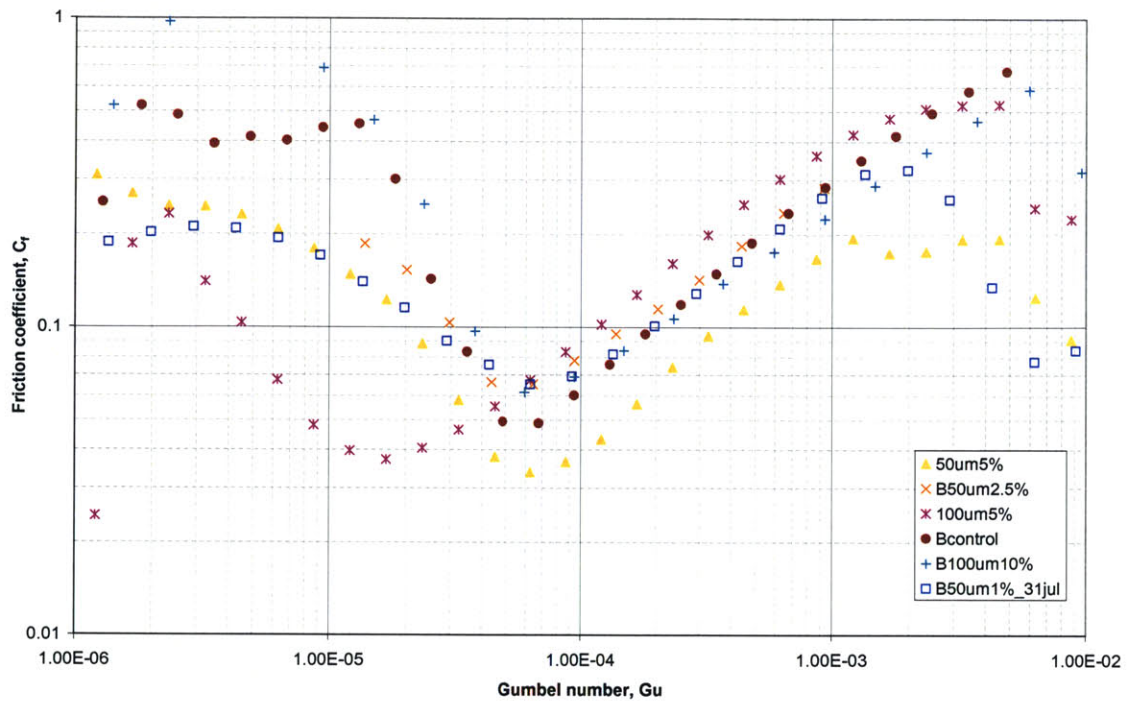


Figure 6.38. Summary of Stribeck curves from textured surfaces using PDMS (30Pa.s) as the lubricating fluid.

Testing performed with PDMS fluid was collected simply as a comparison to the STP fluid, so no emphasis was placed on collecting data that clearly related the relationship of PDMS to the surface texture.

CHAPTER 7

7 DISCUSSION

7.1 Analysis of Experimental Error and Limitations

Several factors are discussed here that could affect the rheometer testing and result in random data errors. First, the nickel surface patterns had minor inconsistencies such as pattern disfigurement that can be seen in the photos that are included in Appendix B. A statistical study of pore uniformity shows that the instantaneous film thickness for a pore ensemble with a variance of pore radii of $\pm 20\%$ can be lowered by 1.5 times the value of identical pores, so a high uniformity is desirable [30] Despite this fact, though, the resulting data from different surfaces with the same surface pattern retained the same major characteristics and always remained within an order of magnitude difference in both Gumbel number and friction coefficient. It can be concluded from this study that the surface patterns are robust and are not sensitive to minor inconsistencies in surface features.

The surfaces were also exposed to ambient conditions, so although nickel is a corrosive-resistant metal, small amounts of corrosion or oxidation could have built up on the surface and affected the frictional properties. Examinations of the surfaces under a microscope were performed, however, and there was no indication of corrosion or oxidation. Along with avoiding corrosion, care was taken to keep the surfaces clean and free from contamination, but neither the surfaces nor the lubricant could be shielded from

airborne dust and particles. There were visible contaminants in the fluid, and although they were avoided, the fluid was still subject to small dust particles.

Another very possible source of error was the 2cm flat plate geometry used as the rheometer head for testing. During initial surface testing, the plate had minor scratches in both the radial and circumferential directions. After several months of testing, however, the plate developed deep grooves in the circumferential direction that could possibly transport fluid across the surface even under boundary lubrication conditions. This transport of fluid to areas of starved lubrication could reduce the friction coefficient and essentially leave no differentiation between the mixed and boundary lubrication regimes. Figure 7.1 of Stribeck diagrams from the $100\mu\text{m}10\%$ surface tested in both the initial stages of research and during later stages show possible evidence of this phenomenon.

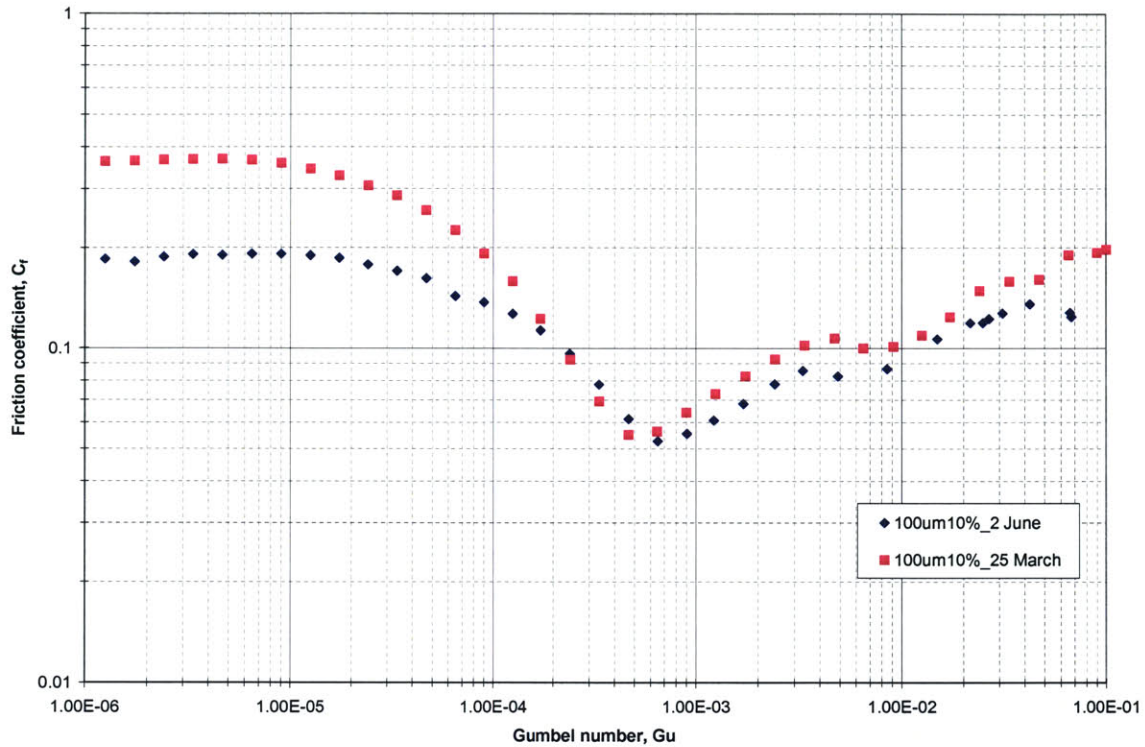


Figure 7.1. Stribeck curves of 100 μ m10% surface indicating wear of the rheometer parallel plate geometry. After several months of testing, the plate developed deep grooves in the circumferential direction that could possibly transport fluid across the surface even under boundary lubrication conditions. The reduction of friction in the mixed and boundary regimes demonstrate the possibility of this phenomenon.

Close examination of the experimental data reflects that there are large sources of error introduced into the testing. If some of the more extreme Stribeck curves are disregarded, though, the remaining curves are typically within $\pm 15\%$ of the median value between the different data sets. This is an acceptable range of experimental error for most aspects of this particular research.

7.2 Run-In Procedure

According to previous research and industry practice [17, 31, 32], many new surfaces require a period of wear called a run-in or break-in period before they reach a steady state value for the friction coefficient. In the rotary shaft seal industry [33], each seal is run through a wear cycle before it is put into commercial use. Without the break in period, a seal performs very poorly and will occasionally experience failure long before seals that have been properly run-in. Theories as to why this break in period occurs include a belief that the surface changes due to work hardening or temperature annealing, while others believe that surface asperities are worn down due to initial breakage and the surfaces conform to each other so that the load is more favorably distributed over the surfaces [3].

Research performed during this study reinforces the existence of a run-in period. The first velocity sweep performed on a surface often resulted in friction patterns that could not be repeated later during the testing process. Each surface was first run-in by sweeping the velocity from nearly 100rad/s to 0.01rad/s before data was taken for surface texture studies so that the running-in effects did not affect the friction data. After this initial velocity sweep, subsequent data was repeatable and showed no evidence of wear.

The break-in period did not always result in surface wear, and data from the initial velocity sweep was sometimes repeatable in subsequent testing. No noticeable pattern was detected, though, to indicate that a particular surface/lubricant condition eliminated the need for the run-in period. More testing would be required to understand the effects of surface texturing on the run-in period.

7.3 Interpreting Stribeck Curve Shifts due to Direction of Velocity Gradient

Throughout this study, it was evident that there is a hysteresis effect in the Stribeck curve for a particular surface/lubricant combination that shifts the curve right or left depending on the direction of the relative velocity sweep. If the velocity increases in speed, the curve shifts to the left, indicating an early onset of the hydrodynamic regime. Typically, increasing the velocity leads to a nearly smooth slope through the hydrodynamic regime, whereas if the velocity is decreasing, there is often a jump in the Stribeck curve during the hydrodynamic regime.

Although no tests were run to verify the assumption, the data indicates that the system is not being given enough time to equilibrate at each particular speed. Since the gap between the two surfaces is changing depending on the velocity and lubrication regime, fluid must flow out from underneath the surface when the velocity is decreasing, and it must flow into the system when the velocity is increasing in order to create a full film of fluid to support hydrodynamic lubrication. If the system is not given enough time to equilibrate, the resulting shear stress data will not accurately represent the particular running condition. The time required for equilibration would depend mostly on the applied normal force, rotational velocity, fluid viscosity, and fluid elasticity.

For this study, data was collected in short time intervals, so it is very possible that the system did not have time to equilibrate at each particular velocity. The resulting shift in the curves is minor, but to retain consistency, the data used to compare surface textures of viscoelastic fluid effects for this study was all collected while sweeping the velocity

from low speeds to high speeds. This method of testing is outlined in Chapter 5 – Experimental Procedures.

Figure 7.2 illustrates both the curve shifts due to velocity and the difference in the Stribeck curve due to the run-in period.

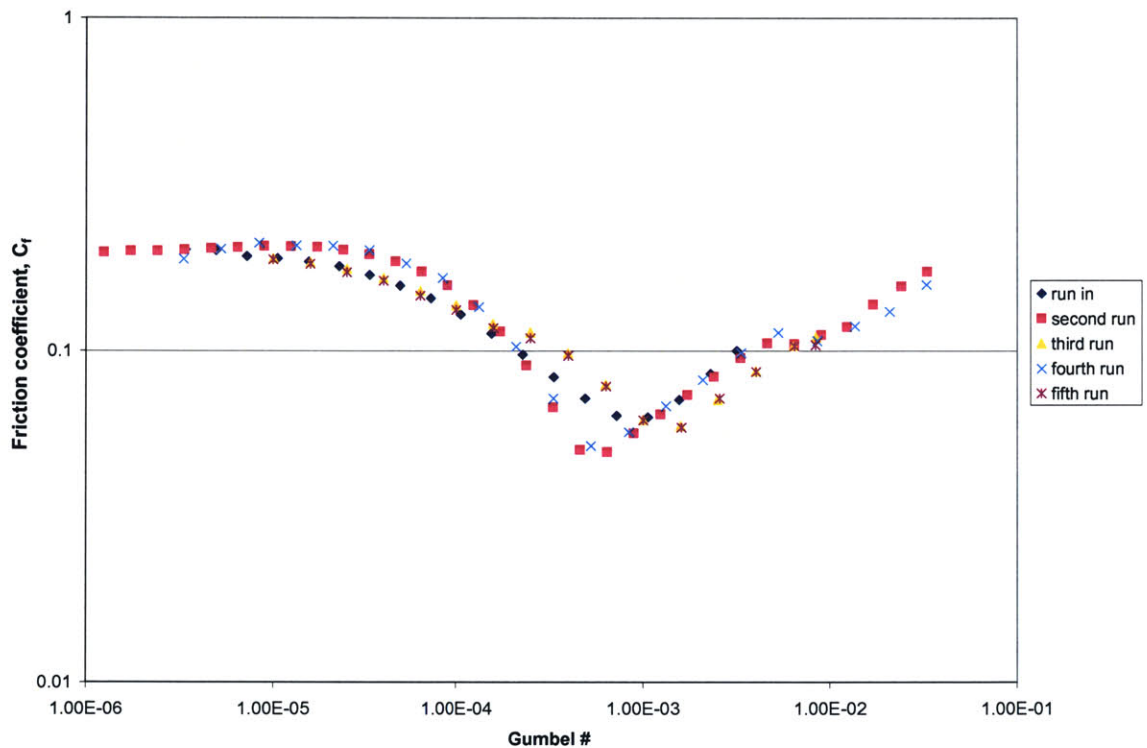


Figure 7.2. Stribeck curve of B50 μ m5% surface showing the run-in curve along with the curve shifts due to the direction of the angular velocity gradients. The second and fourth runs had increasing velocity while the run-in, third run, and fifth run were decreasing in velocity. Throughout this study, the curves were consistently shifted depending on the direction of the relative angular velocity sweep.

7.4 Effect of Texture Pattern on Friction Coefficient

A total of eight patterns were selected for testing in an attempt to determine how to maximize the friction-reducing effect of surface texturing. A summary of the resulting Stribeck curves for each pattern is shown in Figure 7.3. It is important to note that the $125\mu\text{m}15\%$ and the $125\mu\text{m}20\%$ pattern are both square pores, while the rest are circular holes.

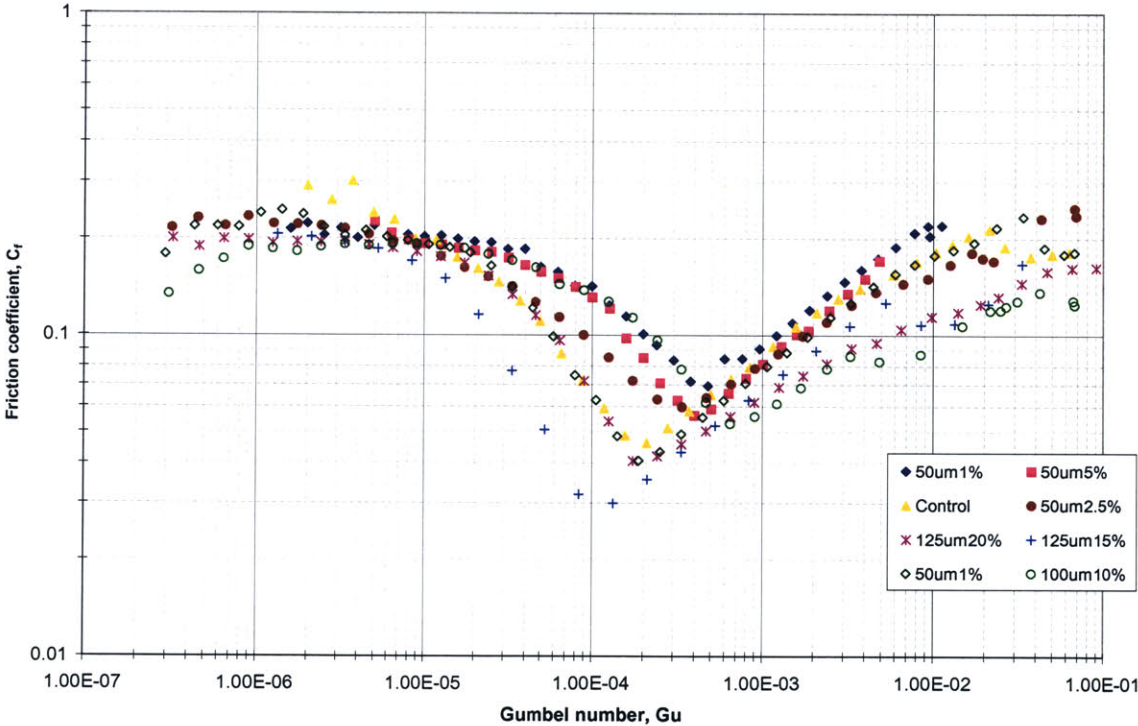


Figure 7.3. Summary of the Stribeck curves for different patterned surfaces. A total of eight patterns were selected for testing in an attempt to determine how to maximize the friction-reducing effect of surface texturing. It is important to note that the $125\mu\text{m}15\%$ and the $125\mu\text{m}20\%$ pattern were both square pores, while the rest were circular holes.

From the acquired data, it is evident that surface micro texturing can reduce friction by as much as 45% in certain areas of the mixed lubrication regime while maintaining beneficial friction reduction in both the hydrodynamic and boundary lubrication regimes. One theory to explain these results is that the pockets of lubricant reduce the load carried by the surfaces. In the hydrodynamic regime, the pores allow a percentage of the area to have a more substantial film thickness, so the shear stresses over the pockets of lubricant are reduced because the distance between the surfaces is increased. This reduction can be calculated by separating the shear stress into a component over the upper surface and a component over the holes. If we assume linear motion for simplicity, the resulting expression for shear stress of a Newtonian fluid is

$$Shear\ stress = \mu \left[(1 - \%) \frac{\partial u}{\partial y} + (\%) \frac{\partial u}{\partial (y + pore\ depth)} \right]$$

where μ is the lubricant bulk viscosity, % is the percent area density of features, y is the gap height between the surfaces, and u is the linear relative velocity between the surfaces. Assuming that the velocity only changes in the y -direction and varies in a linear profile between the surfaces, the equation for shear stress can be simplified for a particular velocity, U , at a particular gap height, H :

$$Shear\ stress = \frac{\mu U}{H} \left[1 - (\%) \frac{pore\ depth}{(H + pore\ depth)} \right].$$

These equations apply for inelastic lubricants in the hydrodynamic regime where there is a continuous lubricant film separating the two surfaces.

When the full-film of lubricant breaks down, there is some surface-to-surface contact, but a portion of the surfaces load is still supported by the hydrostatic lubricant pockets. This reduces the overall load supported by surface-to-surface contact and thus

reduces friction. As the Gumbel number decreases, less of the load is supported by the lubricant until at last boundary lubrication is reached where the lubricant no longer supports any of the load. At this point, Amonton's law can be applied to the surface interaction almost as if it was experiencing dry, sliding friction. This law states that the area of contact between the surfaces is not important, so no matter what surface texturing is applied, the resulting friction will match that of the friction for a smooth, non-textured surface.

Consistent with the theory of load-sharing between the lubricant and surface, the data presented in Figure 7.3 indicates that the surfaces with a higher percentage of surface area taken up by micro pores have a lower coefficient of friction in the hydrodynamic and mixed lubrication regimes than those with a smaller area density of pores. There is some ambiguity in the data, however, that can be explained as a result of experimental data error. This experimental error was previously explained as a result of rheometer wear and non-ideal testing conditions. More work is recommended in this area to determine the effect of pore diameter, depth, and shape. Future research could also lead to determining the amount of contribution the lubrication pockets make in supporting the normal surface load.

7.5 Effect of Viscoelastic Lubricant Properties on Surface Friction

When the Stribeck curve of a viscoelastic fluid is compared to that of a viscous Newtonian fluid for the same surface, there is an obvious shift in the Gumbel numbers of the curves. This shift is evident in Figure 7.4 where STP fluid, a viscoelastic lubricant, and PDMS, a Newtonian fluid, are both tested on a surface with $100\mu\text{m}$ circular pores at

a 5% area density of pores. The viscosity difference of the two fluids has been accounted for in the Gumbel number, but as a viscoelastic fluid, STP has a characteristic relaxation time, λ , while PDMS does not since it is a Newtonian fluid. If the relaxation time effects are neglected in the Gumbel number calculation, the result is a shift in the Stribeck curve.

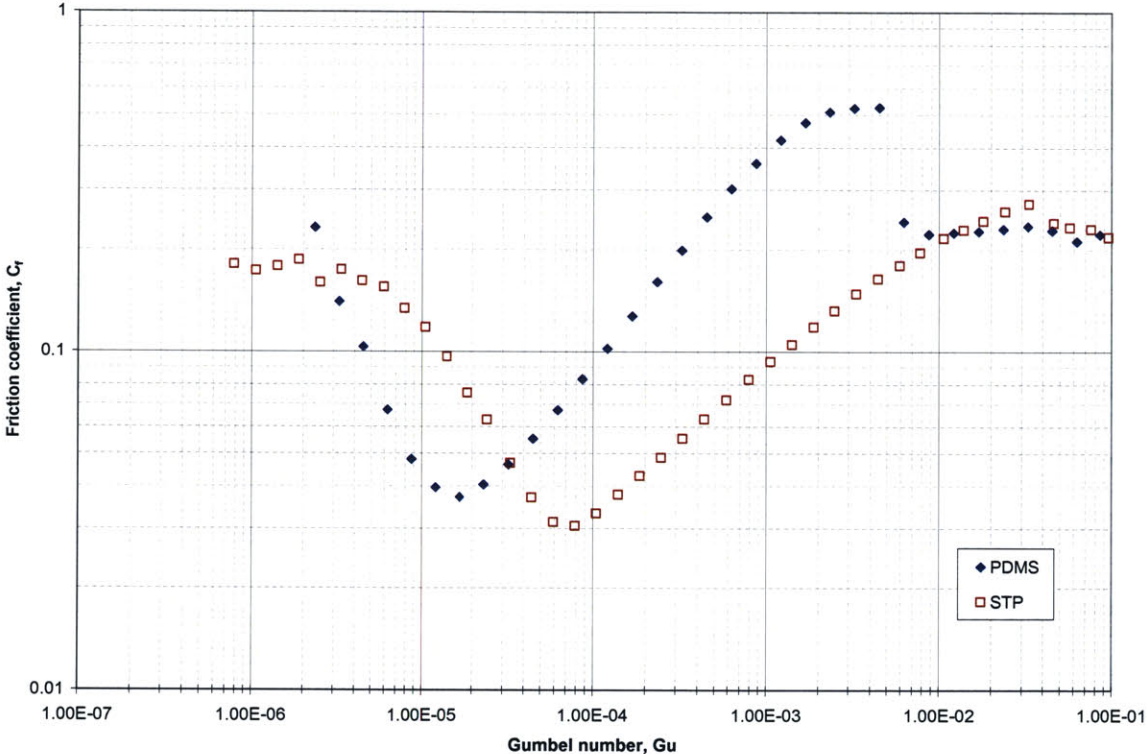


Figure 7.4. Stribeck curve of $100\mu\text{m}5\%$ surface showing the Gumbel number shift as a result of the STP fluid elasticity. While the Gumbel number accounts for variation in the fluid viscosity, it does not allow for non-Newtonian lubricants that also have a characteristic relaxation time. Neglecting the lubricant relaxation time results in a shift of the Stribeck curve.

After noticing the curve shift due to fluid elasticity, further testing on different viscoelastic lubricants shows that the magnitude of the fluid elasticity is proportional to the magnitude of the curve shift. Another observation from the Stribeck diagram showing the two lubricants (Figure 7.4) is that the curve shift is approximately constant

over the boundary and mixed lubrication regimes. In these regimes, the fluid viscosity can be approximated as remaining constant compared to the variable viscosity as the shear rate increases in the hydrodynamic regime and the fluid experiences shear thinning. This curve shift is further analyzed in an attempt to understand the effect of lubricant rheology on the friction between sliding surfaces.

Typically, the Deborah number is used to compare elastic fluids because it is a ratio of the fluid time constant to the characteristic time of the system, as defined by

$$De = \frac{\lambda_s}{t_{system}} = \frac{\lambda_s U}{L}.$$

Because the curve shift between the elastic and inelastic lubricants is approximately constant over a wide range of angular velocities, it can be assumed that the magnitude of the shift is independent of the angular velocity. In order to determine a parameter that will help predict the effect of elasticity, the velocity dependence of the Deborah number needed to be eliminated. It is therefore divided by the Reynolds number calculated using the zero-shear rate viscosity of the elastic lubricant to obtain an elastic sliding friction shift factor that is only a function of the viscoelastic fluid properties

$$\frac{De}{Re} = \frac{\lambda \Omega R}{D} \bigg/ \frac{\rho \Omega R D}{\eta_0} = \frac{\lambda \eta_0}{\rho D^2}.$$

This number is known as the elasticity factor, E , and was previously discussed in viscoelastic flow theory by James and Acosta [34]. In their discussion, James and Acosta interpret the elasticity factor as the ratio of elastic forces to inertial forces

$$E = \frac{\lambda \eta_0}{\rho D^2} = \frac{\text{elastic forces}}{\text{inertial forces}}.$$

In order to account for the relaxation time in friction testing, the Gumbel number of an elastic fluid can be re-scaled by dividing the Gumbel number of the elastic fluid by twice the elasticity factor:

$$Gu_{elastic} = \frac{Gu}{2E} = \frac{\frac{\eta\Omega}{N}}{\frac{2\lambda\eta}{\rho D^2}} = \frac{\rho D^2 \Omega}{2\lambda N}.$$

The new elastic Gumbel number, Gu_{el} , can be compared directly to the Gumbel numbers of Newtonian fluids to better understand the fundamental nature of the surface rather than just the lubricant.

Figure 7.5 shows the elastic and Newtonian Gumbel numbers of two elastic fluids, STP Oil Additive and Valucraft Oil Treatment, compared to the Gumbel number of a Newtonian fluid, PDMS. The elastic Gumbel numbers successfully shift the Stribeck curves of the two elastic fluids so that they can be directly compared to that of the Newtonian fluid. The Valucraft oil is very weakly elastic, so the shift and correction factor are not obvious. The two curves for STP, however, make a clear argument that the elastic Gumbel number can accurately account for the elastic properties of the fluid when testing for the frictional properties.

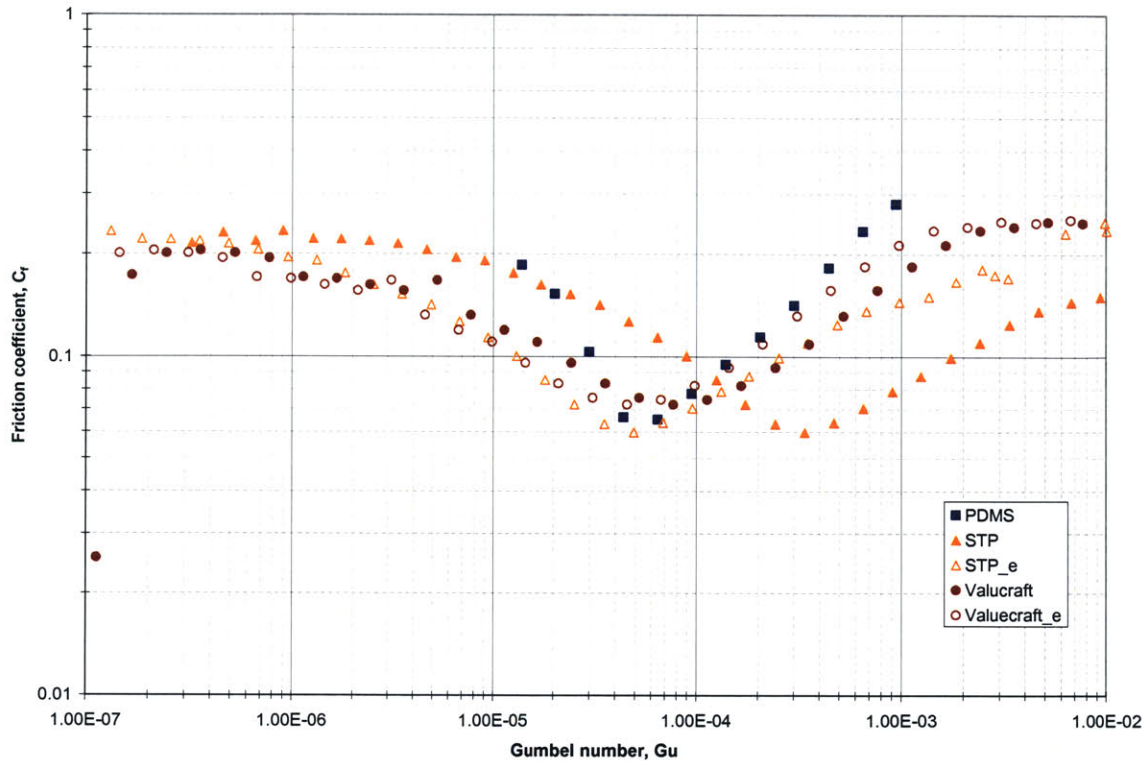


Figure 7.5. Comparison of G_u and $G_{u_{el}}$. The Newtonian Stribeck curves are represented on the graph as solid symbols, and the shifted Stribeck curves using the elastic Gumbel numbers are represented as open symbols, and the names are noted by STP_e and Valucraft_e. The elastic Gumbel numbers successfully shift the Stribeck curves of the two elastic fluids, STP and Valucraft, so that they can be directly compared to that of the Newtonian fluid.

CHAPTER 8

8 CONCLUSIONS AND RECOMMENDATIONS

8.1 Conclusions

The fabrication and testing of micro textured nickel surfaces have been investigated in order to determine the interaction between the textured surface and lubricant rheological properties. Testing parameters such as the lubricant viscosity and normal load were examined to determine the robustness of the Gumbel number, and surface textures ranging from $50\mu\text{m}$ to $125\mu\text{m}$ in diameter and 1% to 20% in area density of features were explored to find the effect of texturing on the friction coefficient. Lubricant elasticity was also investigated in an attempt to understand the importance of fluid rheology and to tune the fluid with particular running conditions. The results from friction testing gave clear Stribeck diagrams and indicated that both surface texture and lubricant rheology play a significant role in the frictional characteristics of a particular lubricant/surface pair.

8.1.1 Testing Surfaces Using the Tribo-Rheometer

Micro textured surfaces can be successfully fabricated and characterized by a complete Stribeck diagram that includes all lubrication regimes. This diagram can be calculated using data collected from testing the textured surfaces with a tribo-rheometer,

as suggested by Kavehpour and McKinley [20]. Testing procedures must include a run-in period, and accurate Stribeck curves should indicate the direction of relative velocity acceleration so that hysteresis effects can be considered.

8.1.2 Friction Reduction using Surface Texturing Techniques

Surface micro pores were successfully fabricated in an array of patterns to test the effect of micro pore area density and diameter on the lubricated, sliding friction of the surface. Results indicate that the surface texture can reduce the surface friction coefficient by as much as a 45% in the mixed lubrication regime for a pattern with $125\mu\text{m}$ square pores at 15% area density. Despite this reduction, all patterns resulted in approximately the same friction coefficient for the boundary lubrication regime. There is evidence in the data indicating that surface texturing can delay the onset of boundary lubrication to smaller values of the Gumbel number, which causes a shift in the Stribeck diagram. This shift changes the value of the friction coefficient at a particular Gumbel or Sommerfeld number and may be the reason why previous researchers reported a reduction in friction coefficient in the boundary lubrication regime as a result of surface texturing [16, 18]. Evidence of this can be seen in Figure 8.1, where Wakuda et al. assert that the data shows a reduction in friction as a result of texturing, but an entire Stribeck curve could show that the data is actually shifted as a result of the applied micro texturing. For this exact reason, it is essential that testing techniques such as the one presented in this thesis be utilized so that the entire lubrication spectrum for a particular surface/lubricant pair can be studied.

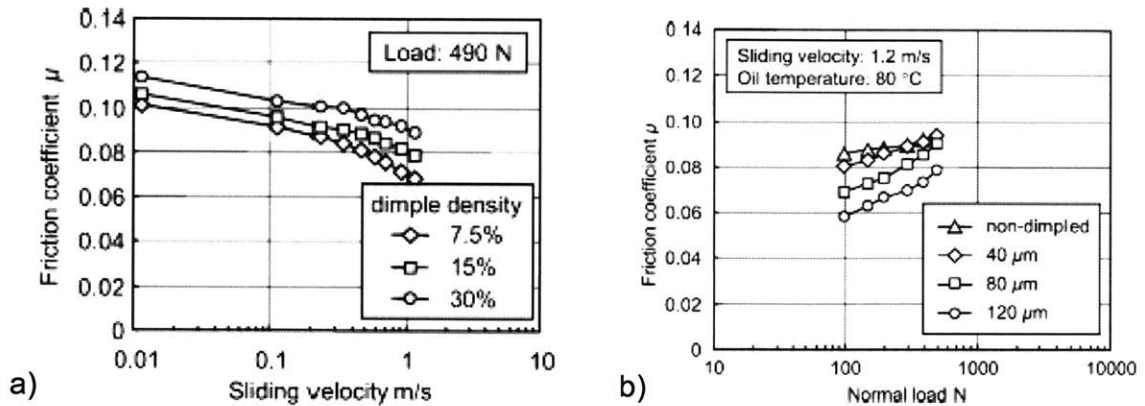


Figure 8.1. Wakuda et al. assert that data from textured ceramic surfaces indicate a reduction in sliding friction when lubricated with engine oil for different texture patterns. Research from the present thesis, however, implies that the apparent friction reduction may actually be a result of a curve shift along the horizontal axis. Figure a) shows the frictional properties for different sliding velocities of ceramic plates textured with 80 μm dimples, and figure b) shows the frictional properties of textured ceramic plates for different normal loads [18].

The results of micro texturing presented for this thesis do not show a clear pattern that would indicate the particular effect of either pore diameter or area density of features on the friction coefficient, but this is likely a result of external sources of error in the friction measurements such as rheometer plate wear and surface pattern irregularities. Polishing the textured surfaces before testing would very likely improve the accuracy of the friction data by reducing the role of surface asperity roughness on the friction coefficient. Another testing improvement would require that the parallel plate geometry used for friction testing be polished before testing so that there are no scratches or imperfections to interact with the texture of the nickel test surface. These improvements should allow for more reliable data and a clearer understanding of the effect of micro texturing on the friction coefficient of a surface.

8.1.3 Impact of Lubricant Elasticity on the Stribeck Diagram

Results from testing lubricants with different rheological properties show that the Gumbel number can successfully account for changes in lubricant viscosity, but it does not account for non-Newtonian lubricants that have a complex viscosity with an elastic component. Analysis of the data and application of viscoelastic flow theory resulted in a new Gumbel number for elastic fluids. This elastic Gumbel number, Gu_{el} , is obtained by dividing the standard Gumbel number, Gu , of an elastic fluid calculated using the zero-shear rate viscosity by an elasticity parameter, E , so that

$$E = \frac{\lambda \eta_0}{\rho D^2}$$

and $Gu_{elastic} = \frac{Gu}{E} = \frac{\rho D^2 \Omega}{\lambda N}$.

Given the new elasticity factor, the effects of lubricant elasticity on the Stribeck curve can be predicted using the rheological properties of the lubricant. The ability to predict the curve shift can be useful when designing systems that experience wear. A single test that determines the Stribeck diagram for a particular system and simple lubricant can be used as a frictional footprint of the system. For particular running conditions, the elasticity of a lubricant can be selected so that the minimum friction coefficient is realized at the desired Gumbel number. If a system runs at multiple loads or velocities, the elasticity can be tuned so that the average friction coefficient is minimized for the desired running conditions.

8.2 Recommendations for Future Work

The work presented in this thesis has clearly shown that the tribo-rheometer can be used to produce a Stribeck diagram that characterizes sliding friction between two surfaces under lubricated conditions. The general trend of friction for different surface texture patterns was discussed, and a shift factor was introduced to normalize the Gumbel number for viscoelastic fluids. Future experiments should concentrate on improving the accuracy of tribo-rheometer measurements by improving both the textured surface condition and the condition of the parallel plate rheometer head used to test the surface.

While the shift in Gumbel number is now understood for different lubricants, future theoretical work is needed to understand both the shift in Gumbel number and friction coefficient as a result of surface texture parameters. In order to apply surface micro texturing research to industrial applications, a study of the texture robustness and wear properties is also required.

Further experiments could also be performed on different surface materials in order to determine the role of the surface material properties on the Stribeck diagram. Several hypotheses have been outlined and are presented in Appendix C which indicate that surface waves could be a large contributor to surface friction. These waves would have unique properties depending on the material properties of the surface. More theoretical work could lead to the understanding of the origin of surface friction and the ability to predict the Stribeck diagram from the knowledge of surface conditions and lubricant properties.

References

1. Nakada, M., *Trends in engine technology and tribology*. Tribology International, 1994. **27**(1): p. 3-8.
2. Kessler, D.A., *A new crack at friction*. Nature, 2001. **413**: p. 260-261.
3. Bhushan, B., ed. *Modern Tribology Handbook*. Vol. 1. 2001, CRC Press: New York.
4. Patir, N. and H.S. Cheng, *An average flow model for determining effects of three-dimensional roughness on partial hydrodynamic lubrication*. ASME J. of Lubrication Technology, 1978. **100**: p. 12-17.
5. Furey, M.J., *Surface temperature in sliding contact*. ASLE Transactions, 1964. **7**: p. 133-146.
6. Meyer, E., et al., *Nanoscience: Friction and Rheology on the Nanometer Scale*. 1998, Singapore: World Scientific.
7. Luengo, G., J. Israelachvili, and S. Granick, *Generalized effects in confined fluids: new friction map for boundary lubrication*. Wear, 1996. **200**: p. 328-335.
8. Lewis, P.R. and C.W. McCutchen, *Mechanism of Animal Joints*. Nature, 1959. **184**: p. 1284 - 1285.
9. Bossler, R.B., *Boundary Layer Lubrication Behavior*. Lubrication Engineering, 1965. **21**: p. 104-111.
10. Anno, J.N., J.A. Walowit, and C.M. Allen, *Microasperity Lubrication*. J. of Lubrication Technology, 1968. **9**: p. 726-731.
11. Hamilton, D.B., J.A. Walowit, and C.M. Allen, *A theory of lubrication by micro-irregularities*. Trans. ASME Journal of Basic Engineering, 1966. **88**: p. 177-85.
12. Cogdell, J.D., et al., *Surface Texture Effects in Thin Film Lubrication of Steel by Silicones*. ASLE Transactions, 1986. **30**(2): p. 141-148.
13. Steinhoff, K., W. Rasp, and O. Pawelski, *Development of deterministic-stochastic surface structures to improve the tribological conditions of sheet forming processes*. J. of Materials Processing Tech., 1996. **60**: p. 355-361.
14. Tian, H., N. Saka, and N. Suh, *Boundary Lubrication Studies on Undulated Titanium Surfaces*. Tribology Transactions, 1989. **32**(3): p. 289-296.
15. Brizmer, V., Y. Kligerman, and I. Etsion, *A Laser Surface Textured Parallel Thrust Bearing*. Tribology Transactions, 2003. **46**(3): p. 397-403.
16. Geiger, M., S. Roth, and W. Becker, *Influence of laser-produced microstructures on the tribological behaviour of ceramics*. Surface and Coatings Technology, 1998. **100-101**: p. 17-22.
17. Wang, X., et al., *The effect of laser texturing of SiC surface on the critical load for the transition of water lubrication mode from hydrodynamic to mixed*. Tribology International, 2001. **34**: p. 703-711.
18. Wakuda, M., et al., *Effect of surface texturing on friction reduction between ceramic and steel materials under lubricated sliding contact*. Wear, 2003. **254**: p. 356-363.

19. Yu, X.Q., S. He, and R.L. Cai, *Frictional characteristics of mechanical seals with a laser-textured seal face*. J. of Materials Processing Tech., 2002. **129**: p. 463-466.
20. Kavehpour, H.P. and G.H. McKinley, *Tribo-rheometry: from gap-dependent rheology to tribology*. Tribology Letters, 2004. **17**(2): p. 327-355.
21. Ronen, A., I. Etsion, and Y. Kligerman, *Friction-reducing surface-texturing in reciprocating automotive components (C)*. Tribology Transactions, 2001. **44**(3): p. 359-366.
22. Pearlstein, F., *Electroless Plating*, in *Modern Electroplating*, F.A. Lowenheim, Editor. 1974, Wiley & Sons: New York. p. 710-747.
23. Blatter, A., et al., *Lubricated sliding performance of laser-patterned sapphire*. Wear, 1999. **232**: p. 226-230.
24. Fletcher, D.I., et al., *Wear behaviour and surface form evolution of a novel titanium carbide implanted surface under lubricated conditions*. Proc. Instn. Mech. Engrs Part J, 2000. **214**: p. 597-610.
25. Stroock, A., *Personal email*. Feb. 2003.
26. Song, I. and P.K. Ajmera, *Use of a photoresist sacrificial layer with SU-8 electroplating mould in MEMS*. J. of Micromechanics and Microengineering, 2003. **13**: p. 816-821.
27. Carreau, P.J., *Rheology of polymeric systems: principles and applications*. 1997, New York: Hanser Publishers.
28. Rodd, L.E., et al., *Capillary Break-up Rheometry of Low-Viscosity Elastic Fluids*. Under Review for Journal of Non-Newtonian Fluid Mechanics, 2004.
29. McKinley, G.H., *Modelling Extensional Viscosity for STP Oil Additive*. 2004: personal communication.
30. Burstein, L. and D. Ingman, *Pore Ensemble Statistics in Application to Lubrication Under Reciprocating Motion*. Tribology Transactions, 2000. **43**(2): p. 205-212.
31. Bulatov, V.P., V.A. Krasny, and Y.G. Schneider, *Basics of machining methods to yield wear- and fretting-resistive surfaces, having regular roughness patterns*. Wear, 1997. **208**: p. 132-137.
32. Ayala, H.M., et al., *Wear of Elastomeric Seals in Abrasive Slurries*. Wear, 1998. **220**: p. 9-24.
33. Davis, K.A., *Investigation of Reverse Pumping in Rotary Seals*, in *Mechanical Engineering*. 2003, Massachusetts Institute of Technology: Cambridge, MA. p. 108.
34. James, D.F. and A.J. Acosta, *The laminar flow of dilute polymer solutions around circular cylinders*. Journal of Fluid Mechanics, 1970. **42**: p. 269-288.

Appendix A: Derivation of the Reynolds Equation

The Reynolds equation is typically used to describe full-film lubrication by combining the equations of motion and continuity. To begin deriving the Reynolds equation, the first step is to consider the Navier-Stokes equation,

$$\rho \left[\frac{\partial \mathbf{v}}{\partial t} + (\mathbf{v} \cdot \nabla) \mathbf{v} \right] = -\Delta p + \mu \Delta^2 \mathbf{v} + \rho \mathbf{f} . \quad (1)$$

The flow of an incompressible, constant viscosity fluid is also governed by the continuity equation,

$$\text{div} \mathbf{v} = 0 . \quad (2)$$

Non-dimensionalization of the Cartesian coordinates with the appropriate length scales and the velocities with the appropriate velocity scales allows the dimensionless continuity equation to be written as:

$$x = L_x \bar{x}, y = L_y \bar{y}, z = L_z \bar{z} ,$$

$$u = U_* \bar{u}, v = V_* \bar{v}, w = U_* \bar{w} ,$$

$$\frac{\partial \bar{u}}{\partial \bar{x}} + \frac{V_* L_{xz}}{U_* L_y} \frac{\partial \bar{v}}{\partial \bar{y}} + \frac{\partial \bar{w}}{\partial \bar{z}} = 0. \quad (3)$$

In order to re-write the momentum equations dimensionless pressure and time variables are defined as:

$$\bar{p} = r_e \frac{p}{\rho U_*^2}, \quad \bar{t} = \Omega t$$

where

$$r_e = \left(\frac{L_y}{L_{xz}} \right) \frac{L_y U_*}{\nu} \quad \text{and} \quad \Omega = \left(\frac{L_y}{L_{xz}} \right) \frac{L_y (L_{xz} \Omega)}{\nu}.$$

The new time and pressure terms can be used to write dimensionless momentum equations

$$r_e \left(\frac{\partial \bar{u}}{\partial \bar{t}} + \bar{u} \frac{\partial \bar{u}}{\partial \bar{x}} + \bar{v} \frac{\partial \bar{u}}{\partial \bar{y}} + \bar{w} \frac{\partial \bar{u}}{\partial \bar{z}} \right) = - \frac{\partial \bar{p}}{\partial \bar{x}} + \frac{\partial^2 \bar{u}}{\partial \bar{y}^2} + \left(\frac{L_y}{L_{xz}} \right)^2 \left(\frac{\partial^2 \bar{u}}{\partial \bar{x}^2} + \frac{\partial^2 \bar{u}}{\partial \bar{z}^2} \right) \quad (4)$$

$$\left(\frac{L_y}{L_{xz}} \right)^2 \left[r_e \left(\frac{\partial \bar{v}}{\partial \bar{t}} + \bar{u} \frac{\partial \bar{v}}{\partial \bar{x}} + \bar{v} \frac{\partial \bar{v}}{\partial \bar{y}} + \bar{w} \frac{\partial \bar{v}}{\partial \bar{z}} \right) - \frac{\partial^2 \bar{v}}{\partial \bar{y}^2} - \left(\frac{L_y}{L_{xz}} \right)^2 \left(\frac{\partial^2 \bar{v}}{\partial \bar{x}^2} + \frac{\partial^2 \bar{v}}{\partial \bar{z}^2} \right) \right] = - \frac{\partial \bar{p}}{\partial \bar{y}} \quad (5)$$

$$r_e \left(\frac{\partial \bar{w}}{\partial t} + \bar{u} \frac{\partial \bar{w}}{\partial x} + \bar{v} \frac{\partial \bar{w}}{\partial y} + \bar{w} \frac{\partial \bar{w}}{\partial z} \right) = - \frac{\partial \bar{p}}{\partial z} + \frac{\partial^2 \bar{w}}{\partial y^2} + \left(\frac{L_y}{L_{xz}} \right)^2 \left(\frac{\partial^2 \bar{w}}{\partial x^2} + \frac{\partial^2 \bar{w}}{\partial z^2} \right). \quad (6)$$

To simplify the momentum equations, the Reynolds lubrication approximation can be made for the length scale ratio (L_y/L_{xz}). Under normal conditions, lubricant films are thin relative to the lateral scale. Films typically range from the millimeter to micron scale, so it can be assumed that $(L_y/L_{xz}) \rightarrow 0$ and $r_e \rightarrow 0$. Using this assumption, Equation 5 is very small in magnitude compared to Equations 4 and 6. So, the momentum and continuity equations can be reduced to

$$\frac{\partial p}{\partial x} = \mu \frac{\partial^2 u}{\partial y^2}, \quad (7)$$

$$\frac{\partial p}{\partial y} = 0, \quad (8)$$

$$\frac{\partial p}{\partial z} = \mu \frac{\partial^2 w}{\partial y^2}, \quad (9)$$

$$\frac{\partial u}{\partial x} + \frac{\partial v}{\partial y} + \frac{\partial w}{\partial z} = 0, \quad (\text{averaged continuity equation}) \quad (10)$$

written now in terms of the dimensional variables.

In order to reach the Reynolds equation for lubrication, the momentum equations are integrated and evaluated assuming boundary conditions on the velocity and assuming that the pressure is constant across the film (y-direction)

$$u = U_1, \quad w = 0 \quad \text{at } y = 0$$

$$u = U_2, \quad w = 0 \quad \text{at } y = h$$

so that

$$u = \frac{1}{2\mu} \frac{\partial p}{\partial x} (y^2 - yh) + \left(1 - \frac{y}{h}\right) U_1 + \frac{y}{h} U_2, \quad (11)$$

$$w = \frac{1}{2\mu} \frac{\partial p}{\partial z} (y^2 - yh). \quad (12)$$

The pressure distributions must be such that the continuity equation is satisfied. To assure this, substitute Equations 11 and 12 into the averaged equation of continuity (Equation 10). The result is the Reynolds equation that governs the pressure distribution in a lubricant film,

$$\frac{\partial}{\partial x} \left(\frac{h^3}{\mu} \frac{\partial p}{\partial x} \right) + \frac{\partial}{\partial z} \left(\frac{h^3}{\mu} \frac{\partial p}{\partial z} \right) = 6(U_1 - U_2) \frac{\partial h}{\partial x} + 6h \frac{\partial(U_1 + U_2)}{\partial x} + 12(V_2 - V_1). \quad (13)$$

Appendix B: Micro Textured Surface Photographs

50 μm Diameter Circular Pores with 1% Feature Density.....	123
50 μm 1%.....	123
B50 μm 1%	123
50 μm Diameter Circular Pores with 2.5% Feature Density.....	124
50 μm 2.5%.....	124
B50 μm 2.5%	124
50 μm Diameter Circular Pores with 5% Feature Density.....	125
50 μm 5%.....	125
B50 μm 5%	125
74 μm Diameter Circular Pores with 5% Feature Density.....	126
B74 μm 5%	126
100 μm Diameter Circular Pores with 5% Feature Density	127
100 μm 5%.....	127
B100 μm 5%	127
100 μm Diameter Circular Pores with 10% Feature Density	128
100 μm 10%.....	128
B100 μm 10%	128
125 μm Square Pores with 15% Feature Density	129
125 μm 15%.....	129
B125 μm 15%	129
Control Surface	130
BControl.....	130

This appendix shows photographs of the surfaces used for this study. The scaling for each photograph will be evident because the feature size will be given for each set.

50 μ m Diameter Circular Pores with 1% Feature Density

50 μ m1%

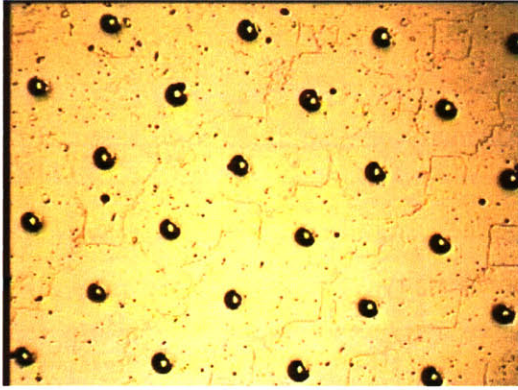


Figure B.1. 50 μ m1% at 5x magnification

B50 μ m1%

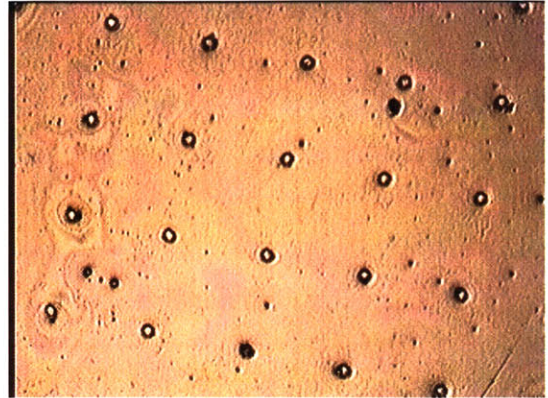


Figure B.4. B50 μ m1% at 5x magnification

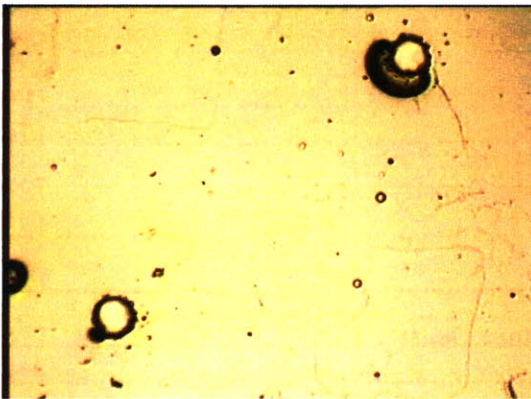


Figure B.2. 50 μ m1% at 20x magnification

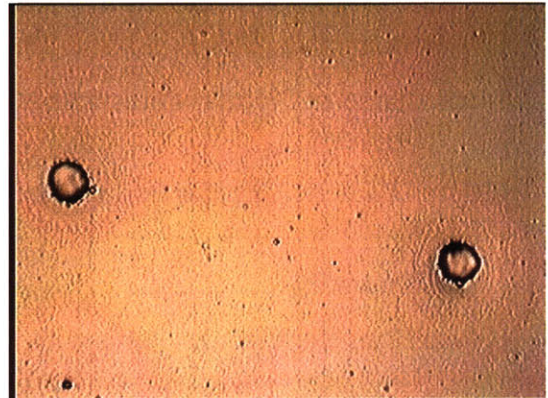


Figure B.5. B50 μ m1% at 20x magnification

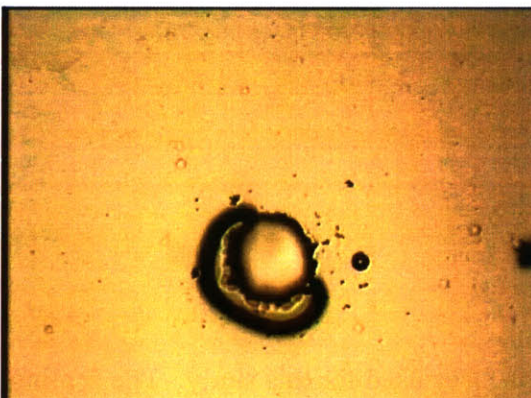


Figure B.3. 50 μ m1% at 40x magnification

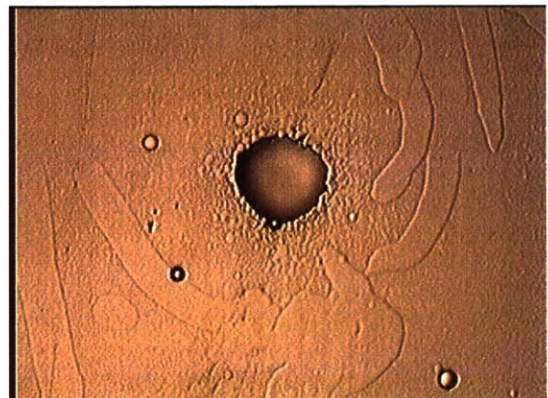


Figure B.6. B50 μ m1% at 40x magnification

50 μ m Diameter Circular Pores with 2.5% Feature Density

50 μ m2.5%

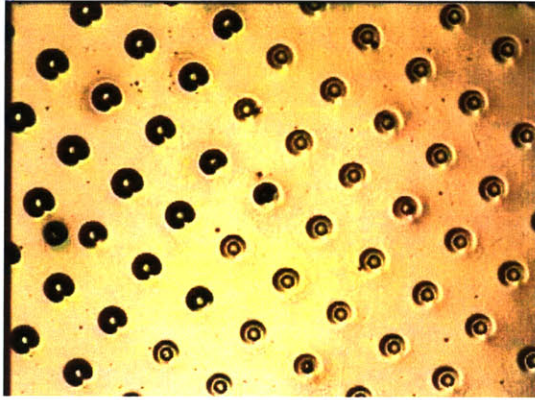


Figure B.7. 50 μ m2.5% at 5x magnification

B50 μ m2.5%

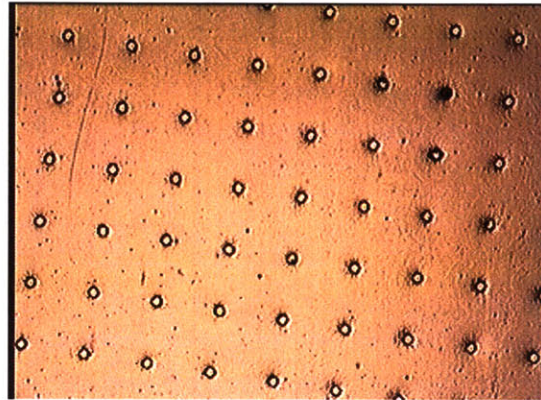


Figure B.10. B50 μ m2.5% at 5x magnification

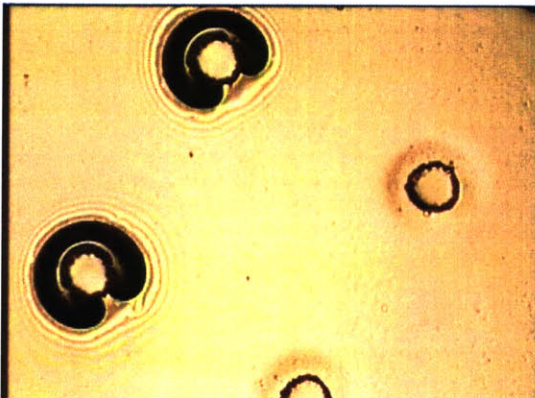


Figure B.8. 50 μ m2.5% at 20x magnification

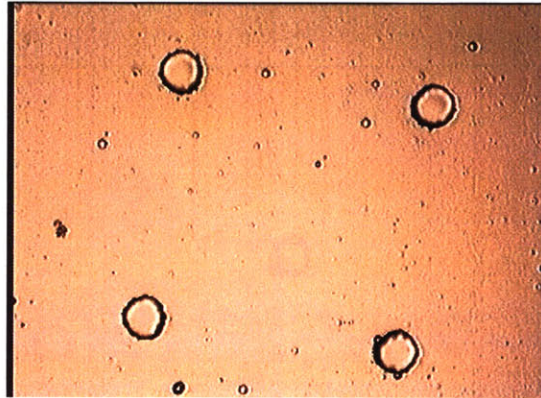


Figure B.11. B50 μ m2.5% at 20x magnification

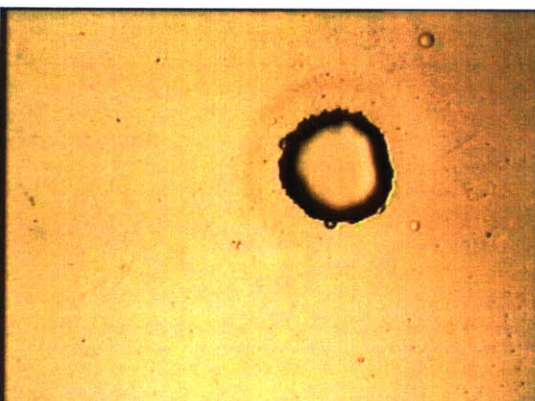


Figure B.9. 50 μ m2.5% at 40x magnification

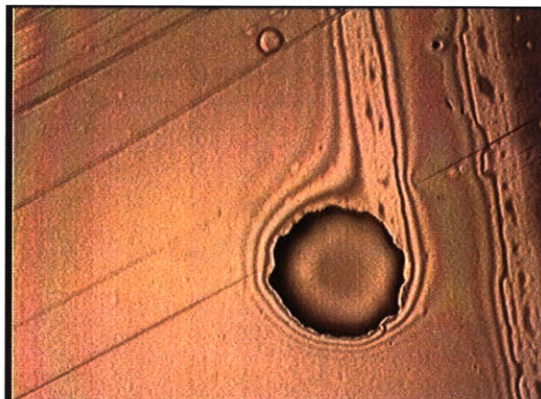


Figure B.12. B50 μ m2.5% at 50x magnification showing wear scars covered in lubricant

50 μ m Diameter Circular Pores with 5% Feature Density

50 μ m5%

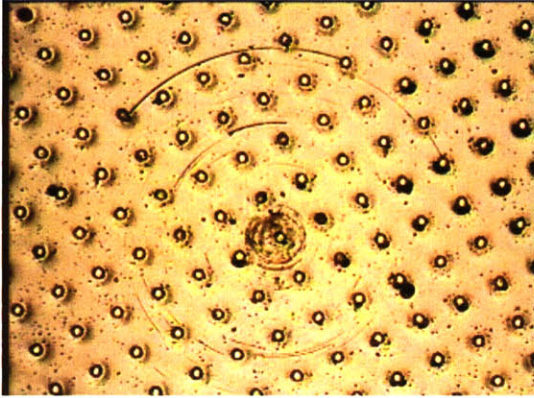


Figure B.13. 50 μ m5% showing the center of rotation for the wear scars.

B50 μ m5%

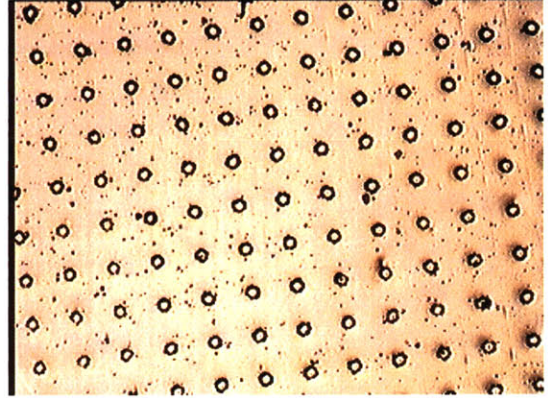


Figure B.16. B50 μ m5%

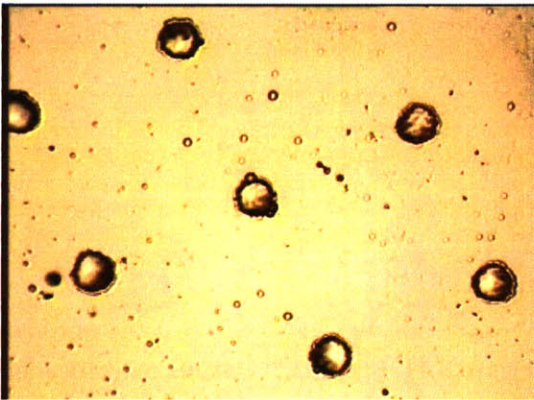


Figure B.14. 50 μ m5%

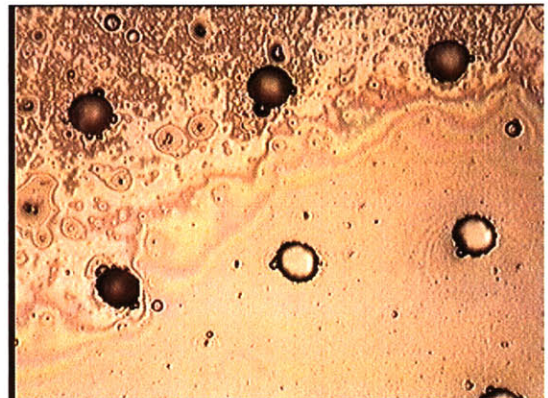


Figure B.17. B50 μ m5% with lubricant covering half

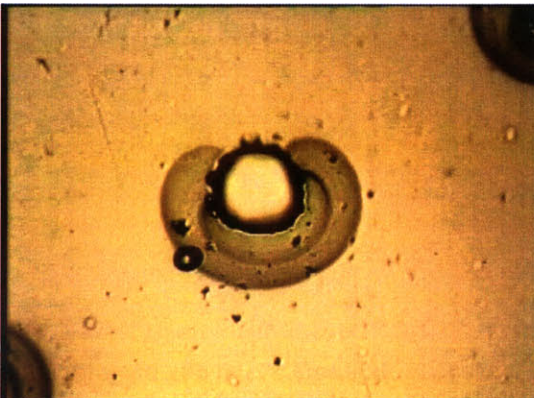


Figure B.15. 50 μ m5% misshapen hole

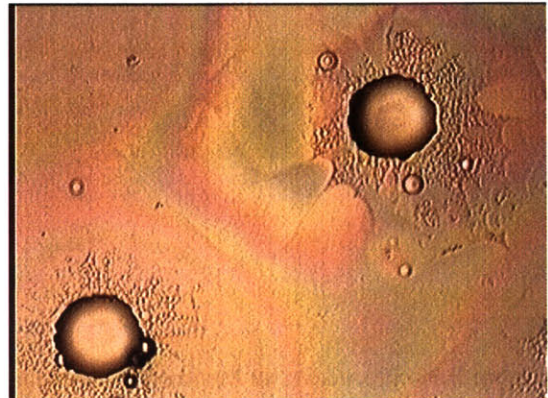


Figure B.18. B50 μ m5% with lubricant

74 μ m Diameter Circular Pores with 5% Feature Density

(Only one 74 μ m5% surface was fabricated, but it was named B74 μ m5%)

B74 μ m5%

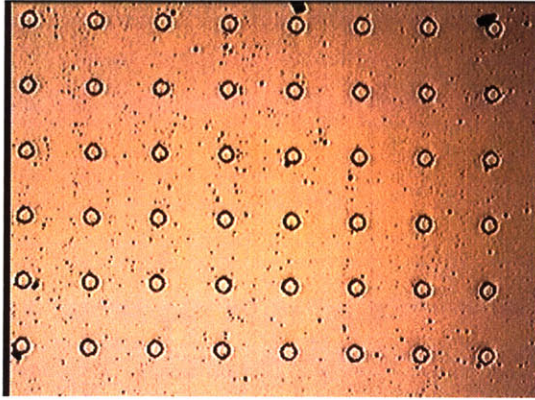


Figure B.19. B74 μ m5%

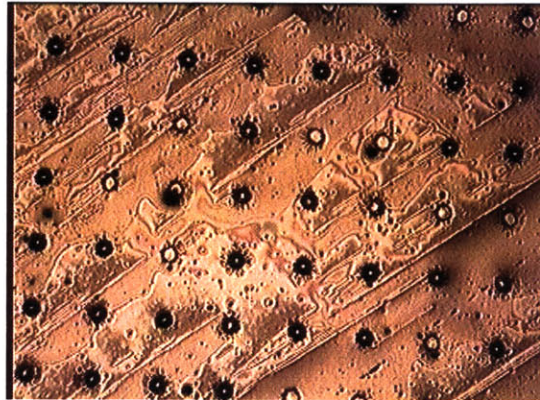


Figure B.22. B74 μ m5% after testing with lubricant

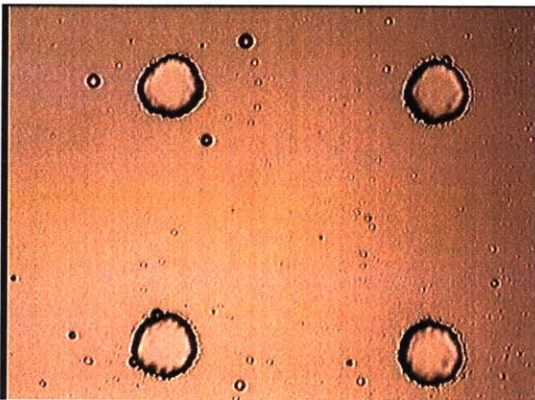


Figure B.20. B74 μ m5%

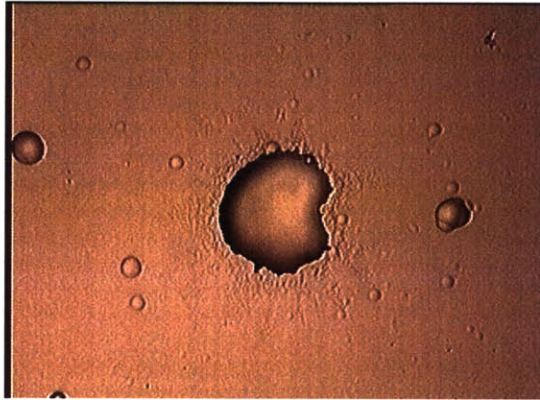


Figure B.23. B74 μ m5% oddly disfigured hole

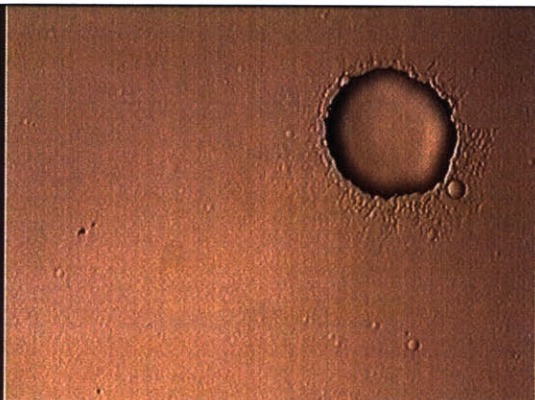


Figure B.21. B74 μ m5% showing surface texture around hole

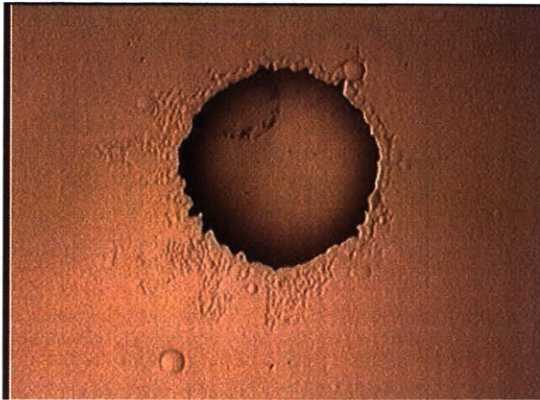


Figure B.24. B74 μ m5%

100 μm Diameter Circular Pores with 5% Feature Density

100 μm 5%

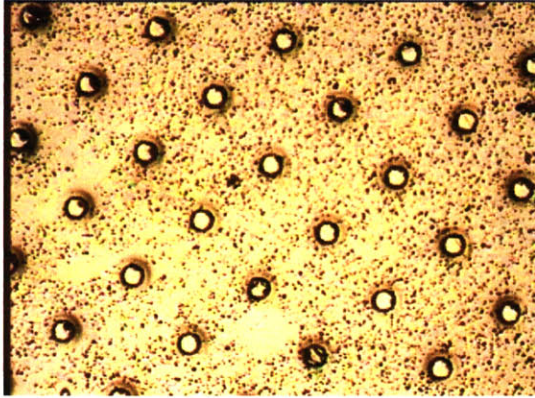


Figure B.25. 100 μm 5%

B100 μm 5%

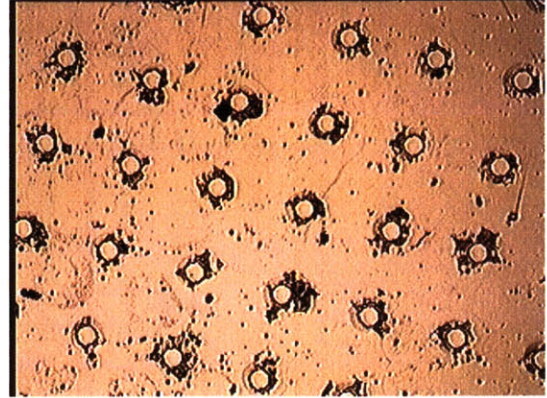


Figure B.28. B100 μm 5% inconsistent surface

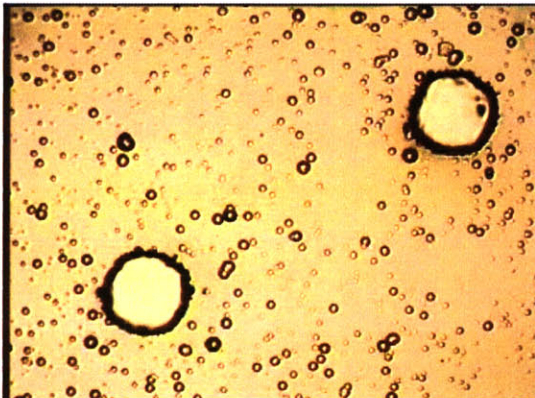


Figure B.26. 100 μm 5%

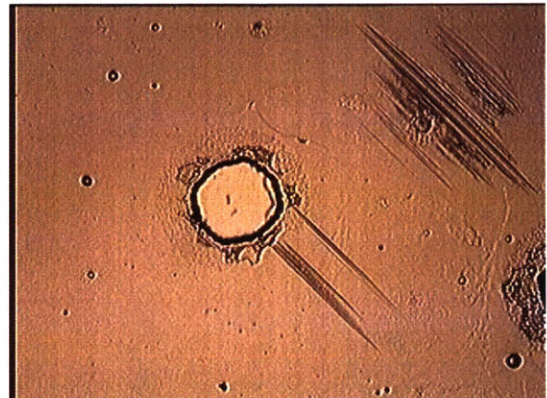


Figure B.29. B100 μm 5% showing wear scars

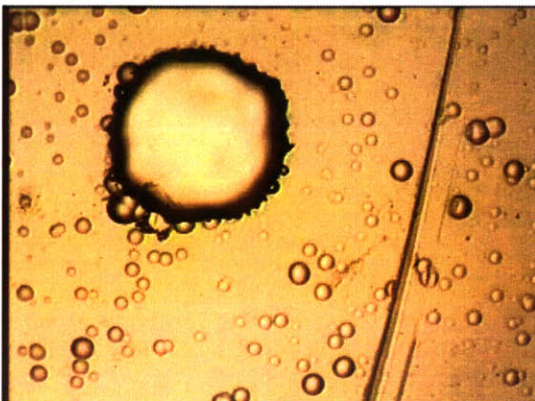


Figure B.27. 100 μm 5% with wear scar

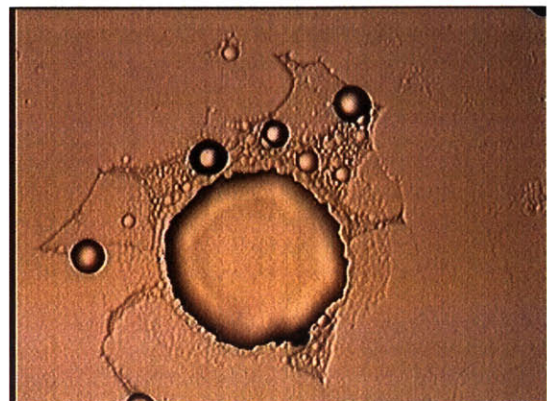


Figure B.30. B100 μm 5%

100 μ m Diameter Circular Pores with 10% Feature Density

100 μ m10%

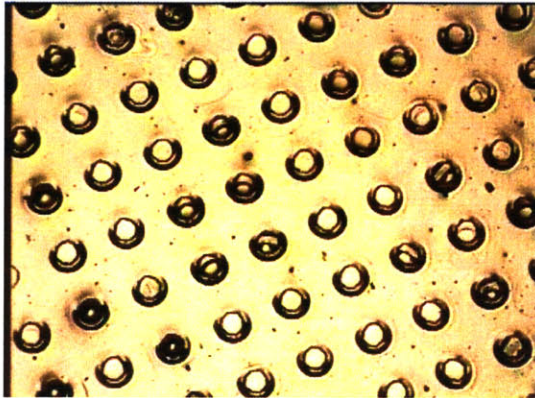


Figure B.31. 100 μ m10% with misshapen holes

B100 μ m10%

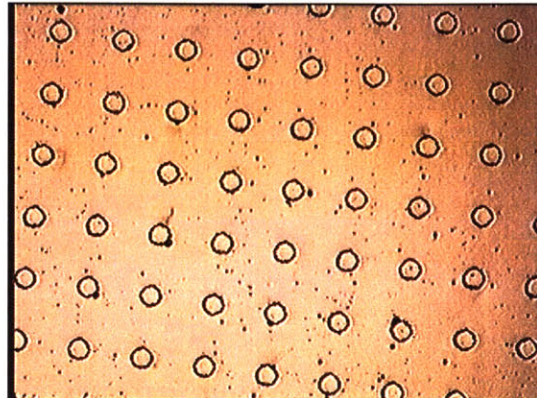


Figure B.34. B100 μ m10%

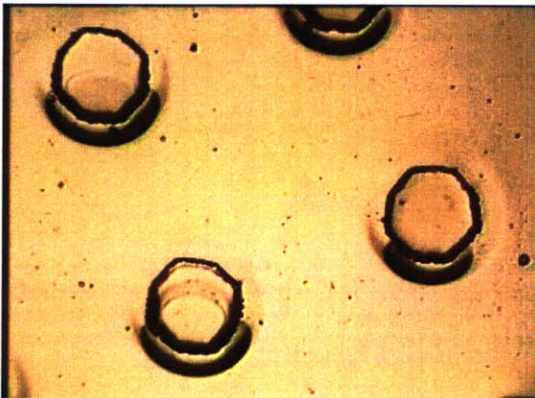


Figure B.32. 100 μ m10%

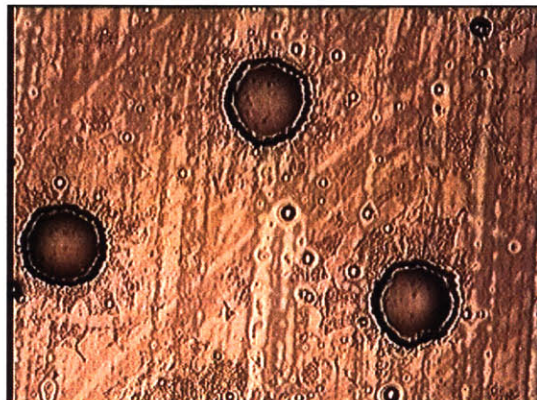


Figure B.35. B100 μ m10% with lubricant after testing

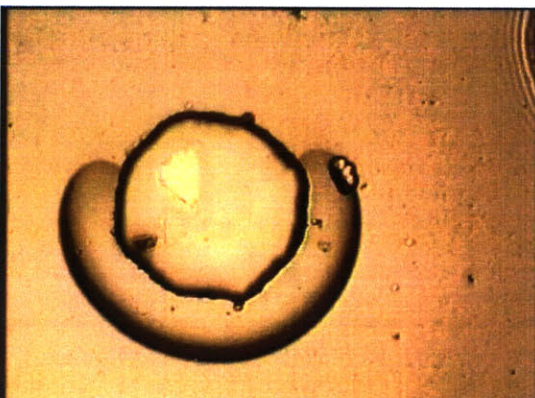


Figure B.33. 100 μ m10% misshapen hole

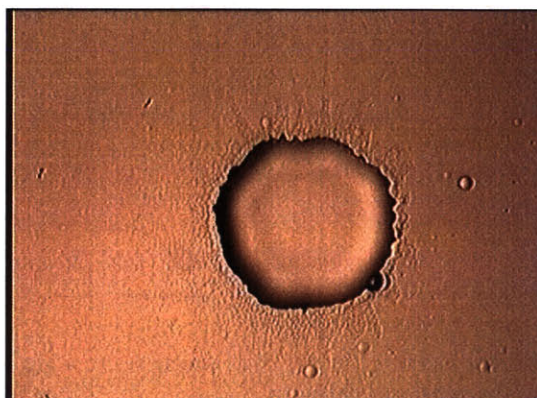


Figure B.36. B100 μ m10%

125 μ m Square Pores with 15% Feature Density

125 μ m15%

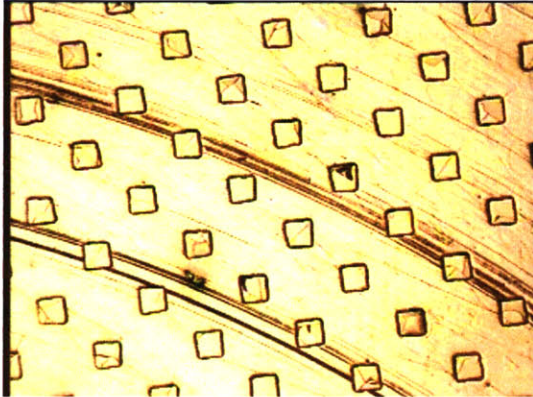


Figure B.37. 125 μ m15% with wear scars

B125 μ m15%

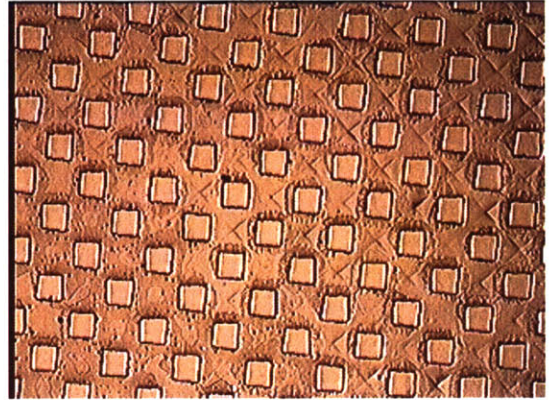


Figure B.40. B125 μ m15%

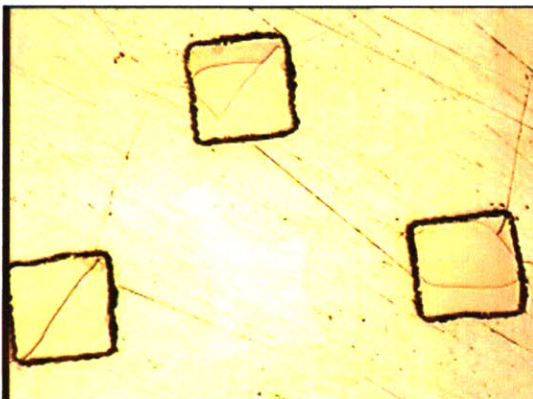


Figure B.38. 125 μ m15%

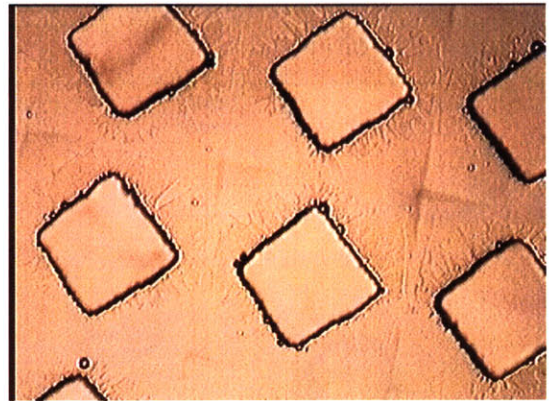


Figure B.41. B125 μ m15%

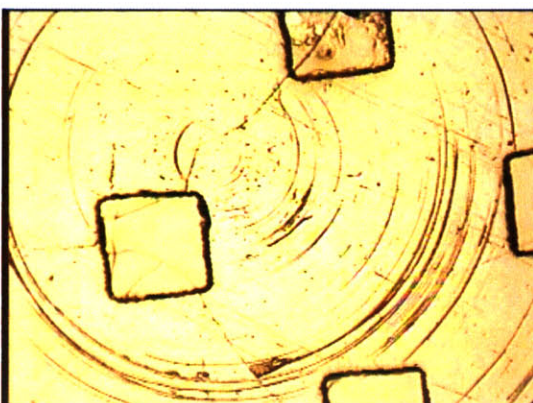


Figure B.39. 125 μ m15% showing wear scars at the center of rotation

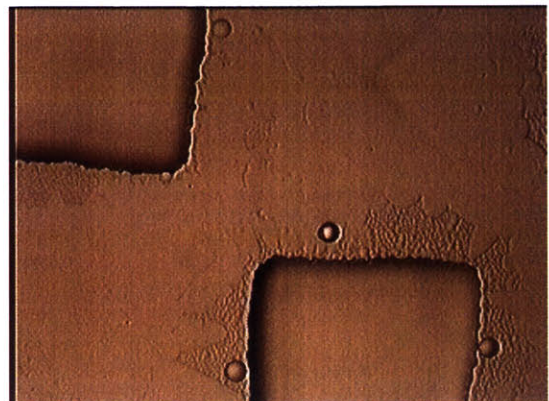


Figure B.42. B125 μ m15% showing surface texture

Control Surface

(Pictures were only taken of the Bcontrol surface)

BControl

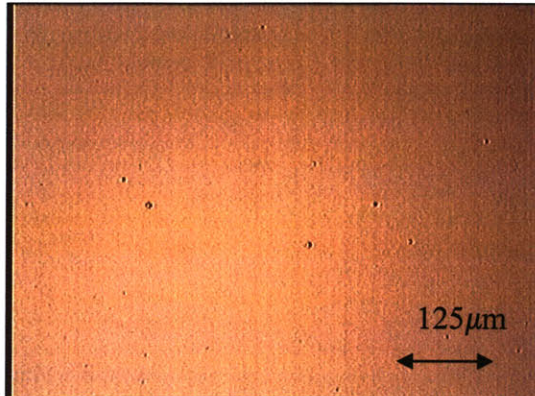


Figure B.43. Bcontrol

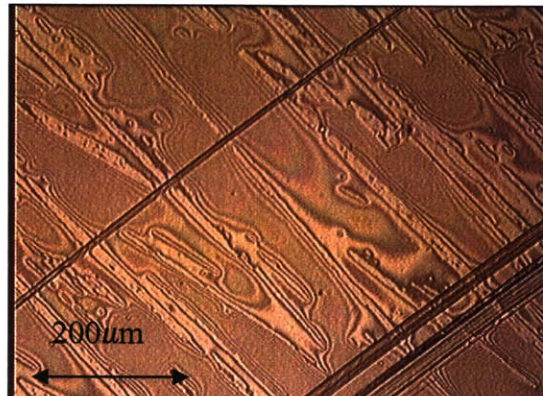


Figure B.45. Bcontrol after testing with lubricant and wear scars

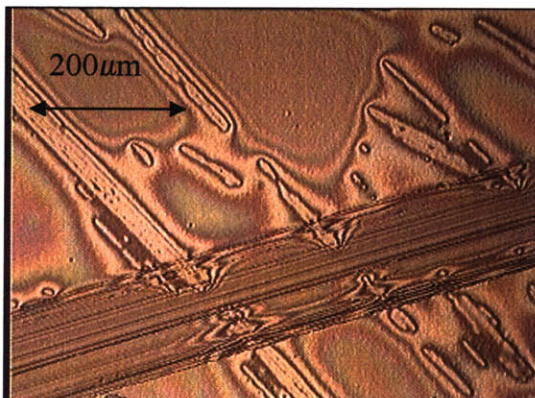


Figure B.44. Bcontrol after testing with lubricant and wear scars

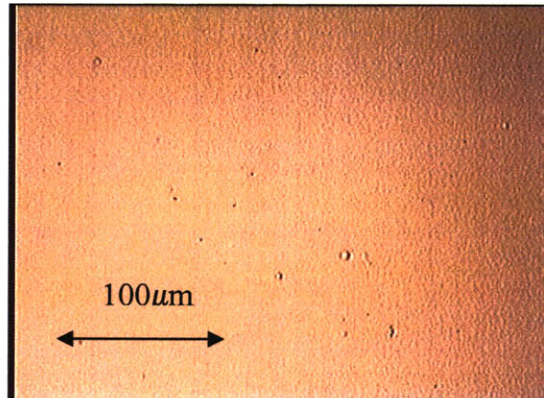


Figure B.46. Bcontrol showing surface texture

Appendix C: Second Order Fluid Solution for Weakly Elastic Fluids

* Notes from Gareth McKinley, Professor in Mechanical Engineering at MIT

$$3\eta_E \dot{\epsilon} = (3\eta_0 + 3b_E \dot{\epsilon}) = \frac{(2x-1)\sigma}{R}$$

Scale with $h = R/R_0$, $t = \hat{t}/t_{\text{char}} = \hat{t}\sigma/6\eta_0 R_0$

$$\left\{ 1 + \left(\frac{b_E \sigma}{3\eta_0^2 R_0} \right) \left(\frac{-1}{h} \frac{dh}{dt} \right) \right\} \left(\frac{-1}{h} \frac{dh}{dt} \right) = \frac{(2x-1)}{h}$$

$$\text{where } B = \frac{b_E \sigma}{3\eta_0^2 R_0} = \frac{b_E}{\eta_0} \frac{\sigma}{3\eta_0 R_0} = \frac{\lambda \sigma}{3\eta_0 R_0}$$

For the Newtonian Solution:

B=0

$$\begin{aligned} \frac{dh}{dt} &= -(2x-1) \\ h &= 1 - (2x-1)t \\ R &= R_0 - \frac{(2x-1)\sigma}{6\eta_0} \hat{t} \\ t_c &= \frac{6\eta_0 R_0}{(2x-1)\sigma} \end{aligned}$$

For the Second Order Fluid Solution:

Solve: $B(-\dot{h})^2 - h\dot{h} - (2x-1)h = 0$

Solution: $\frac{1}{2}(e^{2y} - 1) + y = \frac{(t_c - t)}{2B}$

Where $y = \sinh^{-1} \left(\frac{h}{4B(2x-1)} \right)^{1/2}$

Close to breakup for $y \ll 1$:

$$y \approx \frac{(t_c - t)}{4B}$$

$$\sinh y \approx y \approx \left(\frac{h}{4B(2x-1)} \right)^{1/2}$$

or $h \approx \frac{(2x-1)}{4B} (t_c - t)^2$

Rescaling

$$h = R/R_0, \quad t = \frac{\hat{t}\sigma}{6\eta_0 R_0}$$

or $\frac{R}{R_0} \approx \frac{(2x-1)3\eta_0^2 R_0}{4b_E \sigma} \cdot \frac{(\hat{t}_c - \hat{t})^2 \sigma^2}{36\eta_0^2 R_0^2}$

$$R \approx \frac{(2x-1)}{48\sigma} \cdot \frac{\sigma}{b_E} (\hat{t}_c - \hat{t})^2$$

Summary of Fitting Protocol/Equations

1) External Length Scale

- Original equations contain an (arbitrary) external scale, R_0
- This cancels out when substituting for $h = R/R_0$

$$t = \frac{\hat{t}\sigma}{6\eta_0 R_0}$$

$$B = \frac{\lambda\sigma}{3\eta_0 R_0}$$

To Be Fitted:

$$y = \sinh^{-1} \left(\frac{h}{4B(2x-1)} \right)^{1/2}$$

$$\frac{1}{2}(e^{2y} - 1) + y = \frac{(t_c - t)}{2B}$$

for $i = 1, 2, \dots, N_{\text{data}}$

Left-Hand Side

$$y^{(i)} = \sinh^{-1} \left\{ \left[\frac{(R/R_0)}{4 \left(\frac{\lambda\sigma}{3\eta_0 R_0} \right) (2x-1)} \right]^{1/2} \right\} = \sinh^{-1} \left\{ \left[\frac{3\eta_0 R^{(i)}}{4(2x-1)\lambda\sigma} \right]^{1/2} \right\}$$

Right-Hand Side

$$\frac{1}{2B}(t_c - t^{(i)}) = \frac{\frac{\sigma}{6\eta_0 R_0} (t_c - t^{(i)})}{2 \frac{\lambda\sigma}{3\eta_0 R_0}} = \frac{\hat{t}_c - \hat{t}^{(i)}}{4\lambda}$$

2) Fitting

Determine \hat{t}_c (critical time) - intercept
 λ (relaxation time) - curvature
 $\frac{3\eta_0}{(2x-1)\sigma}$ (1/capillary velocity) - linear region

3) The Apparent Extensional Viscosity (Derived from Fit)

$$\eta_E \dot{\epsilon} = \eta_E \frac{-2}{R} \frac{dR}{dt} = \frac{(2x-1)\sigma}{R}$$

$$\eta_E = \frac{(2x-1)\sigma}{-2(dR/dt)} \text{ [Pa.s]} \quad \text{or} \quad \frac{\eta_E}{\eta_0} = \frac{(2x-1)\sigma}{\eta_0} \frac{1}{-2(dR/dt)}$$

- a) do this from data $dR^{(i)}/dt^{(i)}$
- b) do this from theory prediction (must be linear with rate, as this is the model prediction)

NB: for consistency, plot R(t) [m] and dR/dt [m/s]